N° d'ordre : 42198

THESE

Présentée à l'Université de Lille 1
École Doctorale Sciences Pour l'Ingénieur

Pour obtenir le grade de :

DOCTEUR DE L'UNIVERSITE

Spécialité : MICRO ET NANOTECHNOLOGIES, ACOUSTIQUE ET TELECOMMUNICATIONS

Par

Maria Fahed

"Selective area growth of in-plane III-V nanostructures using molecular beam epitaxy"

Soutenance le 24 novembre 2016 devant la commission d'examen

Membres du jury :

Chantal FONTAINE	Directrice de Recherche, LAAS, Toulouse	Rapporteur
Charles CORNET	Maître de Conférences, INSA Rennes	Rapporteur
Clément MERCKLING	Pr. Scientist, IMEC, Louvain	Examinateur
Gilles PATRIARCHE	Directeur de Recherche, C2N, Marcoussis	Examinateur
Isabelle LEFEBVRE	Chargée de Recherche, IEMN	Examinatrice
Sylvain BOLLAERT	Professeur, Université de Lille 1	Président du jury
Ludovic DESPLANQUE	Maître de Conférences, Université de Lille 1	Co-encadrant
Xavier WALLART	Directeur de Recherche, IEMN	Directeur de thèse

Remerciements

Je tiens d'abord à remercier Mr. Lionel Buchaillot, directeur de l'Institut d'Electronique, de Microélectronique et de Nanotechnologie (IEMN), de m'avoir permis de réaliser ma thèse au sein de cet Institut. Ce travail a bénéficié du soutien financier de la région des Hauts de France ainsi que des contrats ANR SAMBA et MOSInAs.

Je remercie Mme Chantal Fontaine et M. Charles Cornet d'avoir accepté d'être rapporteurs de ce manuscrit, Mme Isabelle Lefebvre et MM. Gilles Patriarche, Clément Merckling et Sylvain Bollaert d'avoir accepté de faire partie de mon jury de thèse. Ce fut pour moi un honneur mais aussi un plaisir que de présenter mes travaux devant eux.

Un grand merci à mon directeur de thèse Xavier Wallart, directeur de recherche à l'IEMN, pour sa confiance, sa patience et pour m'avoir soutenue tout au long des trois années. Je lui sais gré de ses encouragements et de nos discussions riches en idées que nous avons partagées. Il m'a surtout appris à exploiter en profondeur les résultats et à les exposer clairement lors de présentations orales ou dans des publications. Je le remercie aussi de m'avoir initiée à la diffraction de rayons X.
Je suis également reconnaissante à mon co-encadrant, Ludovic Desplanque, maître de conférences à l'université de Lille 1, pour ses remarques et suggestions pertinentes. Je le remercie très chaleureusement pour sa bonne humeur, ce travail n'aurait pas été aussi loin sans lui.
Etre votre thésarde a été une sacrée expérience. Merci pour vos précieux conseils et votre grande disponibilité.

Je souhaite également remercier M. Gilles Patriarche du C2N qui a effectué les analyses de microscopie électronique en transmission et qui a répondu toujours très rapidement à mes questions et demandes. Je le remercie chaleureusement pour notre précieuse collaboration et sa grande disponibilité.

Je tiens également à remercier MM. Jean-Louis Codron et Christophe Coinon, les rois de l'épitaxie car sans eux je n'aurais certainement pas pu accomplir ce travail. Merci d'avoir pris le temps de me former à l'EJM et d'avoir participé à toutes mes campagnes d'épi. Un grand merci également pour vos précieux conseils et pour les fructueuses discussions que nous avons pu avoir sur les problèmes de techno rencontrés durant ce travail.

Enfin, merci à l'ensemble du groupe Epiphy Dominique Vignaud, Djamila Hourlier, Vinay, Sri, et Alexandre qui ont rendu mon passage à l'IEMN fort agréable.

Je suis très reconnaissante à David Troadec pour le FIB-STEM. Quand je lui demandais une lame, je lui disais «je pense que c'est ma dernière lame » et il me répondait «je ne te crois pas», parce qu'une semaine plus tard je revenais vers lui pour faire une nouvelle lame !

Un grand merci à Dominique Deresmes et Charlène Brillard pour m'avoir initiée avec passion à l'AFM. Merci pour leur disponibilité et bonne humeur. Merci à Christophe Boyaval qui m'a formé sur le MEB. Egalement merci à François Vaurette et à Christiane Legrand pour leur aide dans les étapes techno réalisées au cours de ce travail.

Je remercie également M. Vladimir Kaganer pour son aide dans l'interprétation des résultats de diffraction de rayons X.

Je remercie tous mes collègues de l'IEMN, grâce à qui je garderai un très bon souvenir de ces trois années.

Je remercie également ma famille pour m'avoir toujours entourée : Maman, Papa, Fouad, et Paul. Tout n'est que trop peu en comparaison de l'amour qu'ils m'ont donné.

Mes derniers mots vont à Georges, mon rayon de soleil au quotidien...

Merci beaucoup !

ABSTRACT

The use of nanostructures such as quantum dots and nanowires is a very promising way of integration of III-V semiconductors on silicon, since it allows answering most of the associated material challenges. Together with the continuous trend in device scaling, it should lead to the development of new highly efficient opto- and microelectronic circuits. This appeals for a full mastering of the growth and processing of 3D architectures at the nanometer scale. Consequently, the present work aims at investigating the selective area growth (SAG) of III-V semiconductors by molecular beam epitaxy (MBE) in nanoscale patterns. Homoepitaxial SAG of InAs and InP are first reported in order to show that the growth conditions, the opening width and the stripe directions allow tailoring the nanocrystal shape. We then achieve the SAG of in-plane GaSb nanotemplates on a highly mismatched GaAs (001) substrate at low temperature by atomic hydrogen assisted MBE. We highlight the impact of the nano-stripe orientation as well as the role of the Sb/Ga flux ratio on the strain relaxation of GaSb. Finally, from this study, we demonstrate how these GaSb nanotemplates can be used for subsequent growth of in-plane InAs nanowires.

KEYWORDS: III-V compounds, Selective area growth, Molecular beam epitaxy, In-plane nanowires, Antimonides.

RÉSUMÉ

Pour répondre aux défis matériaux relatifs à l'intégration des semiconducteurs III-V sur silicium, l'utilisation de nanostructures telles les boîtes quantiques et les nanofils s'avère une voie très prometteuse. Associée à la miniaturisation continue des dispositifs, elle devrait permettre l'émergence de nouveaux circuits opto et microélectroniques performants. Cela nécessite auparavant une maîtrise complète de la croissance et de la technologie des architectures tridimensionnelles à l'échelle nanométrique. Dans ce contexte, ce travail présente l'étude de la croissance localisée de semiconducteurs III-V par épitaxie par jets moléculaires (EJM) dans des motifs nanométriques. Nous discutons d'abord l'homoépitaxie localisée d'InAs et InP et établissons que les conditions de croissance ainsi que la largeur et l'orientation des ouvertures permettent de contrôler la forme des nano-cristaux obtenus. Nous démontrons ensuite la croissance sélective à basse température de GaSb sur substrat GaAs (001) fortement désaccordé en maille par EJM assistée d'un flux d'hydrogène atomique. Nous mettons en évidence l'impact de l'orientation des ouvertures, ainsi que le rôle du rapport de flux Sb/Ga sur la relaxation des nanostructures GaSb. Enfin, à partir de cette étude, nous démontrons comment ces nanofils GaSb peuvent être utilisés pour la croissance ultérieure de nanofils InAs horizontaux.

MOTS-CLÉS: Semi-conducteurs III-V, Croissance localisée, Épitaxie par jets moléculaires, Nanofils horizontaux, Antimoniures.

Introduction 12

CHAPTER I: III-V semiconductor selective area growth: motivation and background 15
  1. III-V nanostructures for microelectronics 15
    1.1. Si-MOSFET limitations and interest for III-V semiconductors 15
    1.2. Challenges for III-V MOSFET integration 16
        1.2.1. Lattice mismatch 17
        1.2.2. Antiphase boundaries (APBs) 19
        1.2.3. Thermal expansion 20
        1.2.4. Conclusion 21
    1.3. III-V nanostructures 21
      1.3.1. Top-down process 21
        a) Nanowire based devices 21
        b) Towards defect reduction 22
      1.3.2. Bottom-up process 23
    1.4 Conclusion 25
  2. Selective area growth background 25
    2.1. Experimental results 25
      2.1.1. Selectivity 25
      2.1.2. Crystal shape 28
        a) Homoepitaxial SAG 28
        b) Heteroepitaxial SAG 29
    2.2. SAG modeling 31
      2.2.1. Equilibrium crystal shape (ECS) 31
      2.2.2. Facet kinetics 34
  3. Thesis objectives 36
  References 38

CHAPTER II: Experimental setup 45
  1. MBE Growth 45
    1.1. IEMN MBE systems 45
    1.2. Growth monitoring 46
      1.2.1. In-situ characterization: Reflection high-energy electron diffraction (RHEED) 46

a) Flux calibration 46
b) Surface reconstruction 47
1.2.2. Temperature calibration 47
2. Sample preparation 47
2.1. Pattern elaboration 48
2.2. Surface cleaning in MBE chamber 49
3. Material characterization 52
3.1. Morphological characterization 52
3.2. Structural characterization 54
3.2.1. X-Ray Diffraction: principle and experimental setup 54
3.2.2. XRD Analysis 55
a) Determination of epitaxial film lattice parameters 56
b) Crystalline quality 57
Williamson-Hall model 58
Extended version of Williamson-Hall model 59
References 62

CHAPTER III: Homoepitaxial selective area growth of InP and InAs 65
1. Parameters influencing the selectivity 65
1.1. Growth temperature 65
1.2. V/III flux ratio 66
2. InAs selective growth 67
2.1. InAs nanostructure morphology 67
2.1.1. As/In flux ratio influence on the nanostructure shapes 67
2.1.2. Nanostructure shape evolution as a function of deposited thickness 69
2.2. Facet growth rates 71
2.3. InAs facet surface energies 74
2.4. Conclusion 76
3. InP selective growth 78
3.1. InP nanostructure morphology 78
3.1.1. P/In flux ratio influence on the nanostructure shapes 79
a) 200 nm wide stripe openings 79
b) 100 nm wide stripe openings 81

3.1.2. Nanostructure shape evolution as a function of deposited thickness 82
3.2. Facet growth rates 84
3.3. Equilibrium Crystal Shape (ECS) model 85
3.3.1. InP facet surface energies.. 85
3.3.2. Evaluation of the chemical potential from the nanostructure crystal shape........ 86
3.3.3. Nanostructure shape evolution in the first growth stages 89
3.4. Range of values for the interface energy between InP and the mask 90
3.5. Conclusion 93
4. General conclusion 95
References 96

Chapter IV: Heteroepitaxial selective area growth of InAs/GaSb nano-heterostructures on GaAs(001) 97
1. Optimization of the GaSb/GaAs selective growth 97
1.1. Growth temperature 97
1.2. Atomic hydrogen flux during the growth 101
1.3. Sb/Ga flux ratio 104
1.3.1. GaSb nanostructure morphology.. 104
1.3.2. GaSb-lattice relaxation 107
1.4. Conclusion 110
2. InAs/GaSb/GaAs 110
2.1. Structural analysis 110
2.1.1. 2D growth.. 110
a) STEM-analysis 111
b) XRD-analysis 113
Williamson-Hall model... 113
Extended version of Williamson-Hall model.. 114
2.1.2. Selective area growth 116
a) STEM-analysis 116
b) XRD-analysis 119
InAs on 65 nm GaSb.. 119
InAs on 150 nm GaSb.. 122
2.1.3. Discussion 124
2.2. Chemical analysis 126

3. General conclusion 131
References 132

Conclusions and perspectives.. 134

Annex: Selective area growth of GaAs/GaAs(001) 137

Introduction

Over the past fifty years, the manufacturing of silicon for microelectronics has exponentially increased with strong impact in everyday life. However, during these last 10 years, the microprocessor performances face serious brakes related to the high dissipated power density and the difficulty of reducing the supply voltage without degradation in the ON current of the device [1]. This is inherent to the large effective mass of electrons and holes in Si. For this reason, the use of low effective mass materials (III-V semiconductors) in the channel for next generation of metal oxide semiconductor field effect transistor (MOSFET) is considered for increasing the transistor performance. According to ITRS 2013 roadmap, the integration of III-V semiconductors on Si will be manufactured starting in 2018 for MOSFETs [2, 3]. However, several issues such as electrostatic control, parasitic resistance and gate capacitance are still challenging to improve the device performance [4]. One possible solution to circumvent these problems is to implement 3-dimensional (3D) device architectures with low effective mass material. Some theoretical studies have shown that a trade-off can be found to find a real improvement using low effective materials as the channel of a MOSFET working at low supply voltage [1, 5]. Such architectures may take the form of the fin-shaped, TriGate, or Gate-all-around field-effect transistors [4]. Moreover, Intel recently manufactured FinFET and TriGate transistors for the 22-nm and 14-nm node CMOS technology, respectively [4, 6].

On the other hand, the integration of III-Vs on Si is also promising for the fabrication of optoelectronic components for optical interchip connections to replace metallic wires, which suffer from a too high dissipated power. Moreover, bringing together microelectronics and photonics functionalities within a unique device obviously paves the way to the fabrication of new innovative circuits. Up to now, the integration of photonic devices with Si technology has mainly relied on an hybrid scheme with III-V layers or active optical components reported on the Si platform containing all passive circuitry but a monolithic approach is highly desirable. However, the monolithic integration of III-V semiconductors on Si faces growth challenges, i.e. thermal and lattice mismatches and polarity, which affect the structural quality and hence the device operation. For both targeted applications mentioned above (3D transistors and active optical devices) and to circumvent part of the material issues, the selective area growth (SAG) of III-Vs on Si appears as an attractive approach.

The growth techniques, which have been extensively used for III-V semiconductor growth, are metalorganic vapor phase epitaxy (MOVPE) and molecular beam epitaxy (MBE). For planar 2D heterostructures and vertical nanowire growth, both techniques have demonstrated prominent results. However, the SAG was first developed using MOVPE since selectivity is rather easily achieved thanks to different precursor decomposition rates with respect to the substrate materials. In order to reduce the thermal budget associated with the use of high growth temperatures in MOVPE, MBE can be a valuable alternative [7]. Moreover, only few results related to the SAG of GaSb using MOVPE have been reported [8].

From this standpoint, in this thesis, we will study the SAG of III-V semiconductors on (001) substrates using MBE. As a first step and before the integration on Si, we will focus on the SAG on standard III-V substrates (GaAs and InP) and aim demonstrating GaSb SAG by MBE. This manuscript is divided in four chapters.

Chapter I outlines the interest of the III-V nanostructures for microelectronics. It provides a review of the issues related to the III-V integration and processes involved in the elaboration of III-V nanostructures. The SAG background and the main targets of this PhD thesis are then exposed.

Chapter II introduces the MBE growth procedure, the pattern elaboration and surface cleaning methods used in this work in a first part. The second section focuses on the morphological and structural characterization methods performed on the elaborated samples.

Chapter III reports on the investigation of the homoepitaxial SAG of InP and InAs. It shows that the faceting of nanostructures selectively grown can be tailored playing with the growth conditions and the mask opening. In order to interpret these experimental results, we first determine the growth rate of each facet. If the crystal shape evolves in a more or less homothetic way (InP case), we interpret the observed shapes according to the equilibrium crystal shape model. Then using the minimization of total surface energy approach, we discuss the evolution of the nanostructure shape with the deposited thickness and we tentatively determine a range of values for the interface energy between InP and SiO_2 mask.

Chapter IV presents the optimization of the growth conditions for the SAG of GaSb on GaAs to promote the selectivity and growth homogeneity inside the patterns. The growth temperature, the presence of an atomic hydrogen flux during the growth and the Sb/Ga flux ratio are the growth parameters studied in this chapter. Moreover, we reveal the importance of the SAG approach on the GaSb layer quality. Finally, we demonstrate how these GaSb nanotemplates can be used as pedestals for subsequent epitaxial growth of high structural quality in-plane InAs nanowires.

Finally, a conclusion and perspective part summarizes the main results obtained in this thesis and outlines the perspectives for this work in terms of device realization and growth studies.

References

1. J. A. del Alamo, Nature **479,** 317, 2011.

2. www.itrs2.net

3. Viktoriia Gorbenko, "*Ion beam characterisation of III-V heterostructures for micro and optoelectronic applications*", CEA-Grenoble, 2015.

4. Considerations for Ultimate CMOS Scaling, IEEE Transactions on Electron Devices **59**, 7, 1813-1828.

5. K. J. Kuhn, IEEE Trans. on Electron Devices **59**, 1813, 2012.

6. M. Bohr, 14 nm Process Technology: Opening New Horizons, http://www.intel.com/content/dam/www/public/us/en/documents/pdf/foundry/mark-bohr 2014-idf-presentation.pdf

7. M. A. Wistey, et al., J. Vac. Sci. Technol. B **33**, 1, 2015.

8. T. Orzali, et al., J. App. Phys. **120**, 085308, 2016.

CHAPTER I: III-V semiconductor selective area growth: motivation and background

1. III-V nanostructures for microelectronics

1.1. Si-MOSFET limitations and interest for III-V semiconductors

In the last 50 years, Si microelectronics has known an exponential rise, which has led to many innovations in everyday life. This evolution has relied on the continuous down scaling of the metal oxide semiconductor field effect transistor (MOSFET) within the CMOS technology. However, since 15 years, this technology has entered a phase of 'power-constrained scaling' [1]. Actually, the dissipated power density has reached its limit value of ≈ 100 W/cm^2, which impedes further clock frequency or integration density increase without reducing the supply voltage. However, due to the large effective mass and low injection velocity of electrons and holes in Si, the reduction of the supply voltage below 0.8-0.9 V will induce degradation in the ON current of the device. One considered solution to circumvent this problem is the use of low effective mass material in the channel for next generation of transistors. The III-V semiconductor alloys $In_xGa_{1-x}As$ (with $x \geq 0.53$) are among the best candidates for such technology due to their lower bandgap, lower electron effective mass, higher electron mobility and injection velocity, compared to Si or Ge. The introduction of such III-V materials for n-MOSFET fabrication has attracted a lot of interest in the field of microelectronics for the last fifteen years.

Nevertheless, even if the use of III-Vs as channel materials in MOSFETs might allow reducing the supply voltage, the resulting performances will still be restricted by the fundamental limits of MOSFET operation, i.e. carrier thermionic emission. This leads to an upper electrostatic efficiency of the gate, defined by the subthreshlod slope (SS), which cannot reach values below 60 mV/decade. An alternative is the tunnel field effect transistor (TFET) in which carriers tunnel through the electrostatic barrier. For such transistors, III-Vs present a number of advantages due to the variety of possible heterojunctions and band alignments. Indeed, staggered or near-broken band configurations are highly desirable for the realization of TFETs with high ON current, which are encountered in the InGaAs/GaAsSb or InAs/(Al)GaSb heterostructures [2, 3]. Figure I.1 shows the lateral structures of n-type MOSFET and TFET with their corresponding energy band diagrams. In the TFET case, upon applying a positive voltage on the gate, electrons can flow from the source valence band to the channel conduction band at the source/channel tunnel junction.

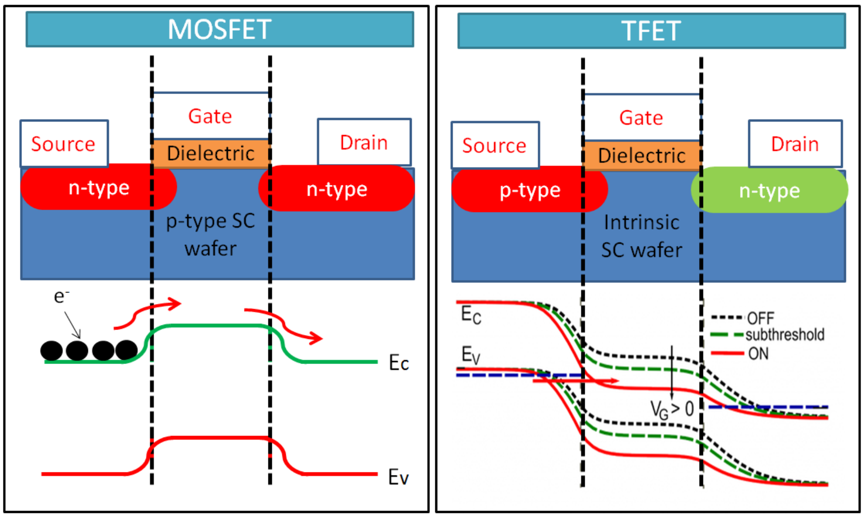

Figure I.1. Basic lateral MOSFET and TFET structures with the corresponding energy band diagrams.

1.2. Challenges for III-V MOSFET integration

Besides the advantages brought by III-V semiconductors, their integration in FETs based on a Si platform presents numerous challenges for both devices and materials. From a device point of view, the InGaAs alloys of interest as channel material exhibit a high electron mobility, mainly due to their low electron effective mass. This in turn reduces the 2D density of states in the channel, which limits the maximum sheet electron concentration that can be obtained and degrades the overall electrostatic control from the gate. This effect might be somewhat attenuated by the non-parabolicity of the conduction band leading to greater effective mass than predicted. On the other hand, the requirement for source and drain low resistance ohmic contacts must be fulfilled. Standard Si recipes as implantation or silicidation are less efficient with III-V materials. However, recent results have demonstrated good ohmic contacts using Ni on an InGaAs channel [4]. In the following, we discuss in more details the material issues associated with the integration of III-Vs on Si.

As discussed above, the III-V materials exhibiting an appreciable interest for microelectronic applications have lattice constants close to that of InP or GaSb. However, the corresponding substrates are brittle, expensive and available in limited size. The most commercially available substrates are the Si and GaAs ones. The epitaxy of III-V materials on such substrates remains the most attractive approach in terms of integration density and cost. This approach presents challenges in terms of large lattice mismatch, difference in thermal expansion coefficients and, in the case of Si, the growth of a polar on a non-polar material. For these reasons, III-V materials grown on Si generally exhibit a large density of defects such as threading dislocations (TDs), inversion domain boundaries called antiphase boundaries (APBs), micro-twins or cracks.

1.2.1. Lattice mismatch

Before beginning this section, it is mandatory to present the Si and III-V compound crystal structures. III-V compound semiconductors have a zinc-blende structure, where group III atoms occupy the positions of a face-centered cubic unit cell and group V atoms occupy the positions of a second face-centered unit cell shifted by (a/4, a/4, a/4) with respect to the first one (figure I.2(b)).

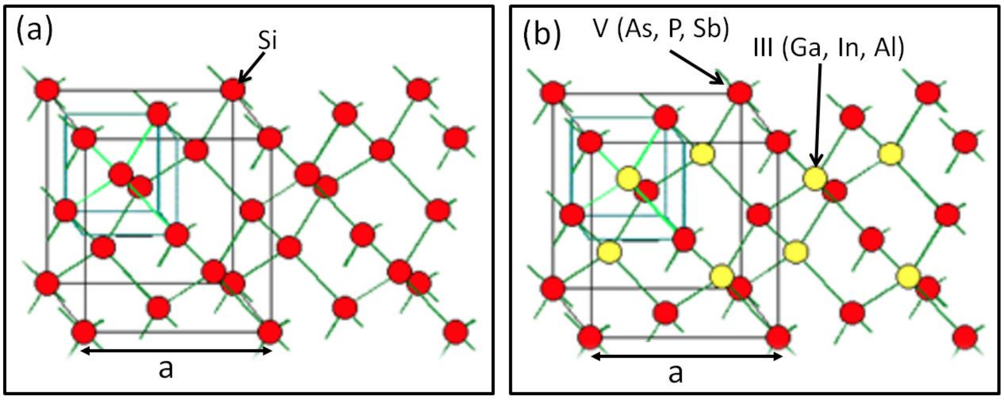

Figure I.2. Unit cell structure of a diamond lattice (a) and zinc blende lattice (b) [5].

Each atom is bonded to the four neighboring atoms of the other group. On the other hand, Si has a diamond cubic crystal structure (figure I.2(a)). The lattice mismatch between the epilayer and the substrate as a function of the lattice constants of the epilayer (a_{layer}) and the substrate ($a_{substrate}$) is given by:

$$f = \frac{a_{layer} - a_{substrate}}{a_{substrate}} \qquad \text{(Eq.I.1)}$$

When f < 2 %, the growth begins according to the Frank-van der Merwe (layer-by-layer or 2D) growth mode [6]. The in-plane lattice constant of the epilayer is imposed by the substrate and the epilayer experiments a bi-axial stress. This latter gives rise to an elastic energy increasing with the layer thickness. Once the critical thickness h_c is reached, the elastic energy is partially released by the introduction of misfit dislocations (MDs). Many studies have been devoted to the determination of h_c during 2D growths [7].

When 2 % < f < 6 %, the growth follows a Stranski-Krastanov growth mode (combined layer-by-layer + island growth) [6]. Here, a 2D layer precedes a transition towards 3D growth leading to the formation of strained islands on the top surface. The critical thickness is defined at the onset of this transition. Upon further growth, islands become bigger with the introduction of MDs before coalescence inducing even more defects.

When f > 6 %, small islands are nucleated directly on the substrate: this is called Volmer-Weber (3D) growth mode [6]. In this case, the critical thickness is reached immediately when the growth begins ($h_c \approx 1$ ML). After island coalescence, the TD density is very high.

Therefore, there is strong link between the mismatch and the dislocation density. In a general way, a dislocation can be understood as a combination of the two basic ones: the edge and screw dislocations. The edge dislocation introduces a half extra plane into a crystal, as it is shown in figure I.3(a). The dislocation line is the line where the half-plane terminates and it is perpendicular to the Burgers vector. This latter may be determined by consideration of a closed loop (atom to atom path) around the dislocation core.

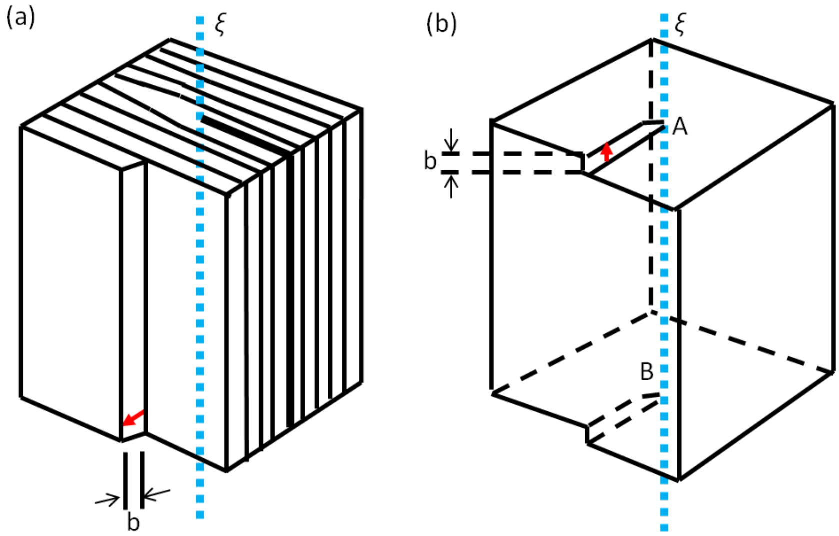

Figure I.3. Schematic diagrams of edge (a) and screw (b) dislocation in a cubic lattice. The dislocation line ξ and Burgers vectors b (red arrows) are shown [8].

On the other hand, the screw dislocation shears one part of the crystal with respect to the other one within a half-plane (figure I.3(b)). In this case the dislocation line corresponds to the position where the half-plane terminates and is parallel to the Burgers vector [9-10]. A mixed dislocation type is defined as resulting from a mixture of edge and screw dislocations with the dislocation line making an angle in the 0°-90° range with the Burgers vector. The two most commonly observed dislocations in highly mismatched III-V (001) growth, are the 60° and 90° ones, the latter being called Lomer dislocations. The 60° dislocation is a mixed type dislocation, with edge and screw components. In addition, the interaction of two 60° dislocations might lead to a 90° dislocation.

For low mismatch values, plastic relaxation occurs mainly via the introduction of 60° dislocations. Dislocation loops nucleate from the surface and propagate through the epilayer until the misfit segment reaches the interface and results in two threading segments [11]. Figure I.4(a) shows the TD and MD propagation inside the mismatched layer in one crystallographic direction. We notice an elongation of the MD at the interface and an elimination of the TD. However, if the same procedure occurs in two crystallographic directions, as it is shown in figure I.4(b), a TD will degrade the epitaxial layer due to the interaction of the TD and MD gliding in two different (111) planes.

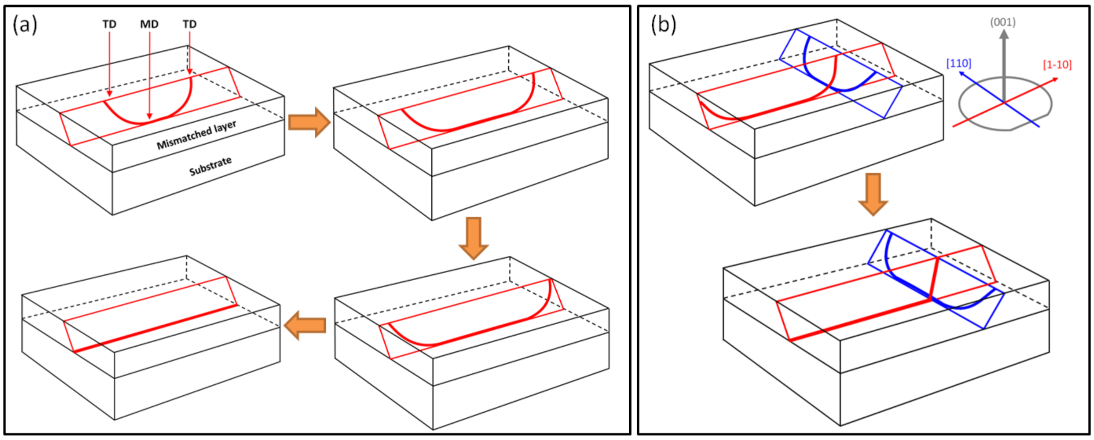

Figure I.4. Schematic of TD and MD propagation inside a mismatched layer in one (a) and two (b) crystallographic directions [12].

For high mismatch, 90° dislocations are progressively introduced at the edges of growing islands and are directly located at the substrate epilayer interface [13, 14]. However, even in this case, upon island coalescence, 60° dislocations can be introduced from the surface. The TDs form non-radiative recombination centers and accelerate the impurities diffusion along their lines. For this reason they are known as a cause of damage for device performance and reliability [15].

1.2.2. Antiphase boundaries (APBs)

Basically, APBs are two-dimensional arrays of atomic bonds between III-III or V-V atoms in a III-V material. The generation of APBs has been largely investigated in epitaxial growth of III-V materials on Si(001) [16-17]. As there is a difference in the crystal structure of group IV (Si) and III-V materials, APBs can arise during the epitaxial growth of III-V semiconductors on Si [18]. An APB might be generated at the coalescence region of two III-V material domains that have nucleated with different starting atoms (group III or V atoms) on a (001) surface of an elemental semiconductor (Si). However, in most cases, since III-V growth is initiated by either a group-III or a group-V supply, APBs will arise from III-V domains nucleated on two different Si terraces separated by a monoatomic step as it is shown in figure I.5(a). Since the APBs contain III-III or V-V atomic bonding in a matrix of III-V bonds, as in the case of dislocations, the APBs degrade the device performance significantly. Therefore, it is essential to eliminate the APBs for the integration of highly performing III-V materials on Si.

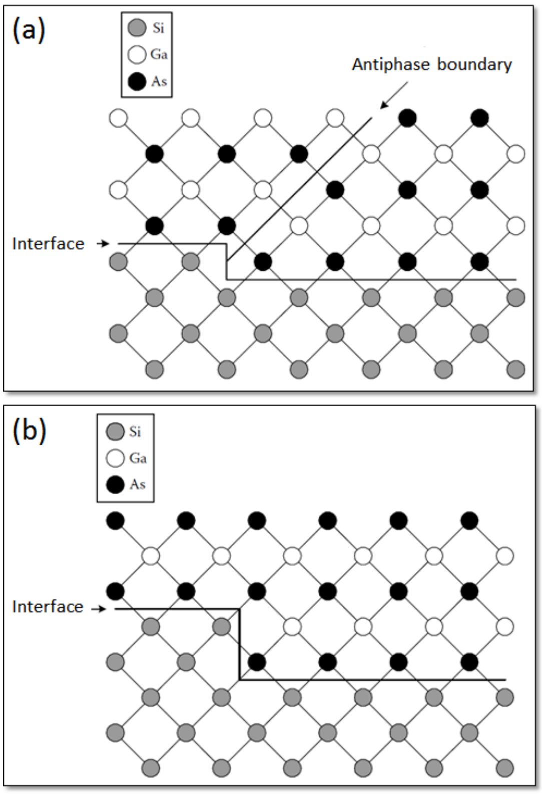

Figure I.5. Growth of GaAs on a Si(001) surface having monoatomic steps: presence of APBs (a), and double steps: no APBs (b)[19].

1.2.3. Thermal expansion

Besides the effects discussed above, the difference in thermal expansion coefficient between the layer and the substrate also plays a role in degrading the layer quality. Table I.1 presents the lattice parameters and the thermal expansion coefficients for Si and the III-V compounds at 300 K [19]. Therefore, if the lattices match at the growth temperature (in most cases > 500°C), upon cooling, the thermal expansion coefficient difference generates a stress in the epilayer which can lead to deformation or even to the appearance of cracks. For a given substrate/epilayer system, this difference in thermal expansion coefficients fixes an upper limit of the thickness that can be grown without crack formation.

Table I.1 Lattice constant and thermal expansion of III-V and Si materials at 300K [19].

	Lattice constant (Å)	Thermal expansion coefficient (10^{-6} /K)
GaSb	6.0959	6.35
GaAs	5.6533	6.03
Si	5.431	2.616
InAs	6.0584	4.28
InP	5.8687	4.6
InSb	6.4794	5.04
AlSb	6.1355	4.2

1.2.4. Conclusion

A lot of work has been done in the past to answer these issues, keeping the planar geometry. More recent works tend to prove that the most efficient solutions could be demonstrated using 3D nanostructures. These nanostructures may be efficient to solve some material issues (TD density, thermal expansion difference) but also to address the drawback of III-V materials. Indeed, 3D nanostructures can provide a solution for improving gate electrostatics (Ω-gate or gate all around transistors) or ohmic contacts (raised heavily doped source-drain contacts). In the following, we highlight the main results demonstrating the benefit of III-V nanostructures for microelectronic applications.

1.3. III-V nanostructures

For nanostructure-based devices, two main fabrication schemes are considered: the top-down and the bottom-up processes. The first one consists in growing first a 2D material before the definition of nanostructures by means of lithography and etching techniques. The latter includes two approaches: the nanowire growth with or without metal catalyst particles or selective area growth (SAG) on a (111) substrate and the SAG on a (001) substrate.

1.3.1. Top-down process

a) Nanowire based devices

Many attempts have been reported on MOSFET and TFET fabrication using III-V materials. For example in a recent work, Gu et al. have presented a comparison between planar and 3D MOSFETs based on InGaAs/InP at deep sub-micron gate lengths [20]. They claim that the 3D configuration greatly improves the off-state performance and facilitates enhancement-mode operation. Regarding TFETs based on InGaAs/InP, Rajamohanan et al. have demonstrated an improvement in electrical quality (low OFF state current) by achieving a channel etching method which decreases the damage in the mesa sidewall [2]. Moreover the work of Zhao et al. reveals InGaAs/InAs TFETs having a diameter of 15 nm, using a novel III-V dry etching process and gate-source isolation method. The nanowire TFET schematic and SEM image are represented in figure I.6 [21]. They demonstrate an excellent combination of steep slope (79 mV/dec) and ON current compared to other nanowire TFETs with III-V materials.

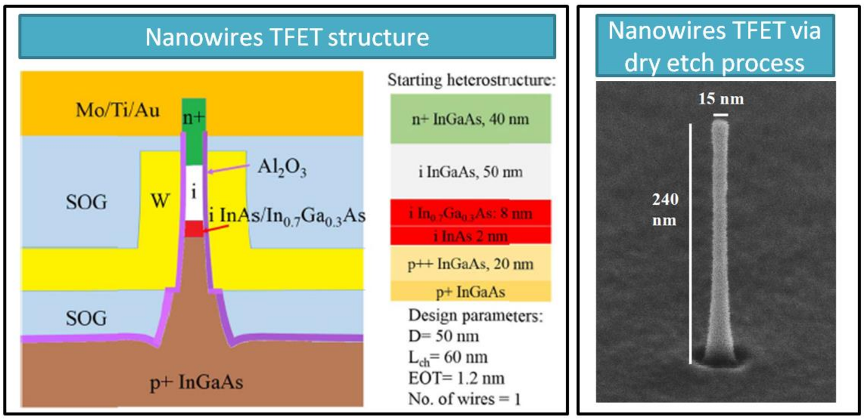

Figure I.6. Nanowires TFETs schematic and design parameters. SEM image of InGaAs nanowire TFET of diameter 15 nm defined by dry etching technique. [21].

While this approach has enabled an important number of device demonstrations, it reveals also several difficulties. On one hand, the etching process can induce damages on the semiconductor surface. On the other hand, the approach of starting from a 2D heterostructure leads to an important defect density when GaAs or Si substrates are used [1]. Since these defects can degrade the device performances, many attempts have been tried to mitigate the detrimental defects. In the next part, we present the main methods that were developed in 2D growth to impede the mismatch issues on the III-V layer grown on Si and GaAs substrates.

b) Towards defect reduction

Threading dislocation density (TDD)

Many researchers have claimed an optimization of the mismatch strain accommodation in the case of highly lattice-mismatched materials using a **gradual metamorphic** approach (compositionally graded-layers) [22-23]. The goal is to slowly increase the strain during the buffer growth so that dislocations are introduced progressively, avoiding the blocking process described in figure I.4(b) and hence the formation of TDs. It has demonstrated a number of perfectly relaxed heterostructures, with the further successful fabrication of devices [24-26]. However, this requires the growth of thick buffer layers (> 1 µm) [27], leading to poor thermal and electrical conductivities and therefore making this method not very satisfying for devices.

In order to reduce the TDD, another way is to promote the formation of an **interfacial 90° misfit dislocation array (IMF)**. This approach consists in creating a network of 90° (edge) MDs at the layer/substrate interface which relaxes most of the strain coming from the mismatch at the interface in both [110] and [1-10] directions and leads to a strain free layer-by-layer growth [28]. Almost strain-free layers grown via IMF have been demonstrated for several systems such as InAs/Ga(As, P) [29-31] and GaSb/GaAs [32]. Moreover, in the case of GaSb growth on Si or GaAs, the role of an AlSb interlayer has been extensively investigated [33-36]. However, the growth mechanism remains still unclear and the resulting TDD for µm-thick overlayers is rarely below $10^8/cm^2$.

Antiphase boundaries (APBs)

The key point to eliminate APBs in heteroepitaxy of a polar semiconductor on Si(001) is the elimination of monoatomic surface steps [37]. The overgrowth on double steps is free from APBs, as shown in figure I.5(b). If the Si (001) substrates are offcut by > 4° toward a [110] direction and are annealed, only double steps exist on the surface [38-40]. The APBs can be annihilated by the use of such surfaces, during the growth of III-V compounds [41-44], as for instance GaAs, GaSb [42-45], GaP [46-49], as well as AlSb [50]. However, these miscut substrates are not suitable for device processing. Indeed, all device areas should be exactly oriented with respect to the miscut direction to obtain double steps all over the surface, which is not obvious [51]. Nevertheless, recent results from Bogumilowicz *et al* have demonstrated the growth of APB-free GaAs epilayers on quasi nominal (001) Si, with a miscut angle <0.5° along the [110] direction [52]. In the same vein, Volz et al. concentrate on APB-free nucleation of GaP on exact Si(001) substrates [53].

1.3.2. Bottom-up process

Besides the top-down approach, an efficient method for reducing the defect density is the bottom-up process [54-55]. The nanowire growth approach in order to fabricate devices is a very attractive idea because it allows attaining narrow channels defined by the nanowire diameter in the 10-50 nm range, hence promoting electrostatic control. Li et al. have grown InAs nanowires on a Si(111) substrate by molecular beam epitaxy (MBE). In this work, a nanowire with a 20 nm diameter is selected and transferred for horizontal device fabrication [56]. Burke et al. followed a similar approach to make horizontal wrapped-gate nanowire transistors [57]. With the aim to impose the nanowire position and area, the SAG was used on (111) substrates. For instance Tomioka et al. have reported a device based on InAs nanowires grown using the SAG approach on Ge(111) substrate by metalorganic vapor phase epitaxy (MOVPE) [58]. They demonstrate a high-performance of vertical InAs nanowire surrounding-gate transistor.

The growth of nanowires on (111) surfaces leads to nanostructures free from APB. However, the use of these vertical nanowires grown on (111) substrates for device fabrication suffers from two main issues. The first one is related to the important density of crystalline defects along the nanowire, mainly stacking faults (SFs), twins and polytypism for which the zinc blende and wurtzite phases coexist within the same nanowire (figure I.7). The stacking sequence of the zinc blende structure along the [111] direction can be written as ″ABCABC″. When a SF occurs, either it gives rise to an extra atomic plane ″ABCBABC″ or it removes one ″ABCBC″. Another type of defect is the twin, which occurs exclusively on (111) planes with the following stacking sequence ″ABCABACBA″. These crystalline defects degrade the electronic transport properties as shown in the case of InAs nanowires [59]. The second drawback of these vertical nanowires concerns the device processing involving 3 vertically stacked contacts (source, gate and drain). Finally, the standard substrate orientation for microelectronic applications is the (001) one and not the (111) one.

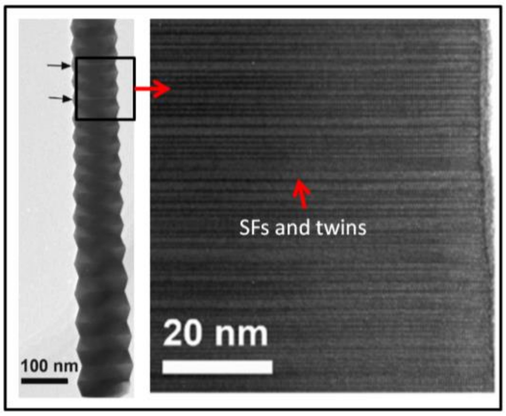

Figure I.7. TEM images illustrating InAs nanowires grown by MOVPE, exhibiting SFs, twins and polytypism for which the zinc blende and wurtzite phases coexist within the same nanowire [59].

This appeals for the growth of in-plane nanowires on (001) substrates. Using such approach, Borg et al. have demonstrated an InAs-Si heterojunction nanowire tunnel diode grown inside a horizontal SiO_2 nanotube template fabricated on a Si(001) substrate. They show that this process permits to obtain nanowires free from dislocations, and with an orientation and dimension directly given by the shape of the template [60]. SAG has also been applied to raise source/drain ohmic contacts, highlighting the control and design of the regrown areas by changing the growth parameters [61].

1.4 Conclusion

In this section we have shown that the integration of low effective mass III-V materials on standard semiconductor substrates using 2D growth faces difficulties, which increase the defect density inside the grown layer and degrade the device characteristics and reliability. The first one comes from the mismatch between the epilayer and the substrate, the second one arises from the difference in thermal expansion coefficients, and the third one is the APBs present in the case of III-V growth on Si. For the APB problem, more or less feasible solutions can be implemented. However, the first two problems are difficult to manage. For instance, in the case of GaSb grown on GaAs, the 7.8% mismatch leads to a threading defect density in the 10^8 cm^{-2} range [62].

In order to overcome these problems, the nanowire growth approach has been considered. Many attempts have been reported on the elaboration of vertical nanowires and associated devices. However, this fabrication route suffers from degraded crystalline quality and is not convenient for technological processing due to the use of a (111) substrate orientation. Therefore, our goal is to elaborate high quality in-plane III-V nanostructures on (001)-oriented substrate. The previous studies based on this approach will be discussed in the next section.

2. Selective area growth background

Since our goal is to study the SAG of III-V materials, in this part we discuss the previously achieved work in this framework. Firstly, we present the experimental results then we turn to the discussion of the models for crystal shape interpretation.

2.1. Experimental results

In this section, we review the previous work done on the SAG of III-V semiconductors. Firstly, we highlight the growth conditions leading to the selectivity with respect to an oxide mask i.e. with no polycrystal deposition on the oxide mask. Then, we focus on the III-V semiconductor shape inside openings. In this context two systems will be discussed: the homoepitaxial and the heteroepitaxial ones.

2.1.1. Selectivity

Several experiments have been dedicated to the growth on a semiconductor substrate covered by a dielectric mask (in most cases SiO_2) in which openings have been defined by lithography. The selectivity conditions depend on the epitaxy techniques. For the growth techniques based on metalorganic compounds (TMGa, TMAl, …), such as metalorganic vapor phase epitaxy (MOVPE) or metalorganic molecular beam epitaxy (MOMBE), III-V material grows inside windows opened in the oxide, but there is no deposition on the oxide itself. This is due to the fact that the mask does not catalyze the decomposition of the metalorganics. Therefore, the condition for SAG using metalorganic-based techniques relies mostly on the mask type and weakly on the growth conditions (temperature, growth rate, III/V flux ratio…), i.e. the SAG conditions can be rather similar than those used for conventional (non-selective) growth [63]. However, for techniques such as MBE (having elemental sources), which do not rely on the catalyzed surface decomposition of molecules, the realization of the SAG is not achievable without modifying the growth conditions. Indeed, for this growth technique the selectivity mechanism is only related to the re-evaporation and diffusion of group-III elements deposited on the mask. This mechanism can be achieved using a low growth rate or/and a high growth temperature. Figure I.8 shows an example of GaAs nucleation on a SiO_2 mask using a fixed Ga flux ratio of 0.1 ML/s and by varying the growth temperature (GT) from 630 to 585 °C [64]. In order to optimize the selectivity, the GT must be higher than 630°C. Another attempt was claimed on the SAG of $In_xGa_{1-x}As$, where the selectivity was demonstrated at a GT of 595°C [65]. In both cases, the GT must be high and the growth rate low enough to allow selective growth.

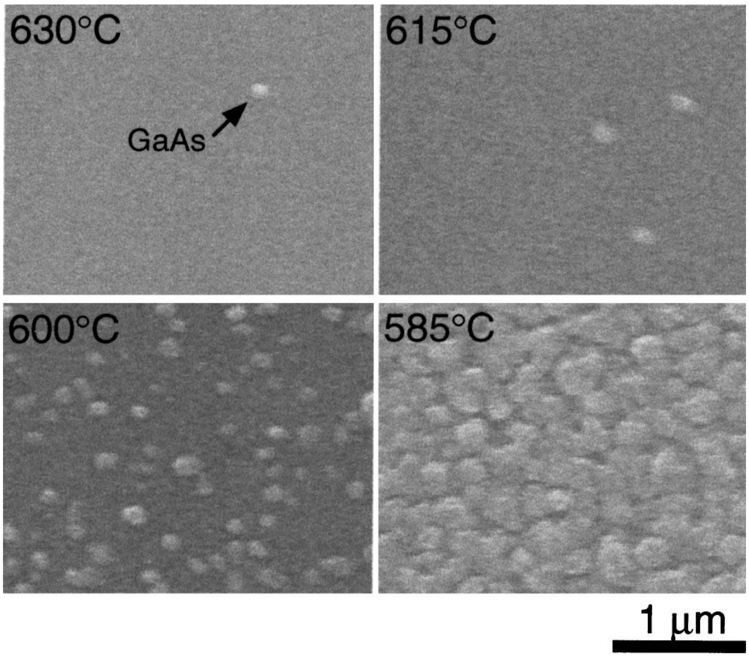

Figure I.8. SEM images of 100 nm of GaAs grown on un-patterned SiO_2 surfaces when varying the growth temperature from 630 to 585 °C. The Ga flux ratio is 0.1 ML/s. [64]

In MBE, the selectivity will mostly depend on the difference of sticking and diffusion coefficients of the group-III element on the mask and semiconductor surfaces respectively [66]. For GaAs, the above example shows that selectivity can be achieved reducing the growth rate and choosing the high limit of GT with respect to 2D growth conditions. In other words, it means that there exists a growth condition for which good quality GaAs can be grown in the openings without any polycrystalline material nucleation on the mask. Turning now to GaSb SAG, considering that the group-III element is still Ga, similar growth conditions as for GaAs should be used. However, good quality GaSb layers are usually obtained at a much lower GT, around 500°C [67-68]. A reduction of the GT is therefore very important to obtain high quality epitaxial nanostructures. One way to improve the growth selectivity for some III-V materials at low temperature with respect to a SiO_2 or a Si_3N_4 mask is the addition of an atomic hydrogen flux during the epitaxy as it has been demonstrated in the case of GaAs, GaInAs or InP [69-70].

Sugaya et al. have proposed a mechanism based on the enhanced Ga and As desorption from the SiO_2 surface due to the formation of Ga and As hydrides [69]. In the same way, Kuroda et al. have shown that the dominant factor of the selective growth mechanism of InGaAs/InP under H atomic flux is not an enhanced In and Ga atom migration from the masked regions to the growing regions, but rather an increased In and Ga atom desorption from the mask surface [70]. Actually, they claimed that the presence of the atomic hydrogen leads to the formation of Ga and In hydrides since the bond strength of Ga-H (66 kcal/mol) and In-H (58.1 kcal/mol) is larger than that of Ga-As (50 kcal/mol), In-As (48 kcal/mol), and In-P (47 kcal/mol) [71]. Therefore, on the mask surface, the Ga and In atoms tend to bind with atomic hydrogen rather than with As and P atoms, impeding the formation of polycrystalline InGaAs on the mask surface. This in turn may imply that for atomic hydrogen assisted growth of InGaAs on an un-patterned InP surface, hydride formation should occur and result in a lower thickness than the nominal one. Indeed, Kobayashi et al. have reported that atomic hydrogen reacts with Ga atoms and removes them from the GaAs surface annealed at a temperature higher than 850°C [72]. However, Bachrach et al. have claimed that the interaction between atomic hydrogen and (001) GaAs surfaces which leads to the formation of Ga hydrides is restricted to the top surface layer and cannot be ascribed to an etching mechanism [73]. To our knowledge, up to now, no results on the SAG of GaSb by MBE have been reported.

2.1.2. Crystal shape

The growth conditions, lattice mismatch and the opening size are the main parameters that may affect the crystal shape inside the opening windows. Actually, the control of the III-V arrangement inside the openings is very important since it is related to the device efficiency. In this section, we present previous work done on the homoepitaxial and the heteroepitaxial SAG in order to control the crystal shape inside the openings. For each SAG type, we first present the attempts demonstrated on **micrometer scale** patterns and we then focus on the ones at **nanometer scale** due to the continuous development of nanoscale lithography techniques.

a) Homoepitaxial SAG

The studies on the homoepitaxial SAG were the first step to understand the SAG mechanism. Firstly, it has been devoted to **micrometer scale patterns**, as for instance in the work of Bauhuis et al. which details the faceting of GaAs microcrystals grown by MOCVD inside square openings having an edge size going from 5 to 20 µm. They claimed that the final shape does not depend on the opening size, due to the constant growth rate of the facets [74]. Later on, Ujihara et al. studied the effect of the spacing between stripes, varying it from 1 to 20 µm for a fix opening size of 240 nm, on the InP crystal shape [75]. They compared their experimental findings with a model taking into account the surface and vapor phase diffusion [76]. When the spacing between patterns is comparable to the surface diffusion length on the mask, the surface diffusion contribution is dominant, and the surface diffusion length was estimated to be around 1-2 µm.

Let us now turn the discussion to the SAG inside **nanostructured patterns**. At this length scale mastering the nanocrystal shape is of paramount importance since it affects the optoelectronic and microelectronic states inside the semiconductor nanostructures such as quantum dots or nanowires. A recent work reports the influence of the base size and shape on the formation of InP pyramids by SAG using MOVPE, stressing the interplay between the major low-index facets in the final shape [77]. The aim of such study is to control the position and distribution of InAs quantum dots grown on these designed InP pyramids [78]. For the same goal, but using a vicinal GaAs surface, Fukui et al. have shown that when the misorientation angle of the substrate increases, the surface migration of Ga adatoms from the sidewall facets to the top region decreases, due to high step density enhancing the growth rate on the sidewalls [79].

Recently Lee *et al.* have explained the faceting of GaAs nanostructures directed along [110] in the framework of the equilibrium crystal shape model (ECS) [80-81], using the relative surface energy of the involved facets [82-84]. In this approach, the evolution of the facets is predicted according to the equilibrium theory and Wulff geometrical construction [81]. In the same way, the formation of vertical facets in one-dimensional high-aspect ratio GaAs gratings has been interpreted based on the minimization of total surface energy [84].

b) Heteroepitaxial SAG

In the goal of accommodating lattice mismatched heterostructures using SAG approach, the crystal shape behaviors were also studied. In the 90's, the heteroepitaxial SAG of unstrained heterostructures has been studied on **micrometer scale patterns**, as for instance in the work of Heinecke *et al.* which details the faceting of InP microcrystals grown on GaInAs depending on the opening orientation and the value of the P/In ratio using MOVPE or MOMBE. They achieved vertical sidewalls on the grown structures for high P/In ratios using small substrate misorientation [85-87]. These investigations can be used for the integration of optical devices. For the same III-V system, Kayser et al. studied the effect of the PH_3 flux on the crystal shape using MOMBE inside 10 µm opening size [88]. When the PH_3 flux increases, the migration length from the (111)B facets to (001) ones decreases and the crystal shape exhibits an "ear" formation, as it is represented in figure I.9. In contrast, for a low PH_3 flux, a uniform transfer of material from (111)B facets to (001) ones is observed, i.e. the migration length from the (111)B facets to (001) ones increases.

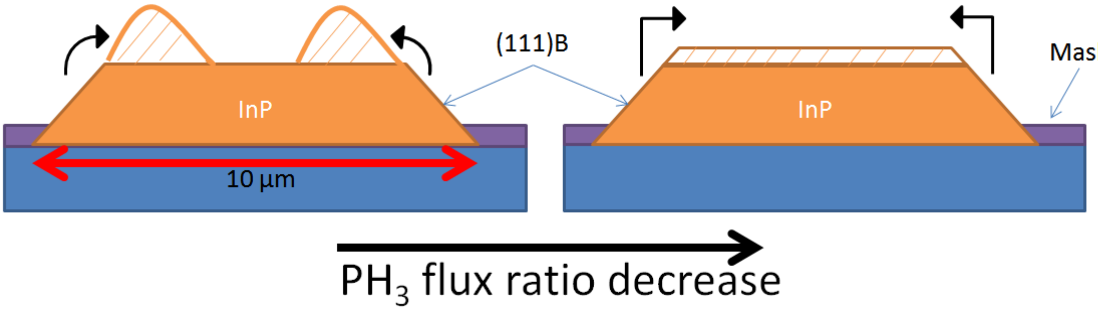

Figure I.9. Schematic of the surface migration processes on (111)B and (001) surfaces as a function of PH_3 flux [85].

More recently and for **nanostructured patterns**, Wang et al. have successfully used the SAG technique inside SiO_2 nano-trenches on Si to grow InP-based lasers on Si (001) [89]. They showed that this novel epitaxial technology suppresses threading dislocations and anti-phase boundaries for a deposited thickness as low as 20 nm. In the same way, Cipro et al. have shown that growing directly GaAs in SiO_2 cavities patterned on a nominal Si(001) surface is efficient to completely annihilate the APBs [90], thanks to the aspect ratio trapping (ART) mechanism [91]. Figure I.10 shows an example of GaAs grown on Si(001) using the ART approach. Via an aspect ratio (trench height/ trench width) of 1.8, the dislocations originating at the GaAs/Si interface are trapped by the oxide sidewalls leading to defect-free GaAs at the top of the trenches. In the same vein, Paladugu et al. demonstrate the minimization of the APBs by performing the selective epitaxial growth of III-V material on Si inside "V-grooves" with (111) facets [92].

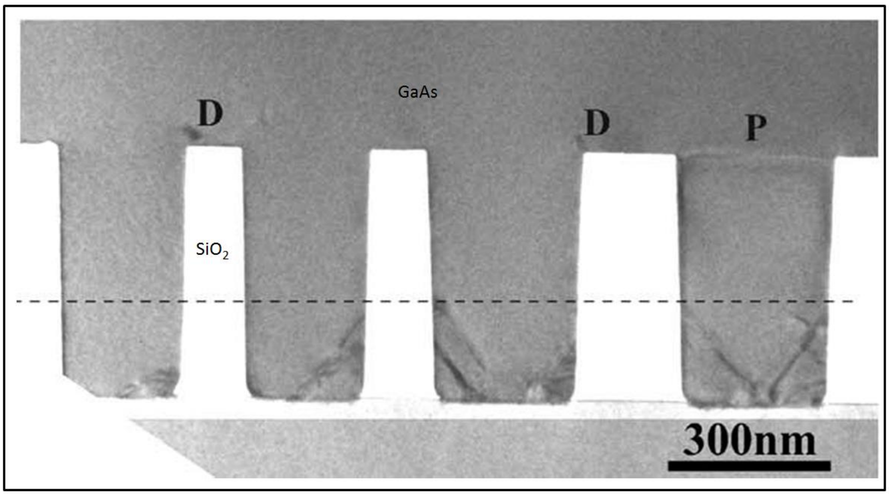

Figure I.10. Cross-sectional TEM images of GaAs on Si(001) in SiO_2 patterned trenches of aspect ratio of 1.8. Some defects are caused by coalescence: D indicate dislocations; P indicate planar defects [91].

Another approach based on SAG was investigated by Renard et al. in order to avoid the emission of MDs and the formation of APBs. This procedure consists in the lateral overgrowth after nucleation in 50 nm wide openings [93-94]. Using this approach, Yi et al. have reported the lateral overgrowth of GaSb nanostructures on the oxide mask using MOCVD. They showed that the GaSb films exhibit defects when the GaSb nanostructures coalesce [95]. Regarding the SAG of GaAs on Si (001), Hsu et al. have investigated the MOCVD growth on a 55 nm round-hole patterned SiO_2 mask on a Si substrate (figure I.11(a)). They showed that due to the blocking of the TDs along the SiO_2 walls, a reduction of the number of dislocations can be observed [96], as highlighted in the SEM images of the growth on a patterned (figure I.11(b)) and non-patterned substrate (figure I.11(c)). Moreover, Suryanarayanan et al. achieved a reduction of the defect density in an InAs epilayer grown on GaAs(001) using lateral epitaxial overgrowth by MOCVD [97]. They demonstrated that when the opening width is less than 1 µm, the InAs-microstructure shape changes in a way that accelerates defect reduction.

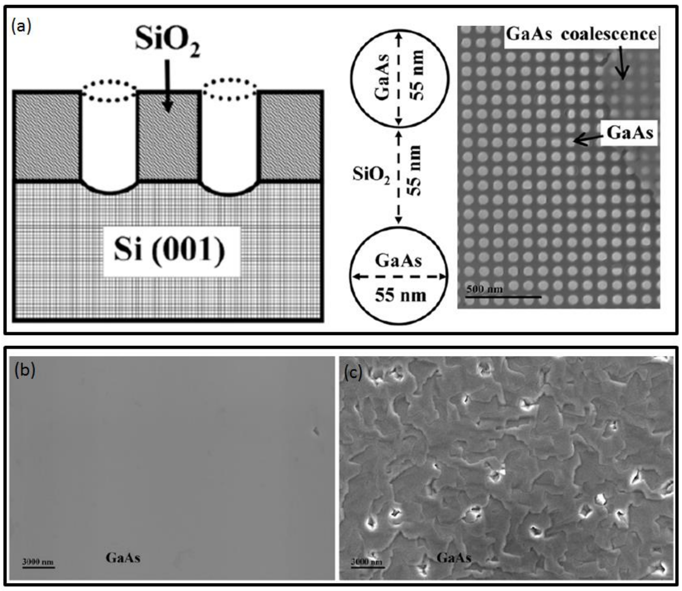

Figure I.11. Schematic diagrams showing the nanopatterned Si(001) substrate and the round-hole diameter and spacing, SEM image of the first step of GaAs filling the round holes (a), SEM images of 900 nm-thick GaAs deposited on patterned substrate (b), and non-patterned one (c) [97].

2.2. SAG modeling

Whatever the length scale considered, the final crystal shape is determined by:

- Surface/interface energies [98]
- Facet kinetics [99-101]

2.2.1. Equilibrium crystal shape (ECS)

When growth is not kinetically limited, the nanostructure shape can be interpreted considering previously calculated surface energies of the involved facets, which leads to the ECS model [98], [102]. To do that, the Wulff geometric construction on the observed 2D nanostructures is often used [103]. Different cases have to be considered:

- The growth is stress free, when the substrate and film have the same lattice constant ($f = 0$).
- The growth is pseudomorphic, when the film is stretched ($f < 0$) or compressed ($f > 0$) such that the substrate and the film in-plane lattice constants coincide.

In the following, we discuss the ECS model as a function of the mismatch between the layer and the substrate [104].

When f = 0, two cases are considered: in the first one, the substrate and layer materials are similar (free crystal) whereas in the second case they are different with the same lattice constant (unstrained crystal).

For an isolated crystal, the equilibrium shape is found by minimizing, at constant volume, the Gibbs surface free energy (G) given by [104]:

$$G = \sum_i \sigma_i . A_i \qquad \text{(Eq.I.2)}$$

where A_i and σ_i are the area and the surface energy of the facet i of the crystal, respectively. The equilibrium shape can be found with a geometrical construction based on the Wulff theorem:

$$\frac{\sigma_i}{H_i} = Constant \qquad \text{(Eq.I.3)}$$

where H_i is the distance of each facet (i) from a common point (Wulff's point) inside the crystal (figure I.12(a)). Therefore, for a free crystal growing in equilibrium conditions, its shape for different sizes (different constant) is similar around the common Wulff's point.

Considering now the growth of a crystal "A" on a substrate "B", the equilibrium shape in the absence of misfit can be again determined only by the minimization of the surface and interface energies. Besides the crystal "A" free facets of area S_i, the contact area A_{AB} with the substrate "B" must be introduced in such a way that the Gibbs surface free energy (G) is as following [104]:

$$G = \sum_i \sigma_i . A_i + A_{AB}(\sigma_{AB} - \sigma_B) \qquad \text{(Eq.I.4)}$$

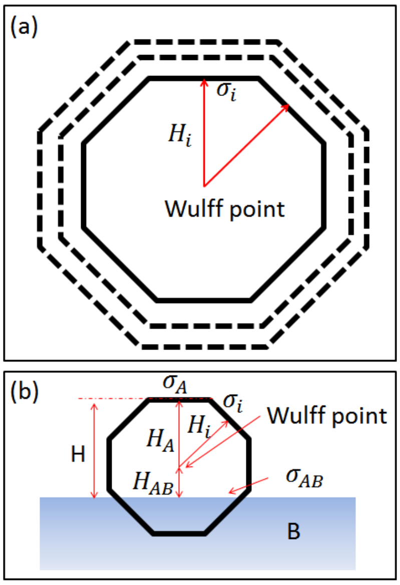

Figure I.12. Equilibrium shape evolution of a free crystal (a); of an island A on a substrate B having the same lattice parameter (b) [104].

The interfacial energy σ_{AB} is defined as a function of the adhesion energy of A on B (β):

$$\sigma_{AB} = \sigma_A + \sigma_B - \beta \qquad \text{(Eq. I. 5)}$$

From Wulff-Kaichew theorem we get:

$$\frac{\sigma_i}{H_i} = \frac{2\sigma_{AB} - \sigma_B}{H} = Constant \qquad \text{(Eq.I.6)}$$

where H is the emerging height of the crystal (figure I.12(b)). In this case (absence of misfit), the equilibrium shape maintains self-similarity above the substrate surface.

When f ≠ 0, an epitaxially strained crystal A is deposited on a lattice mismatched (f) substrate B. The equilibrium shape determination in this case is more complicated. Using the Wulff-Kaichew theorem, Muller et al. have studied the ECS of a 3D crystal deposited onto a lattice-mismatched substrate [104].

Jiang et al. reported a particular case of SAG of mismatched III-V materials on Si inside deep submicron trenches where they assume that the defect density is reasonably low [101]. Neglecting the effect of defects and using surface energy minimization, they determine the ratio between the facet lengths when the crystal is in an equilibrium state. This approach gives the same result as using the Wulff plot (discussed above) and simple geometrical arguments. They found that for the same growth conditions and when the growth proceeds, the following equation should be satisfied [101]:

$$\frac{L_{001}}{L_{111}} = Constant \qquad \text{(Eq.I.7)}$$

where L_{001} and L_{111} are the lengths of (001) and (111) facets, respectively (figure I.13(a)).

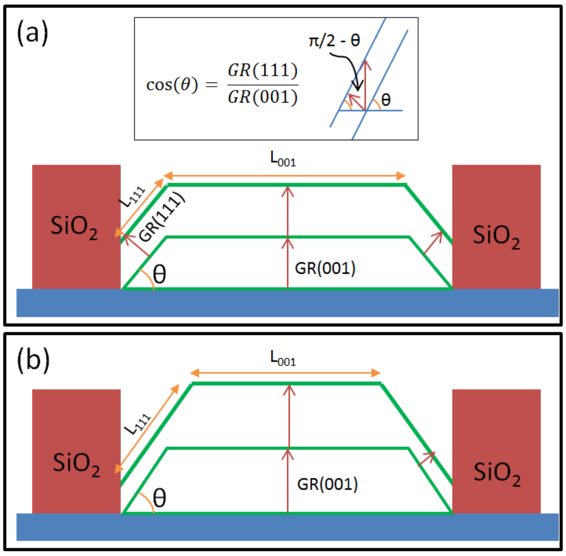

Figure I.13. Schematic of the equilibrium (a) and non-equilibrium (b) shape evolution inside submicron trenches.

To follow the evolution of the crystal shape during growth, growth rates (GR) for (001) and (111) facets can be measured [105-106]. Using simple geometrical arguments shown in the inset of figure I.13(a), to keep constant the facet length ratio in Eq. I.7, the GR(001) and GR(111) must obey to :

$$\frac{GR(111)}{GR(001)} = \cos(\theta) \qquad \text{(Eq.I.8)}$$

If Eq. I.7 is not satisfied, one of the two facets ((001) or (111)) will disappear (figure I.13(b)). This is illustrated for instance in the work of Dutartre et al. where the facet GRs of Si inside 1 µm wide trenches are determined using SiGe layers as markers [107-109]. They demonstrated that the facet GRs do not change when the growth proceeds inside the trenches (figure I.14). However, Eq. I.8 and I.7 applied to (001) and (113) facets are not satisfied during the growth, which therefore does not proceed under equilibrium conditions. This in turn implies that facet kinetics must be considered.

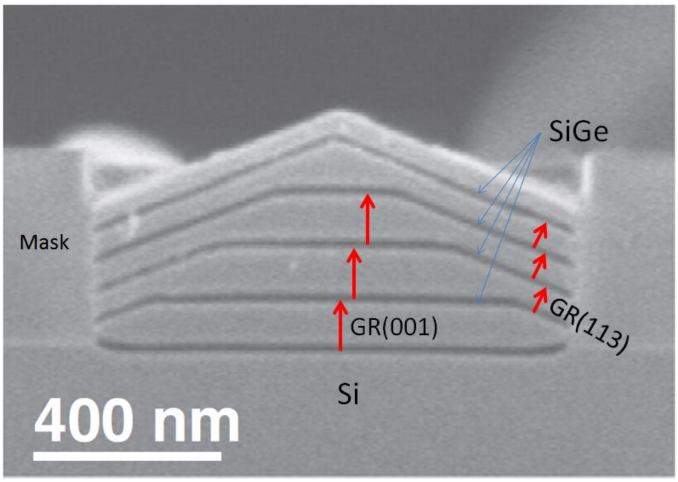

Figure I.14. SEM image recorded for the SAG of Si using a layer of SiGe as a marker [107].

2.2.2. Facet kinetics

Facet kinetics includes the surface diffusion (SD) on the facets and the surface attachment/detachment processes [110]. When discussing the SD mechanism on patterned substrates, it is assumed that the adatoms can be easily attached to/detached from the lattice when the growth proceeds. Conversely, in the case of surface attachment/detachment limiting case, the effect of SD can be neglected, i.e. a fast transport through a surrounding surface layer is assumed. However, in practice, it is not obvious to separate the SD and the surface attachment/detachment processes and most experimental works have been devoted to surface diffusion effects.

Indeed, the SD process was firstly extensively studied on 2D growths in order to measure the SD length of the group-III element atoms. In the 1990s, Hata et al. and Shen et al. have evidenced the surface diffusion length of Ga atoms during MBE growth of GaAs by means of reflection high-energy electron diffraction (RHEED) intensity oscillations [110-113]. These studies show that Ga atoms are quite mobile on the growing surface. The Ga surface diffusion length reaches as far as several micrometers and increases with decreasing V/III ratio [114]. In the same vein, Ohtsuka et al have reported another important result demonstrating that the Ga diffusion length significantly depends on the surface orientation [115]. Using a numerical simulation, they found the variation of the Ga diffusion length as a function of the surface orientation in the case of GaAs growth by MBE. These results are presented in figure I.15, where we notice that the minimum value of the Ga diffusion length is about 0.5 µm. These findings are further confirmed by the works of Ujihara et al. and Shen et al. who have reported typical values for the diffusion length of group-III element in the µm-range on patterned InP and GaAs substrates using MOVPE and MBE [116-117]. Therefore, the effect of the SD depends of the pattern dimensions. If this latter is below the typical SD length of the impinging species at the surface, then the effect of surface diffusion kinetics will be reduced.

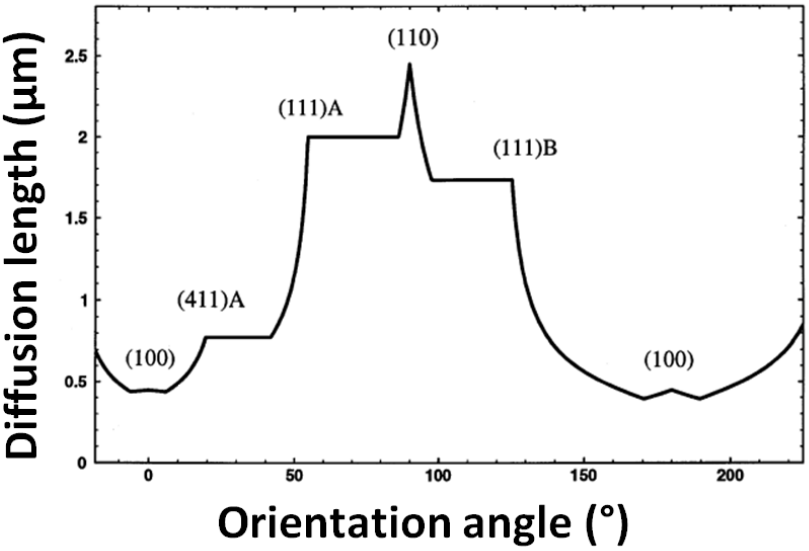

Figure I.15. Diffusion length versus surface orientation angle [115].

Jiang et al., have modeled the effect of kinetics on the evolution of (001) and (111) facets for the crystal shape inside submicron trenches [101]. The two possible migration directions towards the equilibrium shape are schematically shown in figure I.16. The first migration direction consists of an inter-facet surface migration from facet (111) to facet (001), and the opposite for the second migration direction (from (001) to (111)).

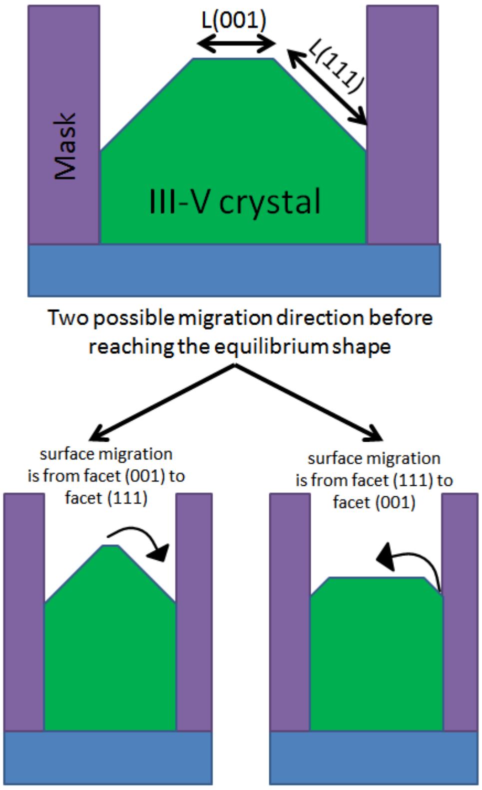

Figure I.16. Schematic of III-V SAG inside submicron trenches on (001) Si substrates and the two possible migration direction before reaching the equilibrium shape [101].

3. Thesis objectives

We have shown the importance of growing III-V semiconductor nanostructures on GaAs and Si substrates for microelectronic applications. We have then exposed the main problems related to the integration of III-V materials on GaAs and Si substrates such as thermal expansion coefficient, polarity or lattice constants. On the other hand, the useful active area of semiconductor being in most cases reduced to a few tenths of nanometers square per device, thanks to nanoscale lithography techniques, we have focused on the SAG approach using (001) substrates which allows the control of the nanostructure position.

In order to overcome these problems, the growth of vertical nanowires has been extensively developed in the last 15 years. However, besides crystal phase polymorphism issues, the inconvenience of this method is the use of a (111) substrate orientation. Therefore, our goal is to elaborate high quality in-plane III-V nanowires, using (001) substrate orientation.

We will first try to understand the mechanisms driving III-V nanocrystal shape inside oxide openings, in the framework of the ECS model and the kinetics phenomena described above. To do this, we will start with the simple case of III-V homoepitaxy (no strain), considering the

InP and InAs cases. We will particularly show how the growth conditions can be used to tailor the nanocrystal shape.

Then, using the SAG approach we will try to achieve, high quality GaSb and InAs nanowires grown on highly mismatched GaAs (001) substrate. We will first show the influence of the growth conditions on GaSb nanowire growth inside stripes directed along [110] and [1-10]. After the optimization of GaSb growth conditions, we will grow 10-nm thick InAs on top of these GaSb nanotemplates to achieve in-plane InAs nanowires. After GaSb selective etching in an ammonia-based solution, free standing InAs nanowires will be established.

References

1. J. Del Alamo, Nature **479**, 320, 2011.

2. B. Rajamohanan, R. Pandey, V. Chobpattana, C. Vaz, D. Gundlach, K. P. Cheung, J. Suehle, S. Stemmer and S. Datta, IEEE El. Dev. Lett. **36**, 20, 2015.

3. R. Li, Y. Lu, G. Zhou, Q. Liu, S. D. Chae, T. Vasen, W. S. Hwang, Q. Zhang, P. Fay, T. Kosel, M. Wistey, H. Xing, and A. Seabaugh, El. Dev. Lett. **33**, 363, 2012.

4. R. T. P. Lee, R. J. W. Hill, W.-Y. Loh, R-H. Baek, S. Deora, K. Matthews, C. Huffman, K. Majumdar, T. Michalak, C. Borst, P. Y. Hung, C-H. Chen, J-H. Yum, T-W. Kim, C-Y. Kang, W-E. Wang, D-H. Kim, C. Hobbs and P-D. Kirsch, IEDM 13-44, 2013.

5. A. Yariv and P. Yeh, Optical Waves in Crystals, John Wiley, New Jersey, 2003.

6. C. Ratsch and A. Zangwill, Surface Science **293,** 123-131, 1993.

7. J. W. Matthews and A. E. Blakeslee, J. Crystal Growth **27**, I 18-125, 1974.

8. Y. Wang, *Misfit dislocation and strain relaxation at large lattice mismatched III-V semiconductor interfaces*, CIMAP Caen, 2012.

9. P. M. J. Marée, J. C. Barbour, J. F. van der Veen, K. L. Kavanagh, C. W. T. Bulle-Lieuwma, and M. P. A. Viegers, J. Appl. Phys. **62**, 11, 4413, 1987.

10. A. Vilà, A. Cornet, J. R. Morante, P. Ruterana, M. Loubradou, and R. Bonnet, J. Appl. Phys. **79**, 2, 676, 1996.

11. E. Lefebvre, *Croissance métamorphique par Epitaxie par Jets Moléculaires et caractérisations physiques pour Transistor Bipolaire à Hétérojonction InP/InGaAs sur GaAs,* IEMN, 2005.

12. Y. B. Bolkhovityanov, A. S. Deryabin, A. K. Gutakovskii, and L. V. Sokolov, J. Appl. Phys. **109**, 123519, 2011.

13. W. Qian, M. Skowronski, R. Kaspi, M. De Graef, and V. P. Dravid, J. Appl. Phys. **81**, 7268, 1997.

14. A. Rocher and E. Snoeck, Mater. Sci. Eng. B, **67**, 1, 62–69, 1999.

15. P. J. Taylor, W. A. Jesser, J. D. Benson, M. Martinka, J. H. Dinan, J. Bradshaw, M. Lara-Taysing, R. P. Leavitt, G. Simonis, W. Chang, W. W. Clark, and K. A. Bertness, J. Appl. Phys. **89**, 8, 4365, 2001.

16. V. Narayanan, S. Mahajan, K. J. Bachmann, V. Woods, and N. Dietz, Acta Mater. **50**, 6, 1275–1287, 2002.

17. Z. Liliental-Weber, M. A. Okeeke and J. Washburn, Ultramicroscopy **30**, 20-26, 1989.

18. G. Wang, R. Loo, S. Takeuchi, L. Souriau, J. C. Lin, A. Moussa, H. Bender, B. De Jaeger, P. Ong, W. Lee, M. Meuris, M. Caymax, W. Vandervorst, B. Blanpain, and M. M. Heyns, Thin Solid Films **518**, 9, 2538–2541, 2010.

19. J. E. Ayers, *Heteroepitaxy of Semiconductors: Theory, Growth, and Characterization*, CRC Press 2007.

20. Gu, J. J., A. T. Neal and P. D. Ye, Appl. Phys. Lett. **99**, 152113, 2011.

21. X. Zhao, A. Vardi and J. Del Alamo, IEEE, 2014.

22. G. Balakrishnan, S. Huang, T. J. Rotter, A. Stintz, L. R. Dawson, K. J. Malloy, H. Xu, and D. L. Huffaker, Appl. Phys. Lett. **84**, 2058, 2004.

23. S. S. Yi, C. K. Inoki, D. L. Harris, T. S. Kuan, T. F. Kuech and D. M. Hansen, Appl. Phys. Lett. **77**, 842, 2000.

24. Y. C. Xin, L. G. Vaughn, L. R. Dawson, A. Stintz, Y. Lin, L. F. Lester, and D. L. Huffaker, J. Appl. Phys. **94**, 2133, 2003.

25. P. F. Marsh, C. S. Whelan, W. E. Hoke, R. E. Leoni, T. E. Kazior, Microelectronics Reliability **42,** 997, 2002.

26. H. Happy, S. Bollaert, H. Fouré and Alain Cappy, IEEE Trans. Elec. Dev. **45,** 2089, 1998.

27. W. Qian, R. Kaspi and M. Skowronski, J. Electrochem. Soc. **44,** 1430, 1997.

28. A. Bourret and P. H. Fuoss, Appl. Phys. Lett. **61,** 1034, 1992.

29. A. Trampert, E. Tournié and K. H. Ploog, Appl. Phys. Lett. **66,** 2265, 1995.

30. E. Tournié, O. Brandt, C. Giannini, K. H. Ploog and M. Hohenstein, J. Cryst. Growth **127,** 765, 1993.

31. J. C. P. Chang, T. P. Chin and J. M. Woodall, Appl. Phys. Lett. **69**, 981, 1996.

32. S. H. Huang, G. Balakrishnan, A. Khoshakhlagh, A. Jallipalli, L. R. Dawson, and D. L. Huffaker, Appl. Phys. Lett. **88,** 131911, 2006.

33. B. Brar and D. Leonard, Appl. Phys. Lett. **66**, 4, 463, 1995.

34. S. J. Brown, M. P. Grimshaw, D. A. Ritchie, and G. A. C. Jones, Appl. Phys. Lett. **69**, 10, 1468, 1996.

35. K. Akahane, N. Yamamoto, S. Gozu, and N. Ohtani, J. Cryst. Growth **264**, 1–3, 21–25, 2004.

36. Y. H. Kim, J. Y. Lee, Y. G. Noh, M. D. Kim, S. M. Cho, Y. J. Kwon, and J. E. Oh, Appl. Phys. Lett. **88**, 24, 241907, 2006.

37. R. D. Bringans, R. I. G. Uhrberg, M. A. Olmstead, and R. Z. Bachrach, Phys. Rev. B **34**, 10, 7447, 1986.

38. T. Sakamoto and G. Hashiguchi, Jpn. J. Appl. Phys. **25**, 1, L78-L80, 1986.

39. M. Kawabe and T. Ueda, Jpn. J. Appl. Phys. **26**, 6, L944-L946, 1987.

40. D. Saloner, J. A. Martin, M. C. Tringides, D. E. Savage, C. E. Aumann, and M. G. Lagally, J. Appl. Phys. **61**, 8, 2884, 1987.

41. L. Barbier, A. Khater, B. Salanon, and J. Lapujoulade, Phys. Rev. B **43**, 18, 14730, 1991.

42. A. Jallipalli, M. N. Kutty, G. Balakrishnan, J. Tatebayashi, N. Nuntawong, S. H. Huang, L. R. Dawson, D. L. Huffaker, Z. Mi, and P. Bhattacharya, Electron. Lett. **43**, 22, 1198, 2007.

43. M. Grundmann, J. Vac. Sci. Technol. B Microelectron. Nanometer Struct. **9**, 4, 2158, 1991.

44. H. Tanoto, S. F. Yoon, W. K. Loke, E. A. Fitzgerald, C. Dohrman, B. Narayanan, M. T. Doan, and C. H. Tung, J. Vac. Sci. Technol. B Microelectron. Nanometer Struct. **24**, 1, 152, 2006.

45. J. Tatebayashi, A. Jallipalli, M. N. Kutty, Shenghong Huang, K. Nunna, G. Balakrishnan, L. R. Dawson, and D. L. Huffaker, IEEE J. Sel. Top. Quantum Electron. **15**, 3, 716–723, 2009.

46. I. Németh, B. Kunert, W. Stolz, and K. Volz, J. Cryst. Growth **310**, 23, 4763–4767, 2008.

47. I. Németh, B. Kunert, W. Stolz, and K. Volz, J. Cryst. Growth **310**, 7–9, 1595–1601, 2008.

48. Y. Ping Wang, J. Stodolna, M. Bahri, J. Kuyyalil, T. Nguyen Thanh, S. Almosni, R. Bernard, R. Tremblay, M. Da Silva, A. Létoublon, T. Rohel, K. Tavernier, L. Largeau, G. Patriarche, A. Le Corre, A. Ponchet, C. Magen, C. Cornet, and O. Durand, Appl. Phys. Lett. **107**, 191603, 2015.

49. T. Nguyen Thanh, C. Robert, W. Guo, A. Letoublon, C. Cornet, G. Elias, A. Ponchet, T. Rohel, N. Bertru, A. Balocchi, O. Durand, J. S. Micha, M. Perrin, S. Loualiche, X. Marie, and A. Le Corre, J. Appl. Phys. **112**, 053521, 2012.

50. S. H. Huang, G. Balakrishnan, A. Khoshakhlagh, L. R. Dawson, and D. L. Huffaker, Appl. Phys. Lett. **93**, 7, 071102, 2008.

51. M. Paladugu, C. Merckling, R. Loo, O. Richard, H. Bender, J. Dekoster, W. Vandervorst, M. Caymax, and M. Heyns, Cryst. Growth Design **12**, 4696, 2012.

52. Y. Bogumilowicz, J. M. Hartmann, R. Cipro, R. Alcotte, M. Martin, F. Bassani, J. Moeyaert, T. Baron, J. B. Pin, X. Bao, Z. Ye, and E. Sanchez, Appl. Phys. Lett. **107**, 21, 212105, 2015.

53. K. Volz, A. Beyer, W. Witte, J. Ohlmann, I. Németh, B. Kunert, W. Stolz, J. Cryst. Growth **315,** 37–47, 2011.

54. S. Jha, C.-C. Liu, T. S. Kuan, S. E. Babcock, P. F. Nealey, J. H. Park, L. J. Mawst, and T. F. Kuech, Appl. Phys. Lett. **95**, 6, 062104, 2009.
55. S. Jha, M. K. Wiedmann, T. S. Kuan, X. Song, S. E. Babcock, and T. F. Kuech, J. Cryst. Growth **315**, 1, 91–95, 2011.
56. Q. Li, S. Huang, D. Pan, J. Wang, J. Zhao and H. Q. Xu, Appl. Phys. Lett. **105**, 113106, 2014.
57. A. M. Burke, D. J. Carrad, J. G. Gluschke, K. Storm, S. Fahlvik Svensson, H. Linke, L. Samuelson and A. P. Micolich, Nano Lett. **15**, 2836−2843, 2015.
58. K.Tomioka, F. Izhizaka, and T. Fukui, Nano Lett. **15**, 7253−7257, 2015.
59. C. Thelander, P. Caroff, S. Plissard, A.W. Dey and K.A. Dick, Nano Lett. **11**, 2424, 2011.
60. H. Schmid, M. Borg, K. Moselund, L. Gignac, C. M. Breslin, J. Bruley, D. Cutaia, and H. Riel, Appl. Phys. Lett. **106**, 233101, 2015.
61. M. A. Wistey, A. K. Baraskar, U. Singisetti, G. J. Burek, B. Shin, E. Kim, P. C. McIntyre, A. C. Gossard and M. J. W. Rodwell, J. Vac. Sci. Technol. B **33**, 011208, 2015.
62. W. Qian, M. Skowronski, and R. Kaspi, J. Electrochem. Soc. **144**, 4, 1430–1434, 1997.
63. M. B. Panish and H. Temkin, Gas source molecular beam epitaxy: Growth and properties of phosphorus-containing III–V heterostructures, Springer series in material science **26**, 1993.
64. S. C. Lee, K. J. Malloy, L. R. Dawson, and S. R. J. Brueck, J. Appl. Phys. **92**, 6567, 2002.
65. S. C. Lee, L. R. Dawson, and S. R. J. Brueck, J. Appl. Phys. **96**, 4856, 2004.
66. A. Okamoto, Semicond. Sci. Technol. **8**, 1011-1015, 1993.
67. S. S. Yi, D. M. Hansen, C. K. Inoki, D. L. Harris, T.S. Kuan, T. F. Kuech, Appl. Phys. Lett. **77**, 842, 2000.
68. J.H. Kim, T.Y. Seong, N. J. Mason, P. J. Walker, J. Electron. Mater. **27**, 466–471, 1998.
69. T. Sugaya, Y. Okada, and M. Kawabe, Jpn. J. Appl. Phys. **31**, Part 2, 6A, L713-L716, 1992.
70. N. Kuroda, S. Sugou, T. Sasaki, and M. Kitamura, Jpn. J. Appl. Phys. **32**, Part 2, 11A, L1627-L1630, 1993.
71. D. R. Lide, CRC handbook of chemistry and physics. CRC press, 2004.
72. R. Kobayashi, K. Fujii, and F. Hasegawa, Jpn. J. Appl. Phys. **30**, L1447-L1449, 1991.
73. R. Z. Bachrach and R. D. Bringans, J. Vac. Sci. Technol. B **1**, 142-145, 1983.
74. G.J. Bauhuis, P. Mulder, H. van Kempen, J. Cryst. Growth **240**, 104-111, 2002.
75. T. Ujihara, Y. Yoshida, W. Sik Lee, Y. Takeda, J. Cryst. Growth **289**, 89-95, 2006.
76. D. Coronell, K. Jensen, J. Cryst. Growth **114**, 581, 1991.

77. J. Yuan, H. Wang, P. J. van Veldhoven, and R. Nötzel, J. Appl. Phys. **106**, 12, 124304, 2009.

78. D. Zhou, S. Anantathanasarn, P. J. van Veldhoven, F. W. M. van Otten, T. J. Eijkemans, T. de Vries, E. Smalbrugge, and R. Nötzel, Appl. Phys. Lett. **91**, 13, 131102, 2007.

79. H. J. Kim, J. Motohisa, and T. Fukui, Nanotechnology **15**, 3, 292, 2004.

80. E. D. Williams and N. C. Bartelt, Ultramicroscopy **31**, 1, 36-48, 1989.

81. C. Rotfman and M. Wortis, Phys. Rep. **103**, Nos. 1-4, 59-79, 1984.

82. S. C. Lee, D. L. Huffaker, and S. R. J. Brueck, Appl. Phys. Lett. **92**, 2, 023103, 2008.

83. P.-S. Wong, B. Liang, R. Molecke, J. Tatebayashi, and D. L. Huffaker, Cryst. Growth Des. **10**, 6, 2509–2514, 2010.

84. S. C. Lee, L. R. Dawson, and S. R. J. Brueck, Appl. Phys. Lett. **87**, 7, 071110, 2005.

85. H. Heinecke, B. Baur, A. Miklis, R. Matz, C. Cremer and R. Höger, J. Cryst. Growth **124**, 186-191, 1992.

86. H. Heinecke, B. Baur, R. Schimpe, R. Matz, C. Cremer, R. Höger and A. Miklis, J. Cryst. Growth **120**, 370-381, 1992.

87. M. Wachter, H. Heinecke, J. Cryst. Growth **164**, 302-307, 1996.

88. O. Kayser, J. Cryst. Growth **107**, 989-998, 1991.

89. Z. Wang, B. Tian, M. Pantouvaki, W. Guo, P. Absil, J. Van Campenhout, C. Merckling, and D. Van Thourhout, Nat. Photonics **9**, 837-842, 2015.

90. R. Cipro, T. Baron, M. Martin, J. Moeyaert, S. David, V. Gorbenko, F. Bassani, Y. Bogumilowicz, J. P. Barnes, N. Rochat, V. Loup, C. Vizioz, N. Allouti, N. Chauvin, X. Y. Bao, Z. Ye, J. B. Pin, and E. Sanchez, Appl. Phys. Lett. **104**, 26, 262103, 2014.

91. J. Z. Li, J. Bai, J.-S. Park, B. Adekore, K. Fox, M. Carroll, A. Lochtefeld, and Z. Shellenbarger, Appl. Phys. Lett. **91**, 021114, 2007.

92. M. Paladugu, C. Merckling, R. Loo, O. Richard, H. Bender, J. Dekoster, W. Vandervorst, M. Caymax, and M. Heyns, Cryst. Growth Des. **12**, 10, 4696-4702, 2012.

93. C. Renard, N. Cherkasin, A. Jaffre, L. Vincent, A. Michel, T. Molière, R. Hamouche, V. Yam, J. Alvarez, F. Fossard, D. Mencaraglia and D. Bouchier, Appl. Phys. Letters **102**, 191915, 2013.

94. C. Renard, T. Molière, N. Cherkashin, J. Alvarez, L. Vincent, A. Jaffré, G. Hallais, J. P. Connolly, D. Mencaraglia and D. Bouchier, Scientific Reports **6**, 25328, 2016.

95. S. S. Yi, D. M. Hansen, C. K. Inoki, D. L. Harris, T. S. Kuan, and T. F. Kuech, Appl. Phys. Lett. **77**, 6, 842, 2000.

96. C. Hsu, Y. Chen and Y. Su, Nanotechnology **23**, 495306, 6pp, 2012.

97. G. Suryanarayanan, A. A. Khandekar, T. F. Kuech, S. E. Babcock, Appl. Phys. Lett. **83**, 1977, 2003.

98. N. Moll, A. Kley, E. Pehlke, and M. Scheffler, Phys. Rev. B **54**, 12, 8844, 1996.

99. B. Korgel, R. F. Hicks, J. Crystal Growth **151,** 204-212, 1995.

100. D. G. Coronell and K. F. Jensen, J. Cryst. Growth **114**, 581-592, 1991.

101. S. Jiang, C. Merckling, W. Guo, N. Waldron, M. Caymax, W. Vandervorst, M. Seefeldt, and M. Heyns, J. Appl. Phys. **115**, 2, 023517, 2014.

102. N. Moll, M. Scheffler, and E. Pehlke, ArXiv Prepr. Cond-Mat 9807200, 1998.

103. G. Wulf, Z. Kristallogr. **34**, 449, 1901.

104. P. Müller and R. Kern, Surf. Sci. **457**, 1, 229-253, 2000.

105. L. Vescan, J. Vac. Sci. Technol. B Microelectron. Nanometer Struct. **16**, 3, 1549, 1998.

106. T. Sato, I. Tamai, and H. Hasegawa, J. Vac. Sci. Technol. B Microelectron. Nanometer Struct. **22**, 4, 2266, 2004.

107. D. Dutartre, B. Seiss, Y. Campidelli, D. Pellissier-Tanon, D. Barge, and R. Pantel, Thin Solid Films, **520**, 8, 3163-3169, 2012.

108. C. Pribat and D. Dutartre, J. Cryst. Growth **334**, 1, 138-145, 2011.

109. B. Seiss and D. Dutartre, Solid-State Electron. **83**, 18–24, 2013.

110. M. Hata, T. Isu, A. Watanabe, and Y. Katayama, Appl. Phys. Lett. **56**, 25, 2542-2544, 1990.

111. M. Hata, T. Isu, A. Watanabe, and Y. Katayama, J. Vac. Sci. Technol. B **8**, 4, 692-696, 1990.

112. X. Q. Shen, M. Tanaka, and T. Nishinaga, J. Cryst. Growth **127**, 1, 932-936, 1993.

113. X. Q. Shen, M. Tanaka, K. Wada, and T. Nishinaga, J. Cryst. Growth **135**, 1, 85-96, 1994.

114. M. Hata, A. Watanabe, and T. Isu, J. Cryst. Growth **111**, 83-87, 1991.

115. M. Ohtsuka, J. Cryst. Growth **205**, 1–2, 112-122, 1999.

116. T. Ujihara, Y. Yoshida, W. Sik Lee, and Y. Takeda, J. Cryst. Growth **289**, 1, 89-95, 2006.

117. X. Q. Shen, D. Kishimoto, and T. Nishinaga, Jpn. J. Appl. Phys. **33**, 11-17, 1994.

CHAPTER II: Experimental setup

In this chapter, we first introduce the Molecular Beam Epitaxy (MBE) systems in which the samples were grown. As this work deals with selective area growth (SAG), we then focus on the *ex-situ* and *in-situ* preparation of the patterns. Finally, we present the morphological and structural characterization techniques used in this study.

1. MBE Growth

MBE is a technique allowing the growth of single crystal layers. It has been developed by J. Arthur and A. Cho [1-2] in the 1970s, based on the principle of the three temperatures proposed by Gunther in 1958 [3]. The process consists in making group V molecular flux react with another group III one evaporated at temperatures T_V and T_{III}, respectively, on a substrate surface heated at a temperature T_s satisfying $\mathbf{T_{III} > T_s > T_V}$. In these conditions, group-III atoms condense on the surface whereas group-V ones only incorporate in the presence of group-III ones making III-V bonds. Therefore, the growth rate is controlled by the group-III element flux, whereas growth is performed under an excess of group-V element to ensure the stoichiometry of the grown layer.

The main benefits of MBE as compared to other growth techniques are:

- A low growth rate, allowing an excellent control of heterostructure thickness and interfaces.
- An ultrahigh vacuum environment leading to high-purity materials and suitable for in-situ growth monitoring by reflection high-energy electron diffraction (RHEED)

1.1. IEMN MBE systems

The samples are elaborated in two chambers dedicated for III-V material growth: a Solid-Source MBE (SSMBE) RIBER 21 TM reactor and a Gas-Source (GSMBE) MBE 32 P reactor, coupled together under ultra-high vacuum and running with a base pressure better than 10^{-10} Torr [4]. These two growth chambers are also coupled with an ESCA analysis chamber (figure II.1). A III-V MBE system consists in four main vacuum chambers: introduction chamber, outgassing chamber, intermediate chamber, and growth chamber. These chambers are separated from each other by gate valves to maintain the vacuum integrity between them [4].

The group-III element effusion cells (Ga, Al and In) are similar in the SSMBE and GSMBE reactors. For the group-V element (P, As, Sb), no phosphorus cell was installed in the SSMBE chamber during this PhD. On the other hand, an As solid cracker cell is used on the SSMBE to produce As_4 or As_2 (depending on the cracker temperature) whereas an arsine/phosphine high-temperature gas injector delivers As_2/P_2 species in the GSMBE.

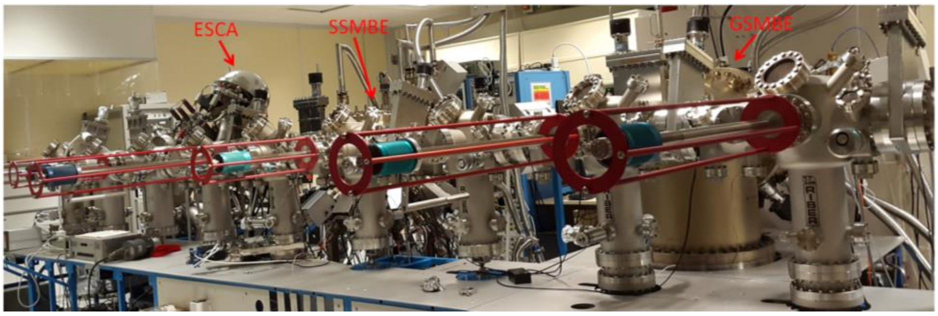

Figure II.1: IEMN III-V SSMBE and GSMBE reactors coupled together to the ESCA analysis chamber.

In the SSMBE reactor, a hydrogen plasma cell is installed, which dissociates molecular hydrogen in the cavity of the cell thanks to a plasma discharge generated by the inductive coupling of an RF excitation coil. During this work, we have typically used a power of 400 W with a 3 sccm hydrogen flow.

1.2. Growth monitoring

1.2.1. In-situ characterization: Reflection high-energy electron diffraction (RHEED)

The RHEED is one of the very useful tools for in-situ monitoring of the growth. It provides feedbacks on the surface morphology (for instance during oxide removal from the surface), as well as on the lattice constant, and growth rate. The RHEED gun emits high energy electrons (15 keV for SSMBE and 20 keV for GSMBE reactors) which strike the surface with a small angle (~1°) [4].

a) Flux calibration

By means of a camera placed in front of RHEED screen, instantaneous pictures or intensities can be recorded as a function of time. The RHEED Specular Beam Intensity (SBI) oscillations can be used as a measurement of the growth rates in MBE [4].

These RHEED oscillations were first used by Neave et al. [5] where the oscillation frequency corresponds to the monolayer growth rate of the epilayer [6]. For example, to calibrate the Ga growth rate, at a defined Ga cell and substrate temperatures, we use a GaAs substrate. Then, we fix the As flux high enough to maintain RHEED oscillations but also low enough to reduce oscillation damping. The period of the SBI oscillations corresponds exactly to a complete layer of GaAs in the [001] direction. Once the Ga growth rate is calibrated, we fix it and decrease the As flux until the oscillations rapidly disappear. This method allows us calibrating all group-III and V element growth rates on different substrates (GaAs, InAs and GaSb). For day to day control, the atomic flux is checked with the help of a Bayart-Alpert gauge placed in front of the substrate holder.

b) Surface reconstruction

In addition to growth rate calibration, the RHEED is used to know the surface reconstruction during growth. The surface reconstructions are fairly well known for III-V semiconductors. They depend on the temperature of the substrate and flux conditions. There are phase diagrams giving the surface reconstruction changes with the growth parameters [7]. As we will present in chapter III, the surface energies of the (001) facets are calculated for different reconstructions which can be known from the RHEED pattern. For example for InP growth on (001) surfaces, whatever the P/In flux ratio, we always observe a (2x4) diagram, that can be ascribed either to the β2(2x4) or to the mixed dimer reconstruction of the (001) surface but not to the c(4x4) one, which would result in a (2x2) diagram [8].

1.2.2. Temperature calibration

The substrate is heated by the radiation of a filament heater regulated via a thermocouple. The surface temperature is controlled via an optical pyrometer installed in front of the sample in a way that it measures precisely the thermal radiation coming only from the middle of the sample surface. The temperature calibration is performed against the melting point of a small piece of InSb (520 ± 5°C) taken as a reference. The precise detection of InSb melting is realized with the help of the RHEED system.

2. Sample preparation

In this work, SAG has been investigated on InP, InAs and GaAs. For InAs we have used pseudo-substrates consisting in a 1 µm-thick relaxed InAs layer grown on a semi-insulating GaAs (001) substrate. A thin 30 nm GaSb layer is used to accommodate the mismatch between GaAs and InAs. Figure II.2 displays the D-XRD experimental spectrum of the InAs layer together with the simulated one. These spectra show that the InAs layer is totally relaxed on the GaAs substrate.

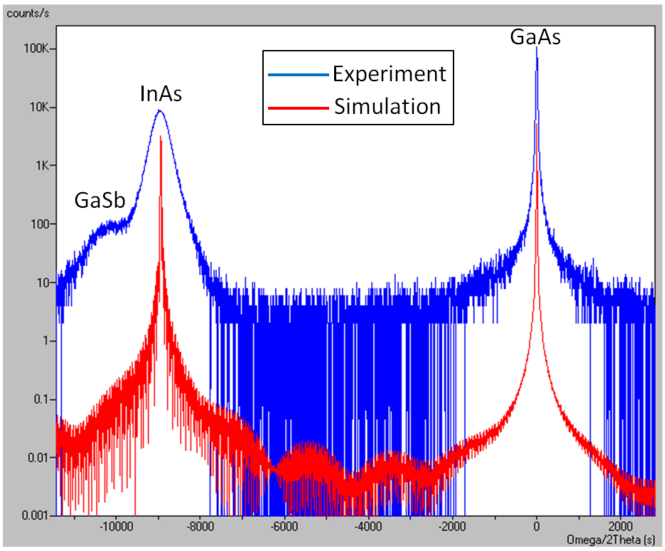

Figure II.2. (004) ω-2θ D-XRD spectrum with the simulated one recorded on a 1 µm-thick relaxed InAs layer grown on a semi-insulating GaAs (001) substrate.

2.1. Pattern elaboration

The nature of the oxide layer used for masking may be crucial for the selectivity as it could affect the strength of the bonds formed with the III and V-element atoms. 10 nm-thick amorphous SiO_2 and Al_2O_3 masks have been investigated in this work and deposited on an InP(001) substrate. Whereas plasma-enhanced chemical vapor deposition (PECVD) is used for SiO_2 deposition, the Al_2O_3 mask is grown by atomic layer deposition (ALD). In order to test the polycrystalline deposition on the mask, 50 nm of InAs is deposited at a growth temperature (GT) of 470 °C and with an As/In flux ratio of 2.5. Figures III.3(a and b) show the SEM images after the growth on a SiO_2 and Al_2O_3 mask, respectively. Polycrystalline InAs covers almost all the Al_2O_3 mask in contrast to the SiO_2 one. For this reason and considering that SiO_2 is quite stable at high GT [9], we will use SiO_2 mask for SAG in the following.

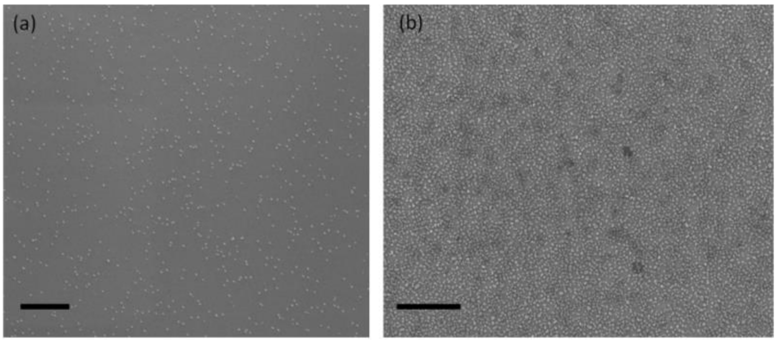

Figure II.3. SEM images recorded after deposition of 50 nm InAs on a SiO_2 (a) or Al_2O_3 (b) mask. The scale bar represents 2 µm.

Figure II.4 shows a schematic representation of the sample preparation before the growth. A 30 nm-thick SiO_2 layer (n=1.45) is first deposited by PECVD at a temperature of 300°C. Then a 100 nm-thick resist layer (PMMA 495K 3% type) is deposited on the oxide using a spin coating setup. The substrate is annealed at 180°C for 30 min to evaporate the solvent. Electron beam (EB) lithography is used to define patterns of different sizes in the resist layer. The electrons are accelerated by a potential difference of 100 kV. We adjust the nominal dose of the EB irradiation to 280 $\mu C/cm^2$.

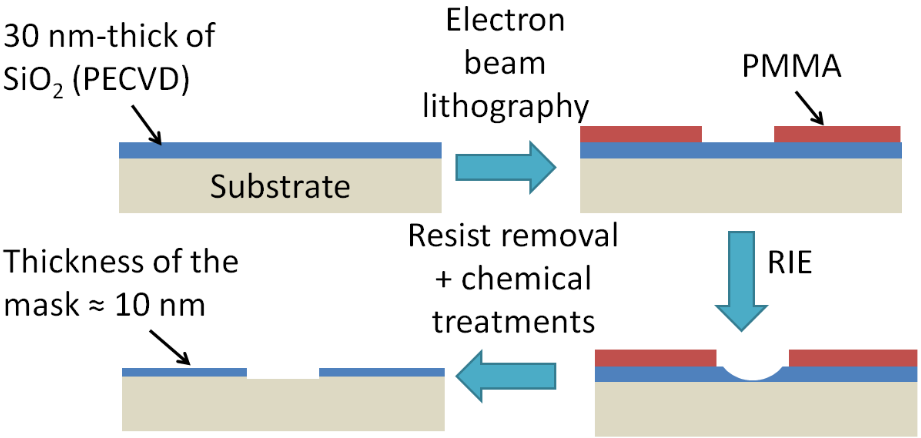

Figure II.4. Schematic representation of the sample preparation before the growth.

All our patterns are prepared using LayoutEditor software. The writing time is about 1 or 2 hours/inch. However, for special masks with dense patterns prepared for X-ray diffraction (XRD) characterization (see chapter 4), the writing time is about 10-15 hours/inch. In this case the pattern covers almost 10% of the sample area. Since we use a positive resist with a high molecular weight, the irradiation of the resist with the EB decreases the size of the polymer chains which makes the resist soluble in the organic solvent (Methyl isobutyl ketone (MIBK)). The remaining resist is used as a mask for silicon oxide etching. By means of reactive ion etching (RIE), the SiO_2 layer is partially removed inside the patterns so that the remaining thin oxide layer protects the substrate surface from damage and contamination during the solvent and oxygen plasma–cleaning step for resist removal. Just before the introduction of the sample under ultra-high vacuum, the patterns are fully opened via chemical etching (30 s in a hydrofluoric acid (HF) 1% solution). Finally, the thickness of the mask is about 10 nm [8-10].

2.2. Surface cleaning in MBE chamber

For each growth run, both a patterned sample and a bare one are In soldered on the same sample holder to allow RHEED observations and control the surface evolution during

III-V surface deoxidization. The III-V native oxide layer inside the SiO_2 apertures is removed by thermal annealing under corresponding V-element combined or not with an atomic hydrogen flux in the MBE chamber. Table II.1 shows the deoxidization used for different experiments in this work.

In order to check the benefit of the atomic hydrogen flux for the GaAs surface cleaning, three different deoxidization procedures were tested. Then the sample surfaces were examined by atomic force microscopy (AFM) (see section 3.1).

Table II.1. Deoxidization procedures for growth systems performed in this work.

Bare substrate	Grown layer	Deoxidization
InP	InP	Thermal annealing under phosphorus flux at 525-530°C
InAs	InAs	Thermal annealing under arsenic flux at 520°C
GaAs	GaAs	Thermal annealing under arsenic flux at 620-640°C
	GaSb	Thermal annealing under combined atomic hydrogen and antimony fluxes at 450°C

The first surface deoxidization was a thermal annealing under arsenic flux at 620-640°C, for which AFM observation (figure II.5(a)) reveals a rough surface. The RMS roughness calculated from the image is about 2.45 nm. The second surface deoxidization was a thermal annealing under combined atomic hydrogen and arsenic fluxes at 450°C, the AFM image exhibiting a smooth surface (RMS = 0.34 nm) (figure II.5(b)). The third surface deoxidization was a thermal annealing under combined atomic hydrogen and antimony fluxes at 450°C, the AFM image exhibiting also a smooth surface with an even better RMS of 0.28 nm (figure II.5(c)). The combination of Sb and atomic hydrogen fluxes with a deoxidization temperature of 450°C improves the surface roughness.

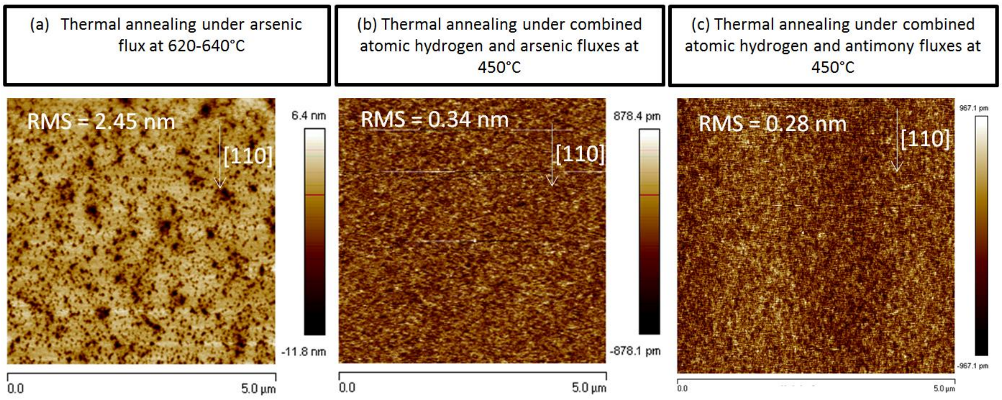

Figure II.5: (5x5) μm^2 AFM images of deoxidized surfaces upon thermal annealing under arsenic at 620-640°C (a), thermal annealing under combined atomic hydrogen and arsenic fluxes at 450°C (b), and thermal annealing under combined atomic hydrogen and antimony fluxes at 450°C (c).

Before *ex-situ* AFM observations, these 3 samples have been characterized by *in-situ* X-ray photoemission spectroscopy (XPS) to examine the composition of the surfaces after deoxidization (figure II.6). No major difference is detected regarding the surface composition for the deoxidization procedures under arsenic whereas antimony signal appears when the deoxidization is done under antimony. However, in all cases, no carbon or oxygen traces can be detected and Ga and As oxides have been efficiently removed (figure II.6 b and c). Therefore, thanks to the atomic hydrogen flux during the deoxidization, a clean GaAs surface without oxygen and carbon can be obtained at a lower annealing temperature, which results in a smoother surface.

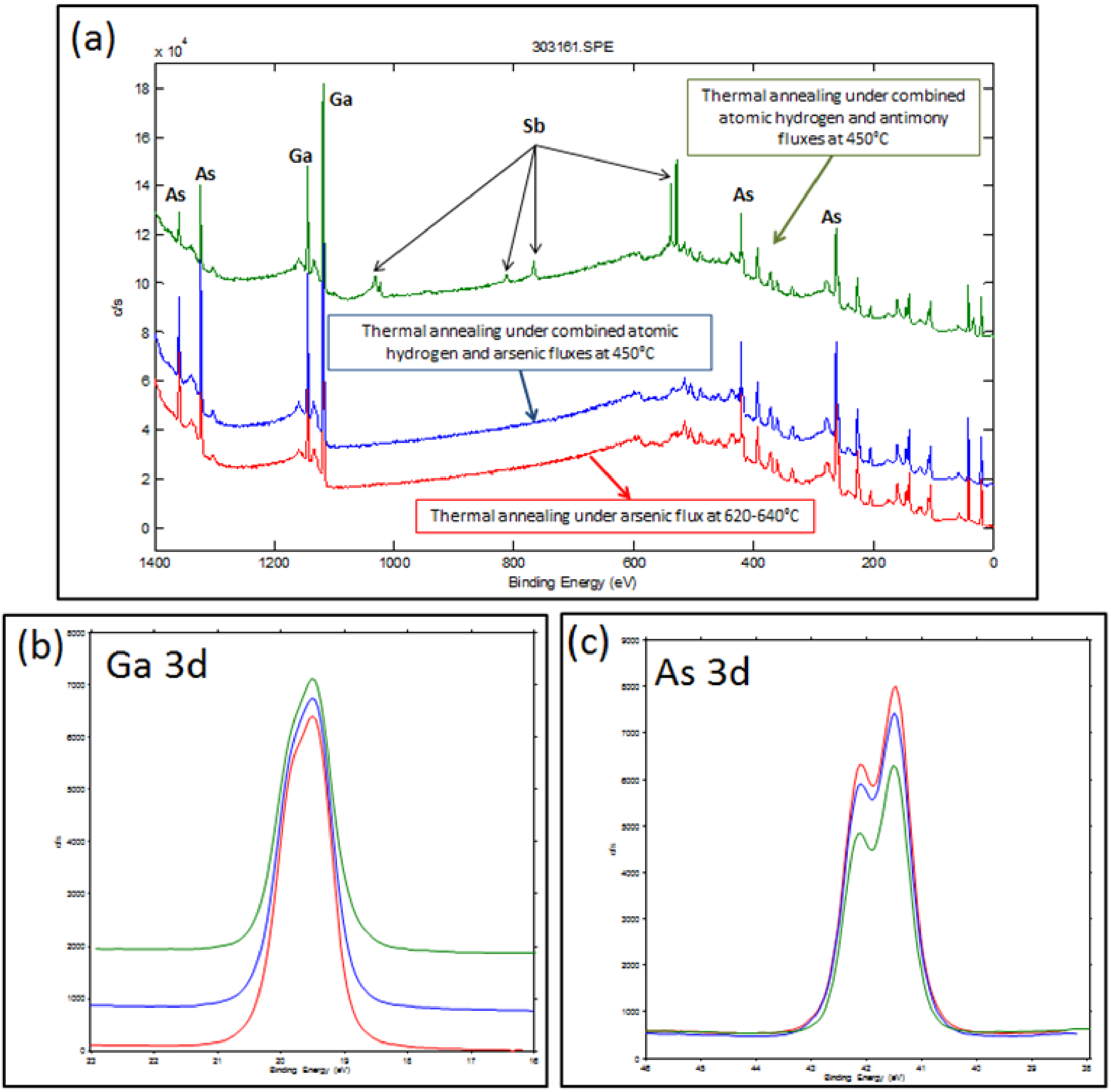

Figure II.6: XPS spectra of GaAs deoxidized surfaces (a) and Ga 3d (b) and As 3d (c) core level spectra upon thermal annealing under arsenic at 620-640°C (red), thermal annealing under combined atomic hydrogen and arsenic fluxes at 450°C (blue), and thermal annealing under combined atomic hydrogen and antimony fluxes at 450°C (green).

3. Material characterization

After the epitaxial growth, scanning electron microscopy (SEM), atomic force microscopy (AFM), scanning transmission electron microscopy coupled with focused ion beam preparation (STEM-FIB), transmission electron microscopy (TEM), and X-ray diffraction (XRD) are carried out to analyze the morphological and structural characteristics of the epitaxially grown material.

3.1. Morphological characterization

The nanostructure morphology is examined by SEM using a Zeiss Ultra 55 system. The SEM plan view is used to give a rapid feedback on the selectivity, the in-plane morphology of the nanostructures in both crystallographic directions. Moreover, the SEM cross-section view allows primary information on the crystal shape inside the stripes before performing the FIB-STEM observations described below.

Some sample surfaces are examined by AFM using a Picoforce system, working in the tapping mode. This tool gives information about the surface topology with a resolution that can reach atomic step in the direction perpendicular to the sample surface (figure II.7(a)). Regarding SAG, a disadvantage of AFM measurement is faced when important thickness changes are analyzed (> 40 nm). As the tip shape is pyramidal, when it confronts a facet which is perpendicular to the sample surface, the shape given by AFM will be different from the real shape of the pattern. Consequently, the nanostructure shapes determined in the AFM images will be different from the real ones. Figure II.7(b) shows a schematic example of the AFM tip path (dashed lines) on a patterned substrate. With the help of the AFM, we measured the nanostructure average length and height inside the patterns but we cannot define the facet orientation.

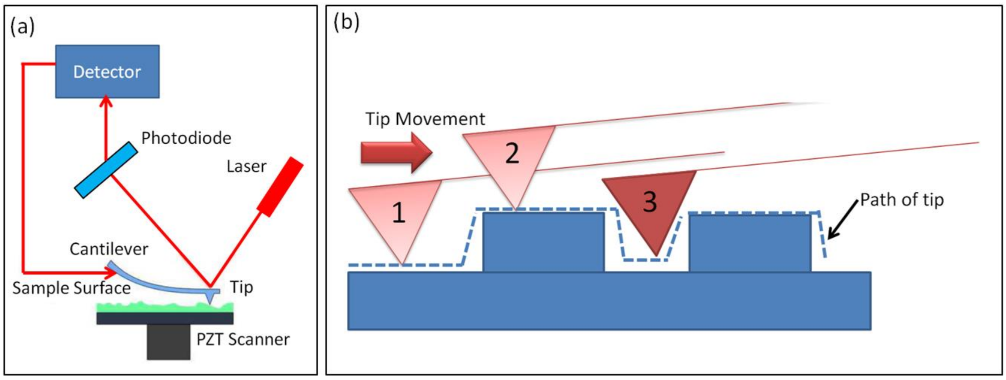

Figure II.7: Schematic of an atomic force microscope (a), Schematic of tip movement on a patterned substrate (b).

A Focused Ion Beam (FIB) system is used to create very precise cross sections of a sample for subsequent imaging via Scanning Transmission Electron Microscopy (STEM). In addition to the conventional SEM, the STEM gives an image with more precise details.

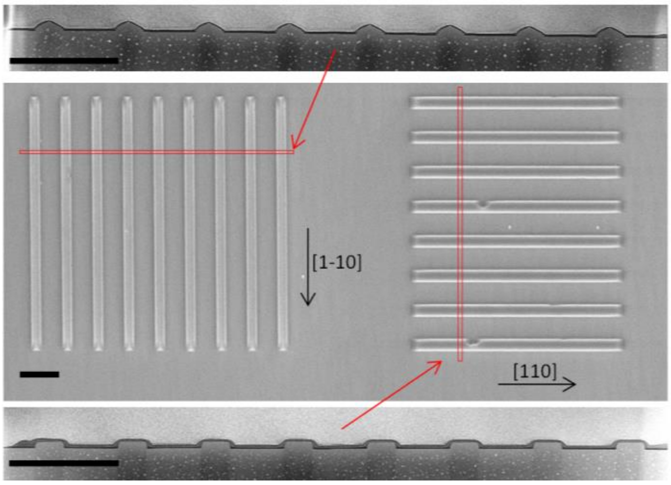

Figure II.8: SEM and FIB-STEM images of InAs sample representing the transversal cross-section lamellas direction with respect to the stipes direction. The scale bar represents 2 µm.

Unlike an electron microscope, FIB is inherently destructive to the specimen. A lamella is extracted by an in-situ lift-out with low-energy gallium ions. To avoid structure damages, the surface is coated by carbon before etching. The FIB preparations were performed at IEMN by Dr. David Troadec. A typical example of the lamella direction relative to the stripe direction is shown in figure II.8 (red lines). The length, width, and depth of the lamellas are about 10 µm, 200 nm, and 4 µm, respectively. The FIB-STEM images give a total description of nanocrystal faceting.

FIB is used to prepare longitudinal cross-section lamellas for both stripe directions. Figure II.9 presents the useful steps in order to achieve these lamellas. Platinum drops are first deposited by electron beam (EB) on the pattern in which the lamella will be done (figure II.9(a)). Then, two crosses of carbon are placed on the first and last platinum drops (figure II.9(b)). We use the carbon to get a color contrast with the platinum when the lamella thinning is carried out. Finally, we deposited a layer of platinum by ion beam (IB) covering the platinum drops and the two crosses. Figures II.9(c-e) show the FIB-STEM images of the lamella thinning procedure. The crosses can be seen as two black dots in both sides of the stripe. When the lamella thinning proceeds, the black dots of each stripe side get closer. The center of the window is reached once the platinum drops deposited by EB appear.

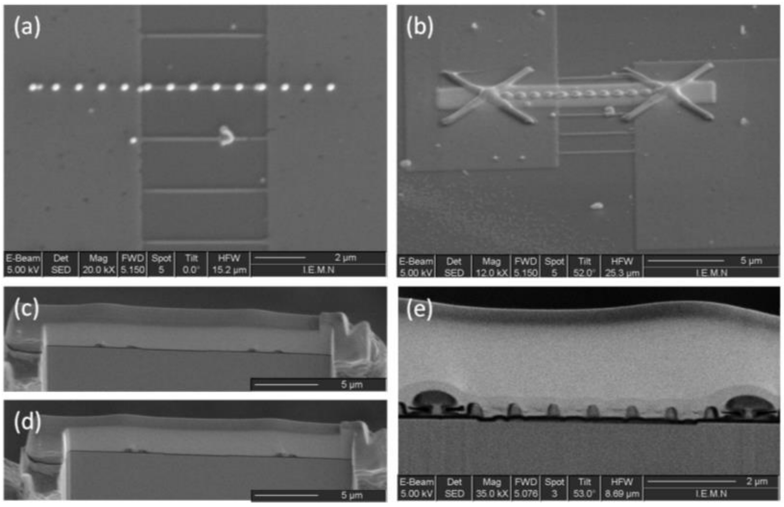

Figure II.9: FIB-STEM images of InAs/GaSb/GaAs sample representing the longitudinal lamella preparation.

3.2. Structural characterization

The structural analysis has been performed for the case of heteroepitaxy. The samples were first analyzed using XRD. In order to get local information at the atomic scale and complete the information given by the XRD measurements, the samples were analyzed by Transmission Electron Microscopy (TEM). The TEM analyses were performed at Centre de Nanosciences et de Nanotechnologies (C2N) in Marcoussis by Dr. G. Patriarche. The TEM studies were performed on a Titan Themis 200 (FEI) microscope equipped with a spherical aberration corrector on the probe and the EDX analysis system super X (0.7 srad solid angle of collection). The accelerative voltage was 200 kV. The (half) convergence angle of the probe was 17.6 mrad and the probe current 85 pA. The half-angles of collection for the annular dark field detector were respectively 69 mrad (inner) and 200 mrad (outter).

3.2.1. X-Ray Diffraction: principle and experimental setup

XRD is a powerful tool for the nondestructive investigation of heterostructures. This technique is based on the elastic scattering of X-ray radiation by the crystal lattice structure and the collection of scattered signal by an open detector or a crystal analyzer. The information of crystal structure and the distance between two scattering crystal planes can be obtained by the Bragg Law:

$$2d \sin\theta_B = n\lambda \qquad \text{(Eq.II.1)}$$

where λ is the X-ray wavelength, θ_B is the angle between the incident x-ray beam and the surface of a set of scattering planes (Bragg angle) and d is the spacing between the planes.

XRD is a non-destructive technique and does not require sample preparation as TEM. It delivers information averaged over a large sample area contrarily to the TEM which provides local structural information.

The XRD measurements are performed using a Panalytical X'Pert MRD system. A monochromator is placed after the X-ray source (λ=1.5406 Å). The incidence angle Ω, the diffraction angle 2θ, the rotation angle around the surface normal Φ, and the rotation angle around an in-plane surface direction Ψ can all be varied independently (figure II.10). Two types of XRD measurements are done, either in double X-ray diffraction (D-XRD) or in triple-axis X-ray diffraction (T-XRD). The D-XRD and T-XRD configurations used in this work are shown in figure II.10(a and b), respectively. In the D-XRD setup, the detector does not discriminate between different diffraction angles 2θ and collect scattered X-rays for different 2θ values within a rather wide range (1°)(figure II.10a, green arrows). In the T-XRD setup, an analyzer crystal filters the scattered X-rays, reducing the angular acceptance of the detector within a very narrow range of 2θ values (0.015°) (figure II.10b, black arrow). There are two modes of operation for T-XRD: the diffraction profile mode and the mapping mode.

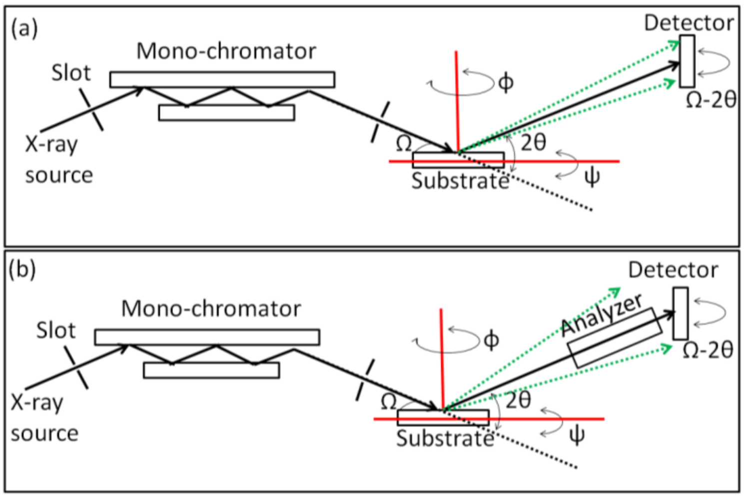

Figure II.10: Schematic view of double x-ray (a) and triple-axis x-ray (b) diffractometry used in this work. (Ω is x-ray incident angle, Φ is rotation angle, Ψ is tilt angle).

3.2.2. XRD Analysis

The XRD measurements are performed in order to determine the lattice parameters of the grown layer in the three main crystallographic directions and to qualify the structural quality of the epitaxial film using the full width at half maximum (FWHM) of the XRD peak.

a) Determination of epitaxial film lattice parameters

The crystal has three main crystallographic directions, two are parallel to the surface and one is perpendicular to it. The two lattice parameters, within the surface plane, belonging to [110] and [1-10] directions for a (001) substrate are referred to a_{110} and a_{1-10} respectively. On the other hand, the lattice parameter in the growth direction is called a_{001}. These lattice parameters provide information about the lattice relaxation (R) in mismatched heteroepitaxial layers.

The determination of the lattice parameter and layer relaxation requires to record symmetric and asymmetric reciprocal space maps (RSM) in T-XRD geometry [11-12]. This method is particularly well adapted for 2D layers with thickness above a few hundreds of nanometers. However, this method is rather time consuming when the lattice mismatch is large. Moreover, for rather thin and non-continuous layers as those considered in this work dealing with SAG, the signal/noise ratio corresponding to the epilayer is rather poor and makes this method not suitable. That is why for this kind of samples, we preferred using (2±20) reflections in grazing incidence geometry (GIXD). From the (220) and (2-20) reflections we find the epilayer lattice parameter a_{110} and a_{1-10}. Figure II.11 schematically represents the sample position with respect to the GIXD in order to get information of the diffracted planes [2-20] and [220].

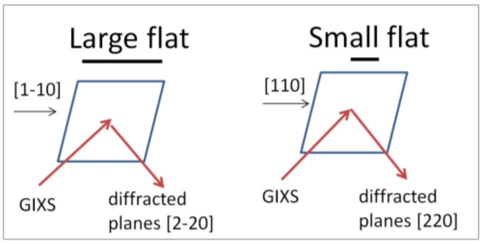

Figure II.11. The sample positions with respect to the X-Ray beam.

We can then obtain the 2 in-plane strain components, ε_{110} and ε_{1-10}, and relate them to the strain along the growth direction, ε_{001}, as a function of the stiffness tensor for cubic crystal (C_{11}, C_{12}, and C_{44}) using Hooke's Law:

$$\begin{cases} \varepsilon_{110} = \dfrac{a_{110} - a_{layer}}{a_{layer}} \\ \varepsilon_{1-10} = \dfrac{a_{1-10} - a_{layer}}{a_{layer}} \\ \varepsilon_{001} = -\dfrac{C_{12}}{C_{11}}(\varepsilon_{110} + \varepsilon_{1-10}) \end{cases} \qquad \text{(Eq.II.2)}$$

where a_{layer} is the lattice constant of the fully relaxed epilayer, and $a_{1\pm10}$ is calculated as followed:

$$a_{(1\pm10)} = \frac{2.\lambda}{\sin(\theta_{Bsubstrate} - \Delta\theta)} \qquad \text{(Eq.II.3)}$$

where the $\theta_{Bsubstrate}$ is obtained from Bragg Law and Δθ is the difference between layer and substrate peak positions. Thus now the coefficients $R_{1\pm10}$ are given by:

$$R_{1\mp10} = \frac{a_{1\pm10} - a_{substrate}}{a_{layer} - a_{substrate}} \qquad \text{(Eq.II.4)}$$

where $a_{substrate}$ is the substrate lattice constant.

The coefficient R_{004} is given by:

$$R_{(004)} = \left(1 - \frac{a_{001} - a_{layer}}{a_{001max} - a_{layer}}\right) \qquad \text{(Eq.II.5)}$$

Where a_{001max} is the lattice parameter in the growth direction for the pure pseudomorphic case ($R_{1\pm10}$ = 0 %) and defined by:

$$a_{001max} = a_{substrate} + \left(1 + \frac{2.C_{12}}{C_{11}}\right).\left(a_{layer} - a_{substrate}\right) \qquad \text{(Eq.II.6)}$$

a_{001} can be calculated in two ways:

- either from the (004) XRD spectra by means of:

$$a_{(001)} = \frac{2.\lambda}{\sin(\theta_{Bsubstrate} - \Delta\theta)} \qquad \text{(Eq.II.7)}$$

- or from the strains ε in (110), and (1-10) directions as following:

$$a_{001} = a_{layer} \,.(1 - \frac{C_{12}}{C_{11}}(\varepsilon_{110} + \varepsilon_{1-10})) \qquad \text{(Eq.II.8)}$$

b) Crystalline quality

The FWHM of an XRD peak is the most common way to characterize the structural quality of an epitaxial film. The primary approach of such a broadening analysis has been proposed, in the 1990s, by Williamson and Hall [13]. Also, Ayers proposed the same model to obtain the TDD in the epitaxial films. The weak point of the Williamson and Hall Model (WHM) is that it ignores the MDs [14]. Since for low mismatched films, the density of MDs at the interface is not significant, the WHM can be used to analyze crystal quality, as is confirmed by Nguyen et al. and Guo et al. [15-16].

For highly relaxed mismatched films it is not obvious to disregard the MD contribution. Ferrari et al. and Kaganer et al. have suggested an extended version of the WHM stressing the fact that the broadening is due to both TDs and MDs, otherwise the model leads to a wrong evaluation of the dislocation density [17-18]. Therefore, they assume that in the case of highly mismatched films, since the density of MDs is much higher than that of TDs [19-20], the broadening is mainly related to the MDs. In the following we present a summary of these two models.

Williamson-Hall model

Assuming that the measured D-XRD peaks are Gaussian, with a full width at half maximum $B_m(hkl)$ (for (hkl) reflection) and can be represented by the convolution of Gaussian intensity distributions, the square of the measured D-XRD broadening, $B_m^2(hkl)$, is given by [21]:

$$B_m^2(hkl) = B_i^2(hkl) + B_c^2(hkl) + B_r^2(hkl) + B_t^2(hkl) + B_d^2(hkl) \qquad \text{(Eq.II.9)}$$

where $B_i^2(hkl)$ is the intrinsic width for the crystal being examined which is usually less than 0.0028° and can therefore be neglected [15]. $B_c^2(hkl)$ is the broadening due to the curvature of the crystal specimen but usually the substrate is largely thicker than the deposited layer so that the broadening due to the substrate curvature can be neglected too [21], $B_r^2(hkl)$ is the broadening caused by angular rotation at dislocations, $B_t^2(hkl)$ is the broadening related to the layer thickness and can be neglected if the layer is thicker than 1 µm, $B_d^2(hkl)$ is the broadening caused by the inhomogeneous strain surrounding dislocations [23]. Therefore simplifying Eq.II.9:

$$B_m^2(hkl) = B_r^2(hkl) + B_t^2(hkl) + B_d^2(hkl) \qquad \text{(Eq.II.10)}$$

The broadening due to the epilayer thickness, $B_t^2(hkl)$, can be obtained as following [24]:

$$B_t^2(hkl) = \left[\frac{4.\ln(2)}{\pi.h^2}\right].(\lambda^2/cos^2(\theta_B)) \qquad \text{(Eq.II.11)}$$

where h is the layer thickness.

Warren [24], Hordon and Averbach [26] have assumed that the square of the strain broadening ($B_d^2(hkl)$), due to dislocations, gives rise to a Gaussian distribution of local strain. Then $B_d^2(hkl)$ is given by:

$$B_d^2(hkl) = a.tan^2(\theta) \qquad \text{(Eq.II.12)}$$

Williamson and Hall have suggested a plot of the $B_d^2(hkl)$ from the D-XRD versus $\tan^2(\theta)$, where θ is the Bragg angle, called "Williamson–Hall plot". The use of different Ω-scan D-XRD symmetric reflections such as (002), (004), and (006) allows calculating the slope a. $B_r^2(hkl)$, caused by angular rotation at dislocations, will be the intercept of this equation:

$$B_m^2(hkl) = \; B_r^2(hkl) + \; a.tan^2(\theta) \qquad \text{(Eq.II.13)}$$

The dislocation density (D) may be determined from the rotational broadening as [14]:

$$D = \frac{B_r^2(hkl)}{4.36 \times b^2} \qquad \text{(Eq.II.14)}$$

and from the strain broadening as:

$$D = \frac{a}{0.09 \times b^2 \times \left| \ln(2 \times 10^{-7} \; cm \sqrt{D} \right|} \qquad \text{(Eq.II.15)}$$

The value of D determined from the rotational broadening must be close to that determined from the strain broadening.

The WHM described above attributes the peak broadening to TDs and ignored the MDs which are unavoidable in relaxed highly mismatched films. Kaganer et al. have observed a non-linear relationship applying the WHM for the InAs/GaAs and GaAs/Si heteroepitaxial systems [20]. Thus, a more comprehensive model of the effect of dislocations in highly mismatched epitaxial films on the diffraction peaks is needed.

Extended version of Williamson-Hall model

The extended version of Williamson-Hall model, proposed by Kaganer et al. [18-20], is based on a plot that brings the broadening of the diffraction peaks obtained in different reflections, different scans, and different diffractometers on a common straight line.

The epilayer geometry employed in this model is schematically presented in Figure II.12.

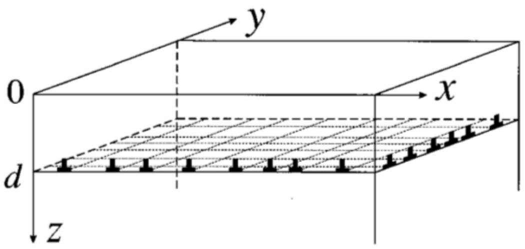

Figure II.12. Geometry of the MDs network in heteroepitaxial layer [27].

The MDs are supposed to lie on the interface between the epilayer and the substrate and they extend in two orthogonal directions at the interface (x and y-axis). The extended version of Williamson-Hall model is developed in Ref. 18. The integration in Fourier-transformed for the equation of the diffracted intensity represented as an integral over the film thickness (d) leads to the following equation [18]:

$$\Delta q = K \times \sqrt{\frac{\gamma\rho}{d}} \qquad \text{(Eq.II.16)}$$

where Δq is the FWHM of the peak from XRD scans, ρ is the density of MDs, γ is a correlation factor corresponding to the mean variation of the spacing between the dislocations, and the coefficient K depends on the scan, the reflection, and the diffractometry types. This latter coefficient is calculated from the equation of diffraction peak intensity by numerical integration. Table II.2 presents the coefficients K for 60° and 90° misfit dislocations for heteroepitaxial zinc blende structures for the reflections used in this work [20]. A plot of the peak FWHMs for different diffraction geometries as a function of K exhibits a linear trend with a slope equal to $\sqrt{\gamma\rho/d}$ and passing through the origin. Consequently, the determination of the MD density at the interface of a highly mismatched layer can be extracted. Actually, this model has been confirmed for GaAs/Si and GaSb/Si growth systems [20-28]. As the K coefficients are calculated for 60° and 90° misfit dislocations, two K-plots are obtained. In the following, we will discuss these two types of K-plot, following Rodriguez et al. [28].

60° dislocation K-plot

In this case**,** a combination of a perfectly regular 90° dislocation network and randomly distributed 60° dislocations at the interface is considered. Since the 60° dislocations are randomly distributed, therefore $\gamma = 1$ [19]. Then, according to Eq.II.16, the slope of the 60° dislocation K-plot provides the linear density of 60° dislocations.

90° dislocation K-plot

In this case, only an imperfect 90° dislocation network ($\gamma < 1$) is considered without 60° dislocations [19]. Then, using Eq.II.16 and assuming the dislocation density ρ for full relaxation, the slope of the 90° dislocation K-plot gives the correlation factor γ corresponding to the mean variation of the spacing between 90° dislocations.

Table II.2. Calculated K coefficients for 60° and 90° misfit dislocations in D-XRD and T-XRD measurements [20].

	K for 60° dislocations			**K for 90° dislocations**		
Diffractomery / scan types Reflections	T-XRD/Ω-scan	T-XRD/Ω-2θ scan	D-XRD/Ω scan	T-XRD/Ω-scan	T-XRD/Ω-2θ scan	D-XRD/Ω scan
(002)	10.751	3.425	11.022	6.507	4.4298	6.6668
(004)	21.499	6.85	19.617	13.0141	8.8597	12.5006
(006)	32.164	10.275	21.938	19.5202	13.2895	16.4088
(117)	37.856	11.76	15.038	23.4903	14.3099	14.8305
(444)	30.448	10.199	12.59	24.4286	11.4136	18.7897

References

1. A. Y. Cho, J. Cryst. Growth **201-202**, 1–7, 1999.

2. J. R. Arthur, 1968.

3. G. Gunther, Z. Naturforschg, 1958.

4. S. E. Kazzi, *Croissance épitaxiale d'hétérostructures antimoniées sur substrats fortement désadaptés en maille pour applications aux transistors à effet de champ*, IEMN Lille, 2012.

5. J. H. Neave, B. A. Joyce, P. J. Dobson, and N. Norton, Appl. Phys. A **31**, 1, 1–8, 1983.

6. J. J. Harris, B. A. Joyce, and P. J. Dobson, Surf. Sci.**103**, 1, L90–L96, 1981.

7. K. B. Ozanyan, P. J. Parbrook, M. Hopkinson, C. R. Whitehouse, Z. Sobiesierski, and D. I. Westwood, J. Appl. Phys. **82**, 1, 474, 1997.

8. M. Fahed, L. Desplanque, C. Coinon, D. Troadec, and X. Wallart, Nanotechnology **26**, 29, 295301, 2015.

9. I. Yoshiba, T. Iwai, T. Uehara, and Y. Horikoshi, J. Cryst. Growth **301–302**, 190-193, 2007.

10. L. Desplanque, M. Fahed, X. Han, V. K. Chinni, D. Troadec, M.-P. Chauvat, P. Ruterana, and X. Wallart, Nanotechnology **25**, 46, 465302, 2014.

11. S. Trudel, *Etude par double et triple diffraction des rayons X et modélisation, de la relaxation des contraintes dans des hétérostructures semiconductrices Gain As/GaAs et AllnAs/GaAs à rampe de composition graduelle linéaire*, L'Université des Sciences et Technologies de Lille, 1997.

12. J.-M. Chauveau, *Influence des conditions de croissance sur la qualité structurale et la morphologie de surface de rampes à composition graduelle InAlAs sur GaAs : application aux HEMTs métamorphiques*, Lille 1, 2001.

13. G. K. Williamson and W. H. Hall, Acta. Meta. **1**, 1953.

14. J.E. Ayers, J. Crys. Growth **135**, 71-77, 1994.

15. T. Nguyen Thanh, C. Robert, A. Létoublon, C. Cornet, T. Quinci, E. Giudicelli, S. Almosni, N. Boudet, A. Ponchet, J. Kuyyalil, M. Danila, O. Durand, N. Bertru, and A. Le Corre, Thin Solid Films **541**, 36–40, 2013.

16. W. Guo, A. Bondi, C. Cornet, A. Létoublon, O. Durand, T. Rohel, S. Boyer-Richard, N. Bertru, S. Loualiche, J. Even, and A. Le Corre, Appl. Surf. Sci. **258**, 7, 2808–2815, 2012.

17. C. Ferrari, L. Francesio, P. Franzosi, and S. Gennari, Appl. Phys. Lett. **69**, 27, 4233, 1996.

18. V. M. Kaganer, A. Shalimov, J. Bak-Misiuk, and K. H. Ploog, Appl. Phys. Lett. **89**, 021922, 2006.

19. V. M. Kaganer and K. K. Sabelfeld, Phys. Rev. B **80**, 184105, 2009.

20. V. M. Kaganer, A. Shalimov, J. Bak-Misiuk, and K. H. Ploog, Phys. Status Solidi A **204**, 8, 2561-2566, 2007.

21. M. J. Hordon and B. L. Averbach, Acta. Meta. **9**, 1961.

22. M. A. G. Halliwell, M. H. Lyons, and M. J. Hill, J. Cryst. Growth **68**, 2, 523-531, 1984.

23. P. Gay, P. B. Hirsch, and A. Kelly, Acta. Meta. **1**, 1953.

24. J. E. Ayers, Heteroepitaxy of Semiconductors: Theory, Growth, and Characterization, CRC Press 2007.

25. B.E. Warren, Theory presented in the course on x-ray and crystal physics, Massachusetts Institute of Technology, Cambridge (1957).

26. M.J. Hordon and B.L. Averbach, Acta Met. **9**, 237, 1961.

27. V. M. Kaganer, R. Kohler, M. Schmidbauer, and R. Opitz, Phys. Rev. B **55**, 3, 1997.

28. J. B. Rodriguez, K. Madiomanana, L. Cerutti, A. Castellano, E. Tournié, Journal Crys. Growth **439**, 33–39, 2016.

CHAPTER III: Homoepitaxial selective area growth of InP and InAs

In this chapter, we first discuss about the growth parameters to achieve a good selectivity. We then study the crystal shape inside elongated apertures. Two homoepitaxial systems are considered: (i) InAs on InAs(001) and (ii) InP on InP(001). In each case, we focus on the understanding of the main mechanisms driving the growth.

1. Parameters influencing the selectivity

In this section, we investigate the role of the growth conditions on the selectivity. In MBE it is difficult to achieve growth without polycrystalline deposition on the mask (see chapter I). Full selectivity requires diffusion of the group-III element species towards the mask aperture (large diffusion length on the mask or very dense patterns) and/or important re-evaporation rate of group-III element from the mask surface. In our experiments we will see that the growth rate (GR) in the aperture almost corresponds to the nominal one. This means that the re-evaporation of III-element from the mask surface is the main mechanism to ensure the selectivity. Moreover, in order to obtain the complete selectivity a high substrate temperature is required together with a very slow GR. For InAs and InP homoepitaxial SAG, the In GR is fixed at 0.2 monolayer/s.

1.1. Growth temperature

Regarding the effect of the GT on the selectivity, figure III.1(a and b) displays the SEM images for 50 nm of InAs homoepitaxially grown at 470°C and 500°C, respectively, and for an As/In flux ratio of 10. The growth selectivity is achieved at a GT of 500°C but not at all at 470°C.

In order to determine the mean height of the InAs nanostructures, AFM measurements have been performed. Figures III.1(c and d) show respectively an example of AFM height profile at the GTs of 470°C and 500°C. Same line profiles were done on all the stripes to get the average height of the nanostructures. The mean height of InAs nanostructures grown at 470°C is close to that grown at 500°C. This means that the good selectivity at high GT is due to the larger re-evaporation rate of In at 500°C than at 470°C and not to an enhanced diffusion from the mask to the apertures.

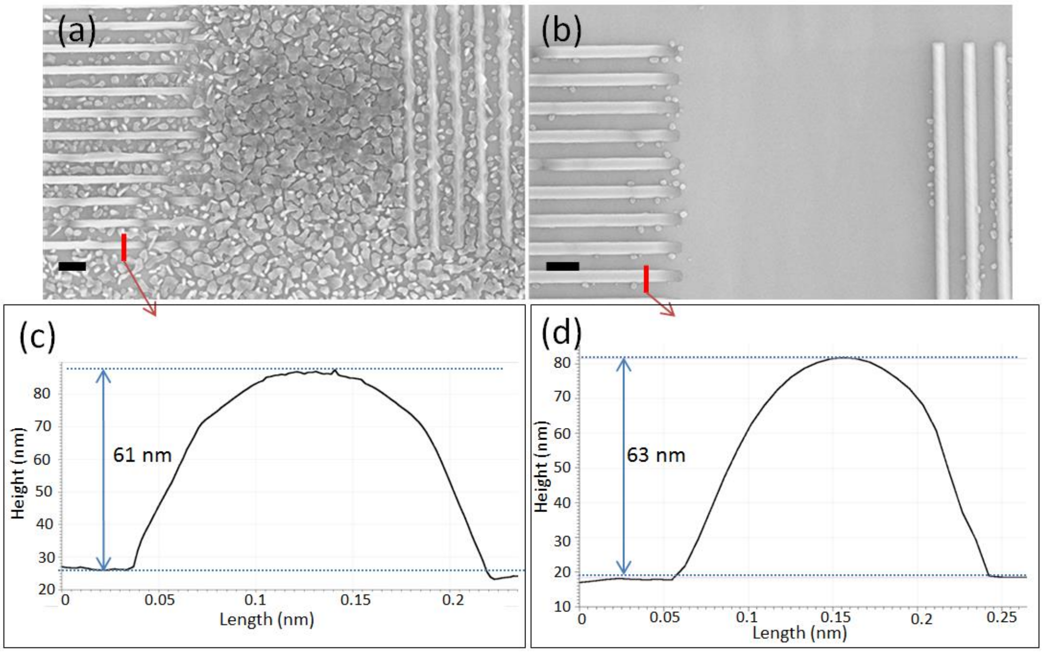

Figure III.1. SEM images recorded after 50 nm of InAs selectively grown on InAs(001) at 470°C (a) and 500°C (b). The scale bar represents 300 nm. Length and height nanostructure profiles along the corresponding red lines presented in the SEM images (c and d).

1.2. V/III flux ratio

Figures III.2(a and b) displays the SEM images after 100 nm of InAs homoepitaxialy grown at 500°C and for an As/In flux ratio of 10 and 30, respectively. No major effect of the As/In flux ratio is observed in this case. Therefore, the effect of the GT is clearly more prominent than that of the As/In flux ratio on the selectivity. In the following, InAs and InP are deposited at a fixed GT of 500 °C and a GR of 0.2 ML/s to ensure growth selectivity between the openings and the mask area.

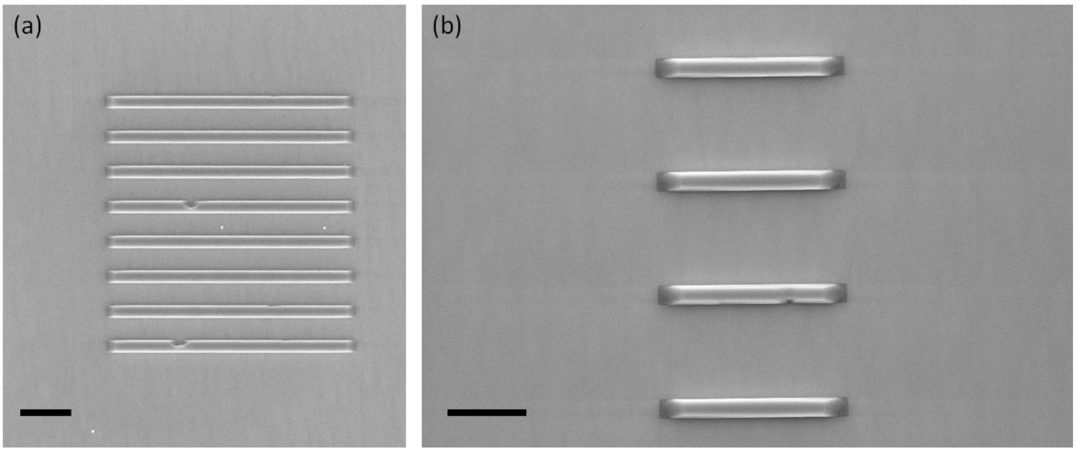

Figure III.2. SEM images recorded after 100 nm InAs selectively grown with an As/In flux ratio of 10 (a) and 30 (b). The scale bar represents 2 µm.

2. InAs selective growth

In this section, we study the faceting of InAs (001) nanocrystals formed in 200 nm and 500 nm wide stripe openings oriented along [110] and [1-10] directions. We especially stress the influence of the As/In flux ratio on the final faceting and show that along the [110] direction, the final nanostructure shape can be tailored thanks to the growth conditions, the stripe widths and directions. In order to interpret these experimental results, we start with the determination of the GR of each type of facet and notice that the shape does not evolve in an homothetic way due to the presence of the mask which impedes crystal growth in one direction. Therefore, we cannot interpret our data in terms of the equilibrium crystal shape (ECS) model (see chapter I). Accordingly, we use the facet surface energies previously calculated in order to discuss the observed shapes.

2.1. InAs nanostructure morphology

For each growth run, both a patterned InAs sample and a bare one without patterns are In soldered on the same sample holder, to allow RHEED observations. Before the growth, the InAs native oxide layer inside the SiO_2 apertures is removed by thermal annealing under arsenic flux at 520°C in the MBE chamber. Oxide removal is attested by the observation of a sharp (2x4) RHEED pattern on the bare substrate (see chapter 2). Table III.1 shows the different growth conditions for the samples considered in this section. InAs is deposited at a fixed GT of 500 °C and a GR of 0.2 ML/s.

Table III.1. Growth conditions for the InAs selectively grown samples.

Sample	Thickness (nm)	As/In flux ratio
A	50	10
B	100	10
C	150	10
D	200	10
E	100	30

2.1.1. As/In flux ratio influence on the nanostructure shapes

Figures III.3(a-d) show the FIB-STEM images of the nanostructures inside 200 nm wide stripe openings of samples B and E, i.e. varying the As/In flux ratio for a constant deposited thickness of 100 nm.

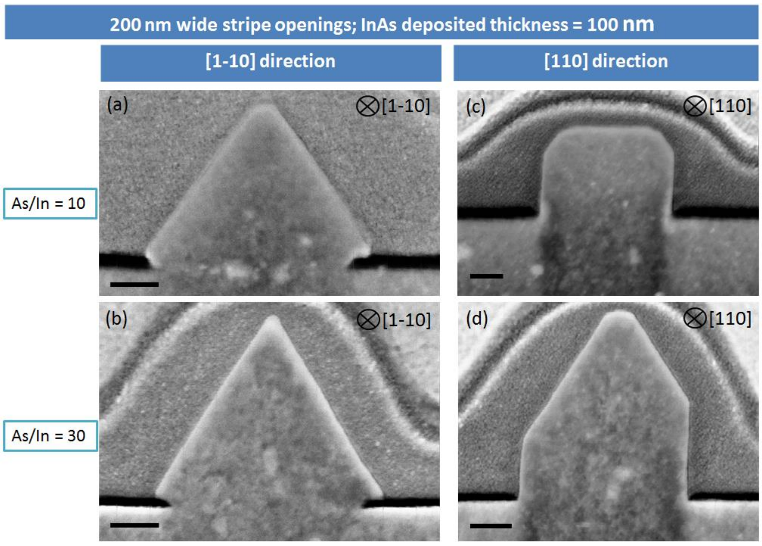

Figure III.3. FIB-STEM images recorded after 100 nm InAs growth in 200 nm wide apertures directed along [1-10] and [110] for As/In =10 (sample B, a and c), and As/In = 30 (sample E, b and d). The scale bar represents 50 nm.

Figures III.3(a and b), related to [1-10]-oriented stripes, exhibit shapes with (111)A facets which are not affected by the variation of the As/In flux ratio. For the same samples, figures III.3(c and d), related to [110]-oriented stripes, clearly demonstrate the increase of the (111)B facet length together with the shrinking of the (001) facet for the higher flux ratio value. In this way, the cross section evolves from a rectangular to a triangular shape, evidencing that changing the As/In flux ratio allows shape control in this direction.

Figures III.4(a-d) show the FIB-STEM images of the nanostructures inside 500 nm wide stripe openings of samples B and E. Figures III.4(a and b), related to [1-10]-oriented stripes, exhibits shapes with (111)A facets and (113)A ones which are not affected by the variation of the As/In flux ratio. For the same samples, figures III.4(c and d), related to [110]-oriented stripes, the cross section is weakly modified with the As/In flux ratio. For a low As/In flux ratio, the cross-section involves a rectangular shape with small (111)B facets at the top corners. For a high As/In flux ratio, the shape exhibits (552) and (001) edge and top facets, respectively, together with small (111)B facets at the top corners. Furthermore, from figures III.3 and 4 we can notice the limited InAs lateral growth over the SiO_2 mask.

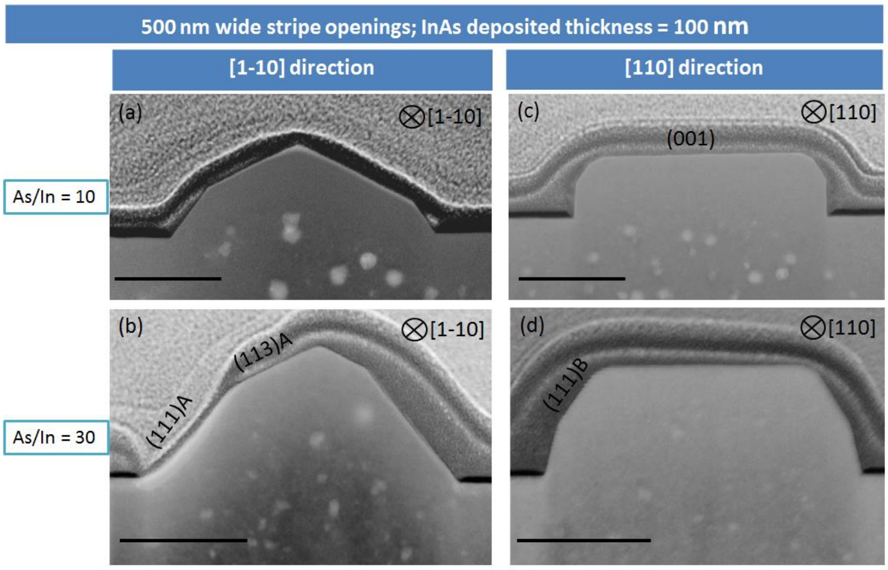

Figure III.4. FIB-STEM images recorded after 100 nm InAs growth in 500 nm wide apertures directed along [1-10] and [110] for As/In =10 (sample B, a and c), and As/In = 30 (sample E, b and d). The scale bar represents 200 nm.

2.1.2. Nanostructure shape evolution as a function of deposited thickness

Figure III.5 reveals the nanostructure evolution as a function of the deposited thickness for a stripe width of 200 nm and an As/In flux ratio of 10. For [1-10]-oriented stripes the shape begins forming (113)A facets (figure III.5a) which extend until the cross section involves only (111)A ones (figure III.5(b and c)). As the growth proceeds, the crystal starts overgrowing on the mask and an important density of twin defects is noticed (figure III.5d).

For the [110]-oriented stripes (figures III.5e), the (111)B, (001), and (110) facets first form until the cross section becomes a rectangle with small (111)B facets at the top corners (figure III.5f). With increasing InAs thickness, the (001) facet disappears and the shape exhibits (110) edge and (111)B facets on the top (figure III.5(g)). Further growth mainly occurs on the (111)B facets with an important density of defects (figure III.5((h)). The growth on (111)B surfaces are largely studied in the case of vertical nanowires. Actually, an important density of crystalline defects along the nanowire, mainly stacking faults (SFs) and twins, are noticed [1].

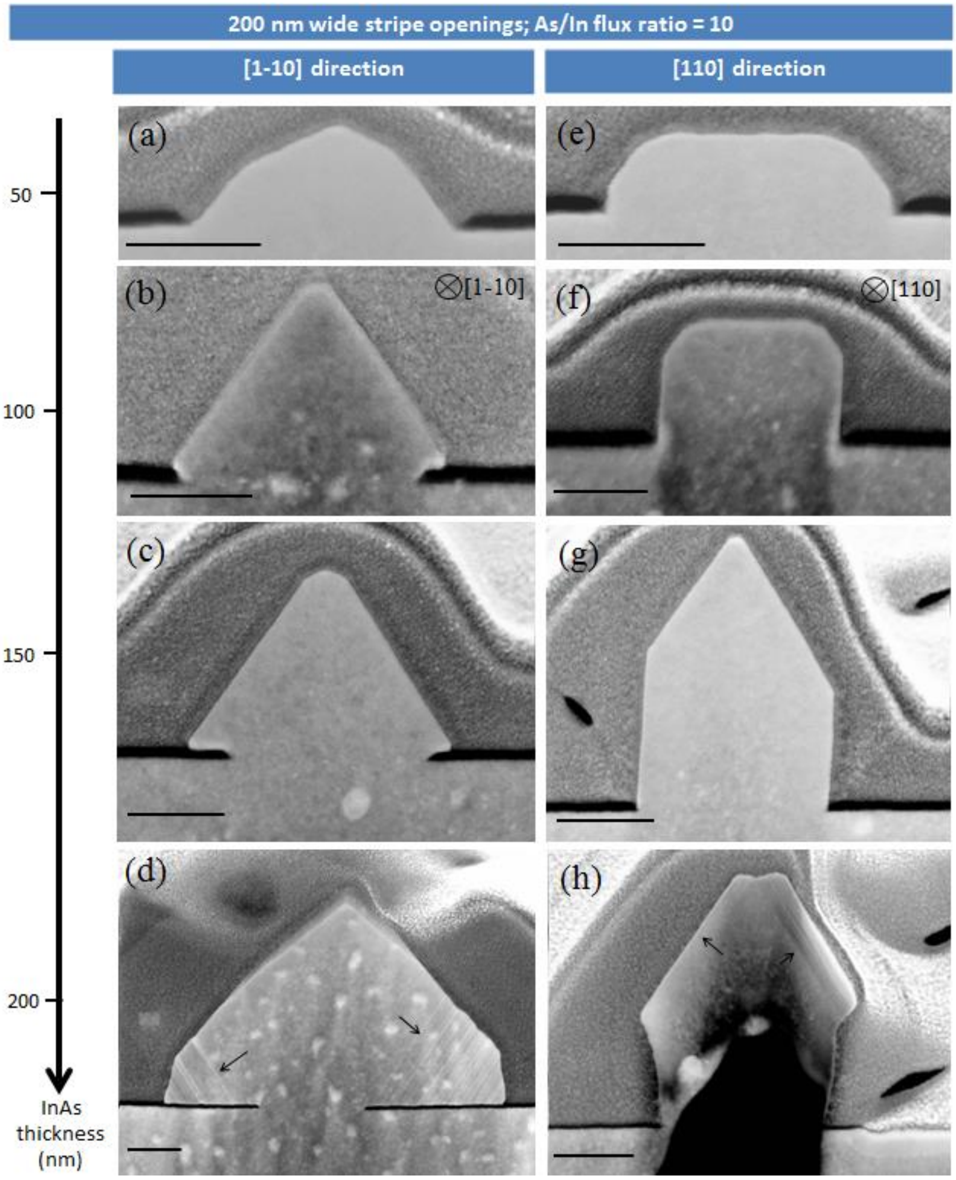

Figure III.5. FIB-STEM images recorded after the growth of 50 nm (sample A, a and e), 100 nm (sample B, b and f), 150 nm (sample C, c and g), and 200 nm (sample D, d and h) of InAs in 200 nm wide stripe openings directed along [1-10] and [110]. The scale bar represents 100 nm.

Figures III.6 reveal the nanostructure evolution as a function of the deposited thickness for the stripe widths of 500 nm. For [1-10]-oriented stripes the shape begins forming (113)A facets (figure III.6a) which extend until the cross section involves only (111)A ones (figure III.6d). For the [110]-oriented stripes (figures III.6e), the (111)B and (001) facets first form until the cross section becomes a rectangle with small (111)B facets at the top corners (figure III.6f). By increasing InAs thickness, the length of the (001) and (111)B facets decreases and increases, respectively (figure III.6h).

We notice that the InAs shape in both aperture openings does not evolve in an homothetic way, mainly due to the lateral growth limitation imposed by the mask. This in turn impedes the crystal to reach its free equilibrium shape.

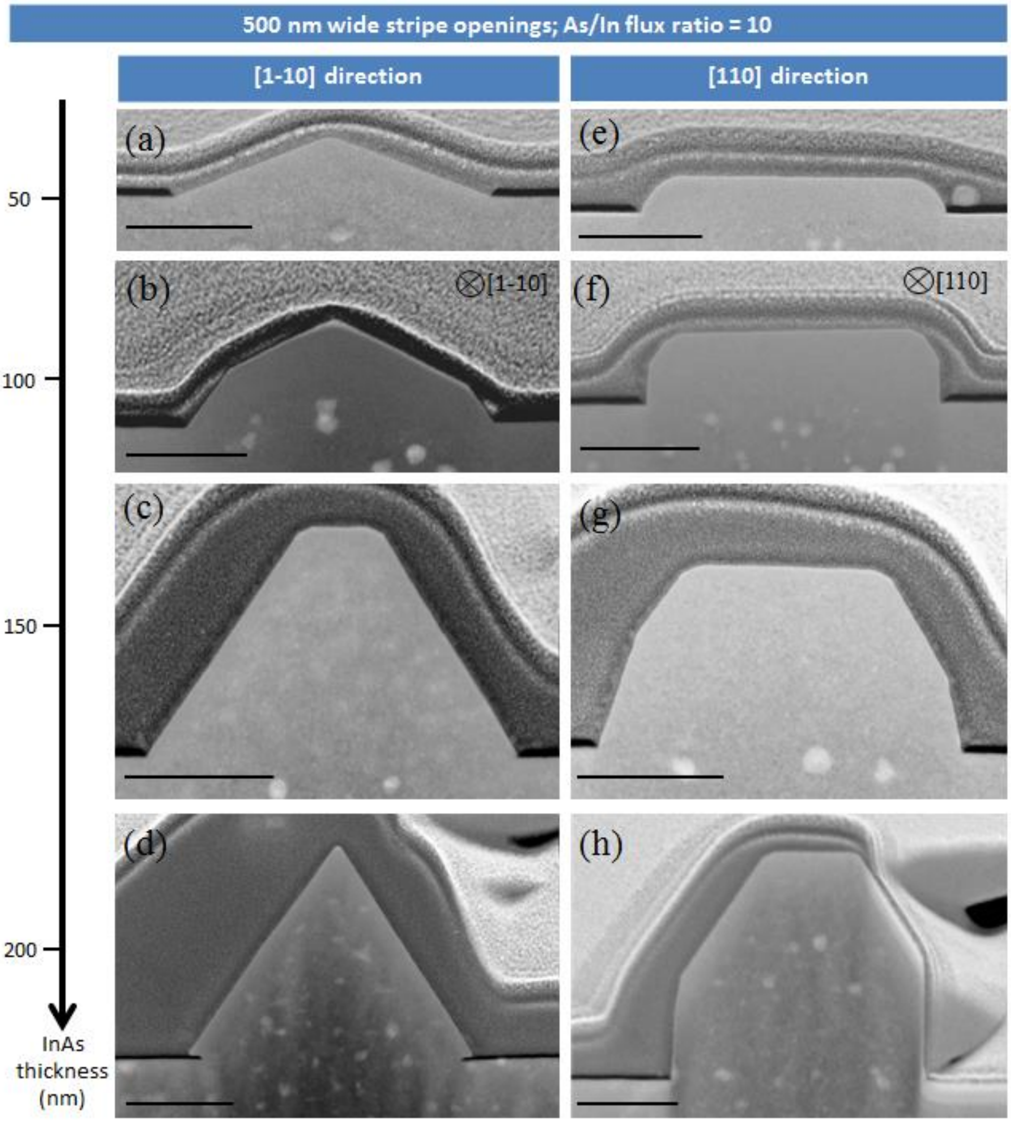

Figure III.6. FIB-STEM images recorded after the growth of 50 nm (sample A, a and e), 100 nm (sample B, b and f), 150 nm (sample C, c and g), and 200 nm (sample D, d and h) of InAs in 500 nm wide stripe openings directed along [1-10] and [110]. The scale bar represents 200 nm.

2.2. Facet growth rates

In the literature, for III-V SAG, the facet GRs have been only studied for GaAs [2]. In this case, several nm-thick AlAs lattice matched markers were embedded into the GaAs nanostructures to clearly observe the evolution of the facets during growth (figure III.7). For InAs, it is difficult to introduce AlSb or GaSb markers during the growth without affecting the InAs nanostructures. Indeed, strain is generated at the interfaces due to the commutation of both anions and cations and more, growth selectivity cannot be achieved easily for Al-based materials. For these reasons, we have grown nanostructures with different InAs thicknesses and determined the corresponding GR for each facet. It is worth noticing that when using marker layers, the GRs are determined within one experiment whereas in our case several growths were needed to determine the facet GRs.

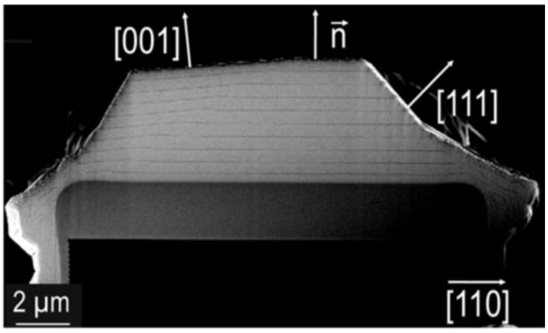

Figure III.7. SEM image of GaAs growth with AlAs markers layers [2].

Figure III.8(a) shows the image of a FIB-STEM lamella with dozen of InAs-nanostructures of sample B. They have almost the same shape with slight differences due to side effects such as the profile and thickness of the mask. For each sample, we then consider the mean nanostructure shape to get the facet GRs. For example, figure III.8b shows how we can determine the GR(001) for sample B.

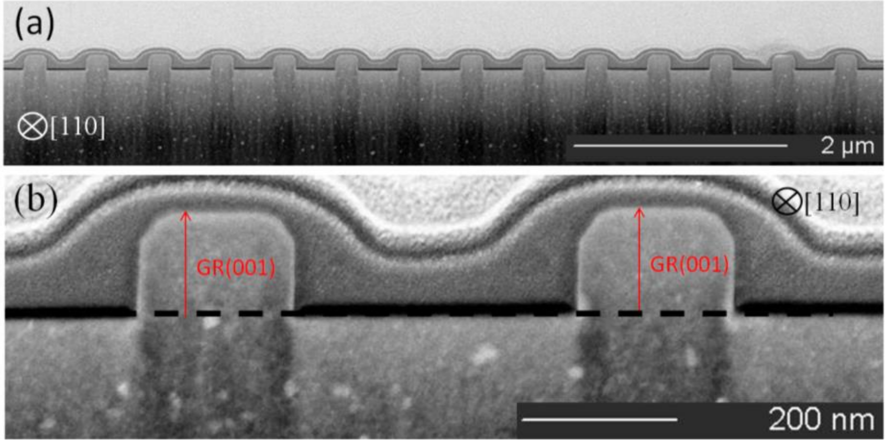

Figure III.8. FIB-STEM image recorded after 100 nm InAs growth in apertures directed along [110] and for As/In = 10 (sample B) (a). Example of GR(001) determination for sample B (b).

Table III.2 represents the facet GRs for the samples grown at low As/In flux ratio (samples A, B, C and D). i.e. varying the deposited thickness for a constant As/In flux ratio of 10. In this table, for the boxes that contain no value, the GR cannot be measured because the facets are not already formed. We notice that the obtained GRs for both stripe widths are close to each other. The important feature in table III.2 is that GR(001) increases whereas GR(111)B remains almost constant and no growth is observed along [110] with increasing deposited thickness. This is related to the fact that the InAs nanostructures do not grow on the oxide.

Table III.2. Experimentally measured facets GR of samples A, B, and C for the stripe opening of 200 and 500 nm.

GR (nm/s) Sample (thickness)	(001)		(111)B		(113)A
	Opening width (nm)				
	200	500	200	500	500
A (50 nm)	0.069	0.066	-	-	-
B (100 nm)	0.091	0.072	0.03	0.039	0.024
C (150 nm)	0.116	0.125	0.032	0.024	-
D (200 nm)	-	0.121	-	0.028	-

The variation of GR(001) values is due to a combination of an increasing amount of material collected by the 3D surface of the nanostructure and migration from the side facets. For this reason, we measure the cross-section area of InAs-nanostructures for samples A, B, C, and D inside the stripe of 200 and 500 nm width in order to compare it with the deposited one (nominal) (Table III.3)

Table III.3. Areas determined via FIB-STEM images for the obtained InAs-nanostructures inside the aperture directed along [110] of samples A, B, C, and D.

Sample	Nominal area (nm^2)	Cross-section area of InAs-nanostructures (nm^2)	Nominal area (nm^2)	Cross-section area of InAs-nanostructures (nm^2)
	Opening width (nm)			
	200		500	
A	10 000	10 150	25 000	24 706
B	20 000	27 800	50 000	58 853
C	30 000	52 960	75 000	105 172
D	40 000	85 731	100 000	175 209

For sample A, we notice a good agreement between the calculated area of the InAs nanostructures via the FIB-STEM images and that corresponding to the nominal deposited thickness. Conversely, for samples B, C, and D different values were found between the calculated area of the InAs nanostructures via FIB-STEM images and the nominal one.

Figure III.9 presents the variation of the GR(001) and the ratio of the InAs cross-section area over the nominal one versus the deposited thickness for the 200 and 500 nm wide stripes. We notice that for the two stripe openings considered, both parameters increase with thickness. This in turn implies that when the (110) facets appear, a migration from these facets to the top ones must occur to avoid the lateral overgrowth on the mask. This behavior leads to an increase of the (001) GR. In the next section, we will discuss this mechanism in the framework of the non-free equilibrium crystal shape using the facet surface energy [3].

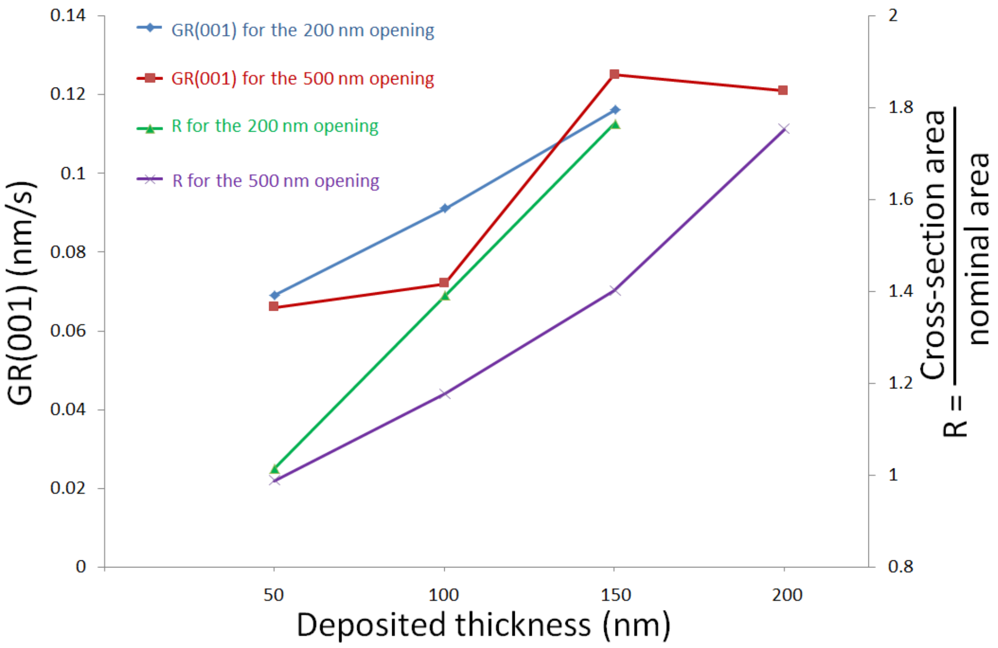

Figure III.9. Variation of GR(001) and the ratio of InAs cross-section area on the nominal one versus the deposited thickness for the stripe wide of 200 and 500 nm.

2.3. InAs facet surface energies

As we have presented in chapter 1, the ECS describes the shape evolution when the growth proceeds under equilibrium and when the crystal is free to grow in all directions. Moreover, crystal growth can be assumed to occur under equilibrium when the ratio between the facet lengths is conserved. This condition is clearly not fulfilled as can be noticed in figures III.5 and III.6. Therefore, we cannot apply the ECS model to describe this crystal shape evolution. Nevertheless, insight in the faceting of the obtained nanostructures can be gained considering the different facet surface energies of InAs, which have been previously calculated within the density-functional theory (DFT) [3].

The (001), (110) and (111)A and B surface energies for different reconstructions have been calculated as a function of the parameter $\Delta\mu_{As}=\mu_{As}-\mu_{As(Bulk)}$, where μ_{As} is the arsenic chemical potential at the surface and $\mu_{As(Bulk)}$ is the chemical potential of arsenic in solid arsenic. The lowest surface energies for (110), (001), (111)A and (111)B surface orientations for InAs are presented in figure III.10.

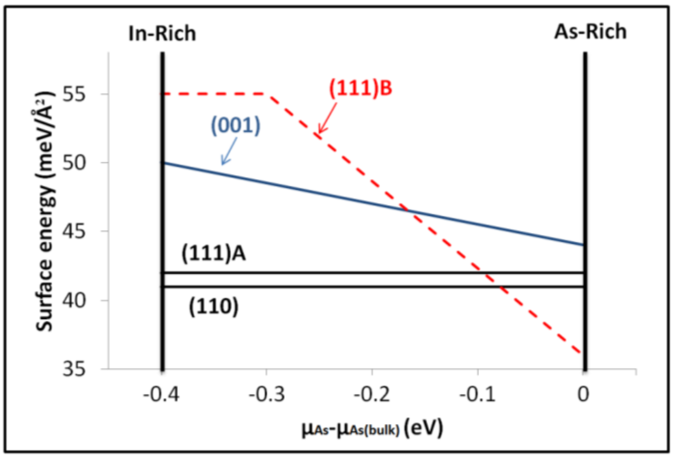

Figure III.10. Variations of the surface energy of the low-index InAs facets versus the arsenic chemical potential. For each orientation, only the minimum value is represented (after [3]).

The left and right vertical black lines determine the limits for In- and As-rich environments, respectively. The important feature in figures III.10 is that the (111)B surface energy strongly varies from In-rich to As-rich environment, contrarily to the other orientations, for which the surface energy remains almost constant. Qualitatively, from these calculations and if the InAs crystal shape evolves in a more or less homothetic way, we expect rather small (111)B facets for a large negative value of $\Delta\mu_{As}$. Actually if the chemical potential is higher than -0.1 eV, we obtain $\sigma_{(111)B} \leq \sigma_{(111)A}$. This should result in the same crystal cross-section for stripes oriented along the [110] and [1-10] directions, which is not the case (figure III.5). Therefore, the chemical potential is lower than -0.1 eV.

The GR calculations presented in the above section show an In-migration from (110) facets to (111)B and (001) ones, which results in an In-enrichment on these facets. Figure III.11 schematically presents this In-migration. This in turn implies that the chemical potential of the As species on the (111)B and (001) facets decreases. When the growth proceeds the (110) facets becomes larger inducing an enhanced In-migration from (110) facets to (111)B and (001) ones and hence to a corresponding decrease of the chemical potential of the As species. Therefore the chemical potential is varying during the growth, which makes difficult the prediction of the InAs shape evolution with the growth conditions such as the deposited thickness and the As/In flux ratio. This explains why, although the InAs nanostructure growth is not limited by kinetic effects, the overall shape is not preserved during growth.

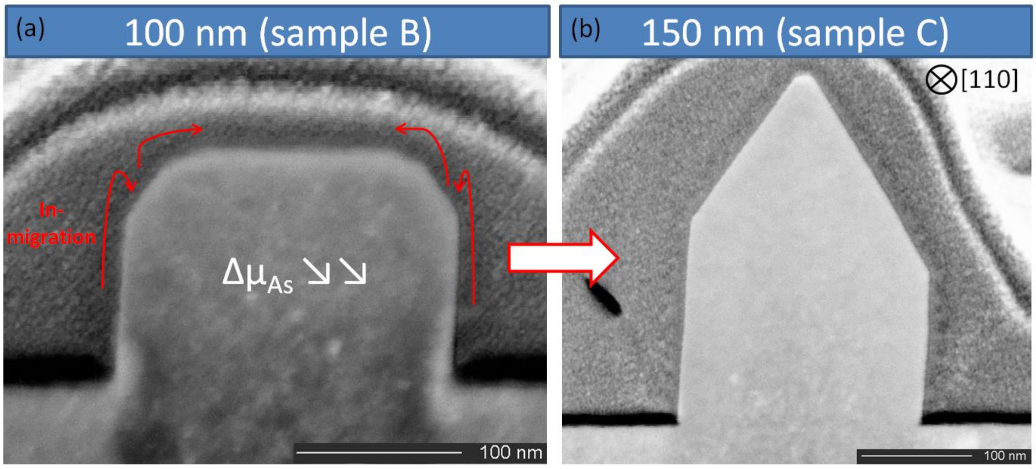

Figure III.11. FIB-STEM image recorded after 100 and 150 nm InAs growth in apertures directed along [110] showing the In-migration from (110) facets to (111)B and (001) ones.

2.4. Conclusion

We have shown that the faceting of InAs nanostructures selectively grown inside 200 and 500 nm wide stripes by MBE on an InAs substrate can be tailored playing with the As/In flux ratio, the deposited thickness, as well as the opening width and direction. We discuss the faceting of InAs in the framework of facet kinetics and surface energies in order to understand the evolution of InAs nanostructures inside opening. For [1-10]-oriented stripes, the crystal shape is characterized by the formation of (113)A and (111)A facets, with no significant difference when varying the As/In flux ratio. However, for [110]-oriented stripes, according to the variations of the (111)B facet surface energy with the As/In flux ratio, (111)B facets are less or more extended for low or high As/In flux ratio respectively. Actually, for a low As/In flux ratio value, in the first stage of growth, the crystal tends to develop a rectangular shape with small (111)B facets on the top edges. When the deposited thickness becomes important, a migration of In from the (110) facets to the (001) ones occurs. This behavior is a consequence of the high value of the interface energy between InAs and the oxide.

In order to compare the shape evolution for both aperture widths when the growth proceeds, we use an effective aspect ratio (EAR). It is defined as the ratio of the experimental thickness (T_{exp}) over the opening width (W), where T_{exp} is obtained as the ratio of the InAs nanostructure cross-section surface over W. Figures III.12 and 13 schematically present the shape evolution with increasing EAR for the stripes oriented along [110] and [1-10] direction respectively. The use of this EAR clearly allows us ordering the growth sequence for different deposited thickness and opening widths.

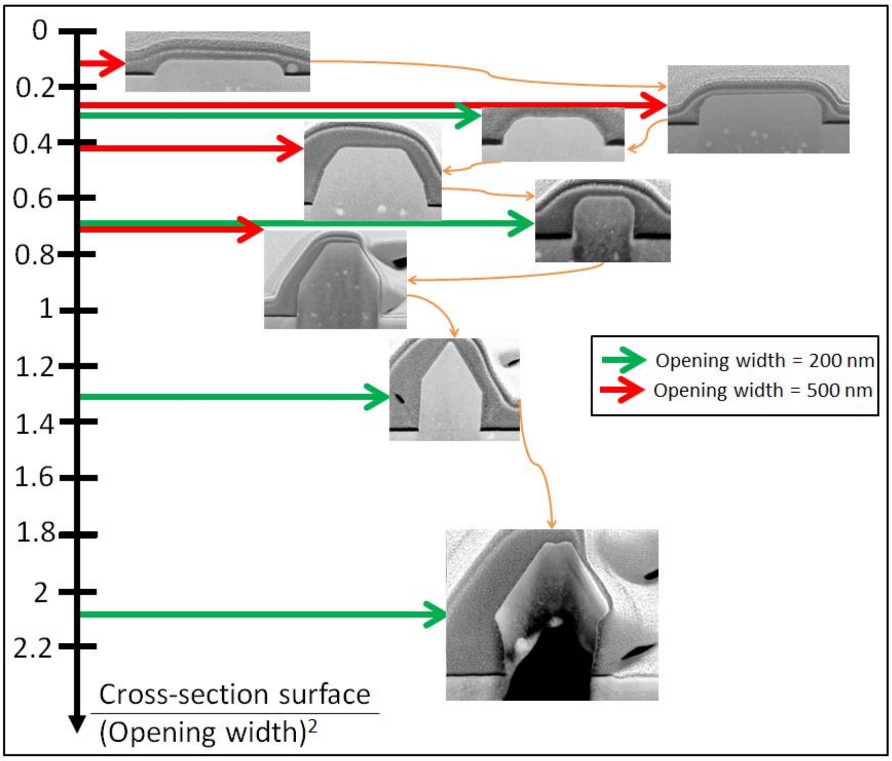

Figure III.12. Schematic of the shape evolution inside the stripe oriented along [110] when the growth proceeds.

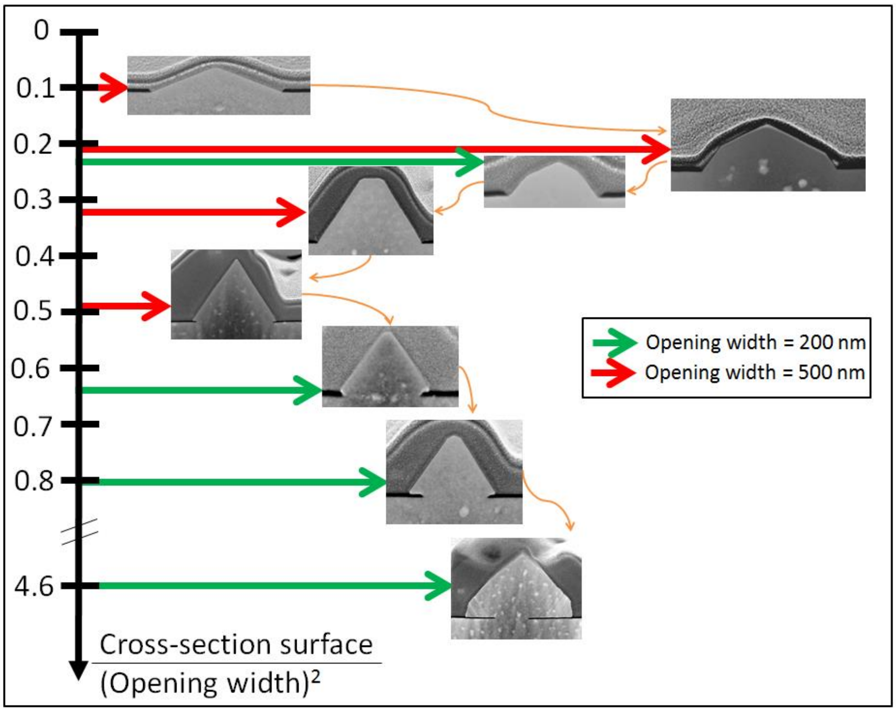

Figure III.13. Schematic of the shape evolution inside the stripe oriented along [1-10] when the growth proceeds.

3. InP selective growth

We investigate the faceting of InP nanocrystals formed in 200 and 100 nm wide stripe openings oriented along the [110] and [1-10] directions. We especially stress the influence of the P/In flux ratio on the final faceting and show that along the [110] direction, the final nanostructure shape can be tailored thanks to the growth conditions. In order to interpret these experimental results, we start with the determination of the GR of each facet type where we distinguish two different regimes: before and after lateral overgrowth on the oxide mask. We noticed that after lateral overgrowth the crystal shape evolves in a more or less homothetic way. For this reason we choose this latter regime, in order to discuss the observed shapes according to the ECS model. We then discuss the evolution of the nanostructure shape with the InP-deposited thickness. Finally, using the minimization of total surface energy approach we tentatively determine a range of values for the interface energy between InP and the mask at low and high values of the P/In flux ratio.

3.1. InP nanostructure morphology

For each growth run, both a patterned InP sample and a bare one are In soldered on the same sample holder, to allow RHEED observations. Before the growth, the InP native oxide layer inside the SiO_2 apertures is removed by thermal annealing under phosphorus flux at 525-530°C in the MBE chamber. Oxide removal is attested by the observation of a sharp (2x4) RHEED pattern on the bare substrate (see chapter 2). Table III.4 shows the different growth conditions for the samples considered in this section [4]. InP is deposited at a fixed GT of 500 °C and a GR of 0.2 ML/s to ensure growth selectivity between the InP openings and the mask area (see section 1). In the following, the ratio between In and P_2 fluxes is referred as P/In without any longer reference to P_2. The pattern consists in 200 and 100 nm wide and 4-micron long stripe openings oriented either along the [110] or the [1-10] direction.

Table III.4. Growth conditions for InP selective growth.

Sample	Thickness (nm)	P/In flux ratio
A	50	5
B	100	5
C	200	5
D	200	20
E	200	40
F	200	70

3.1.1. P/In flux ratio influence on the nanostructure shapes

a) 200 nm wide stripe openings

Figures III.14(a-d) show the SEM images of the nanostructures inside 200 nm wide stripe openings oriented along [1-10] for samples C, D, E, and F respectively, i.e. varying the P/In flux ratio for a constant deposited thickness of 200 nm. The dominant facets formed during growth are (111)A. No major shape difference can be detected, except the apparition of (111)B facets on samples D, E, and F. The observed structure asymmetry is ascribed to side effects such as the profile and thickness of the mask [5].

For the same samples, figures III.14(e-h) present the images recorded for stripes along [110]. In figure III.14(e), the cross section exhibits a rectangular shape with small (111)B facets at the top corners, whereas the cross sections in figures III.14(f-h) reveal larger (111)B facets than in figure III.14(e). Different shapes can be noticed in figure III.14 in both directions, but since for each direction and values of the P/In ratio higher than 20, no major differences are detected, only samples C (P/In=5) and F (P/In=70) will be further considered to discuss the influence of the P/In ratio on the observed shapes. Figure III.15 presents the FIB-STEM images for these two samples.

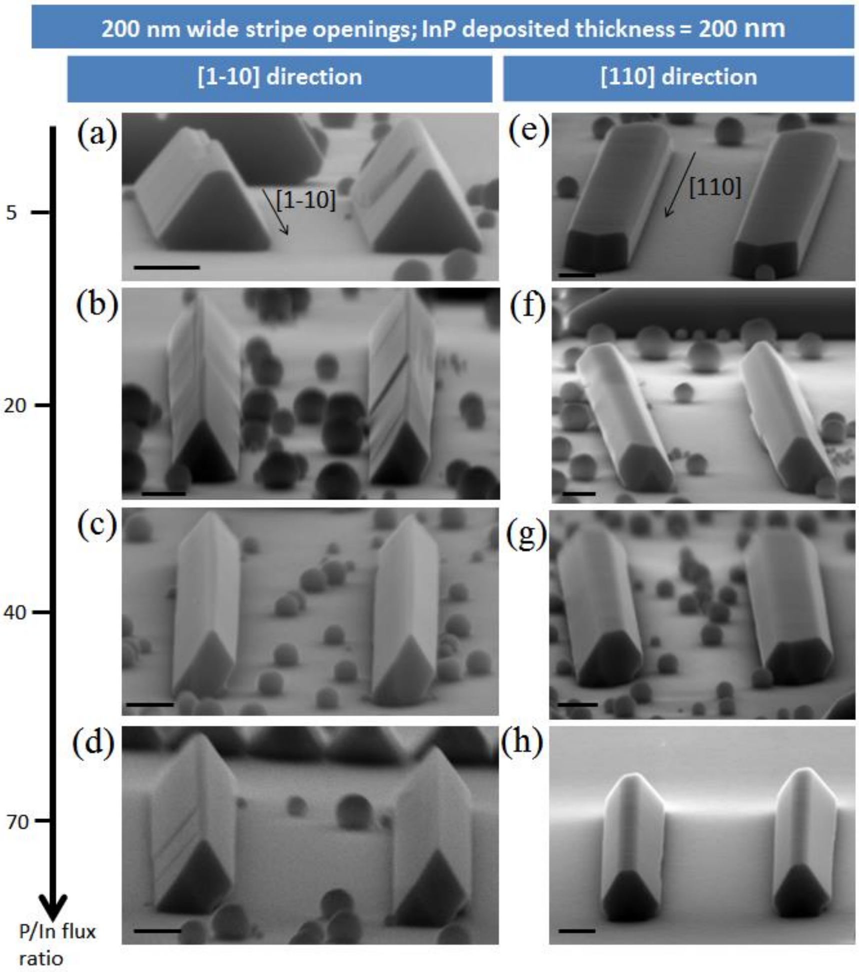

Figure III.14. SEM images recorded after 200 nm InP growth in apertures directed along [1-10] and [110] varying the P/In flux ratio. P/In = 5 (sample C, a and e), P/In = 20 (sample D, b and f), P/In = 40 (sample E, c and g), and P/In = 70 (sample F, d and h). The scale bar represents 200 nm.

Figures III.15(a and b), related to [1-10]-oriented stripes, confirm the observations in figures III.15(a and d), i.e. the major facets are the (111)A ones with only slight shape changes with the P/In flux ratio. On the contrary, for [110]-oriented apertures, the cross section is strongly modified with the P/In flux ratio. Figures III.15(c and d) clearly demonstrate the increase of the (111)B facet length together with the shrinking of the (001) facet for the higher value of this ratio. In this way, the cross section evolves from a rectangular to a triangular shape, evidencing that changing the P/In flux ratio allows shape control in this direction.

Furthermore, figure III.15 also reveals the lateral growth over the SiO_2 mask. This overgrowth is very limited for the high P/In flux ratio (sample F, figures III.15(b and d)), whereas for the low P/In flux ratio (sample C, figures III.15(a and c)) it is more prominent, resulting in a total width of 350 and 380 nm respectively for [1-10] and [110] directions respectively, notably greater than the original 200 nm stripe opening.

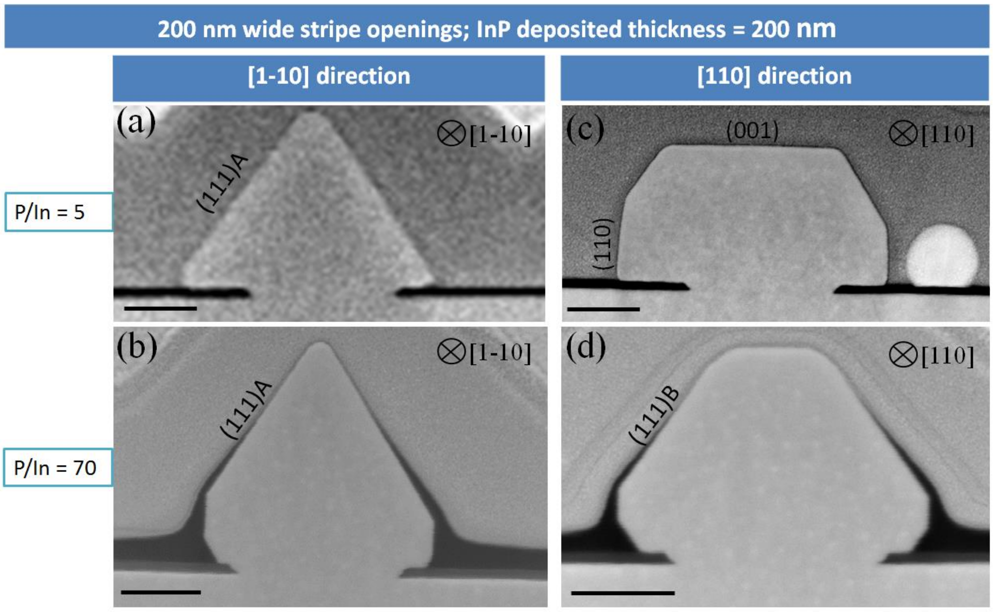

Figure III.15. FIB-STEM images recorded after 200 nm InP growth in apertures directed along [1-10] and [110] for P/In =5 (sample C, a and c), and P/In = 70 (sample F, b and d). The scale bar represents 100 nm.

b) 100 nm wide stripe openings

Figures III.16(a and d) show the SEM images of nanostructures grown inside 100 nm wide stripe openings oriented along both directions for samples C and F respectively, i.e. varying the P/In flux ratio for a constant deposited thickness of 200 nm.

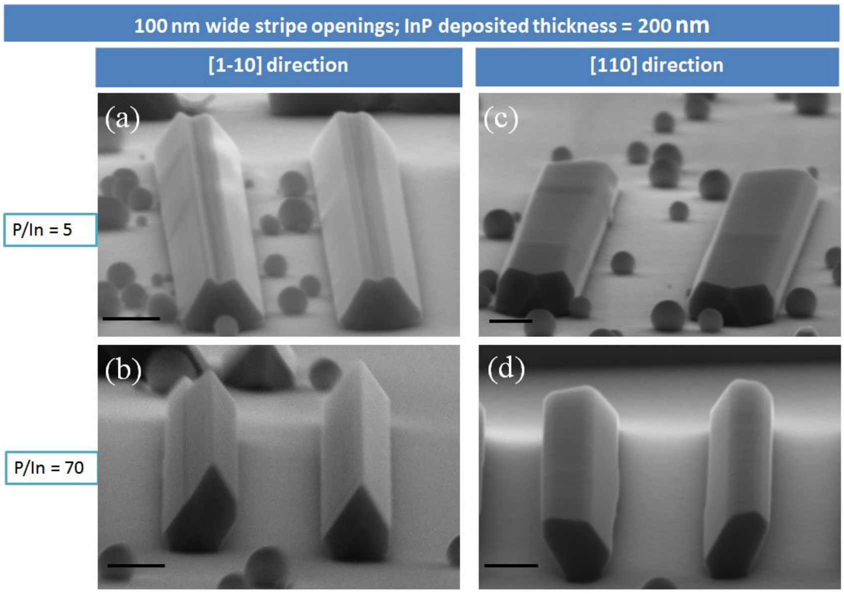

Figure III.16. SEM images recorded after 200 nm InP growth in apertures directed along [1-10] and [110] varying the P/In flux ratio. P/In = 5 (sample C, a and c) and P/In = 70 (sample F, b and d). The scale bar represents 200 nm.

For stripes long [1-10], the dominant facets are the (111)A ones whereas along [110 the cross section exhibits a rectangular shape with small (111)B facets at the top corners at low P/In value and larger (111)B facets for the high P/In one.

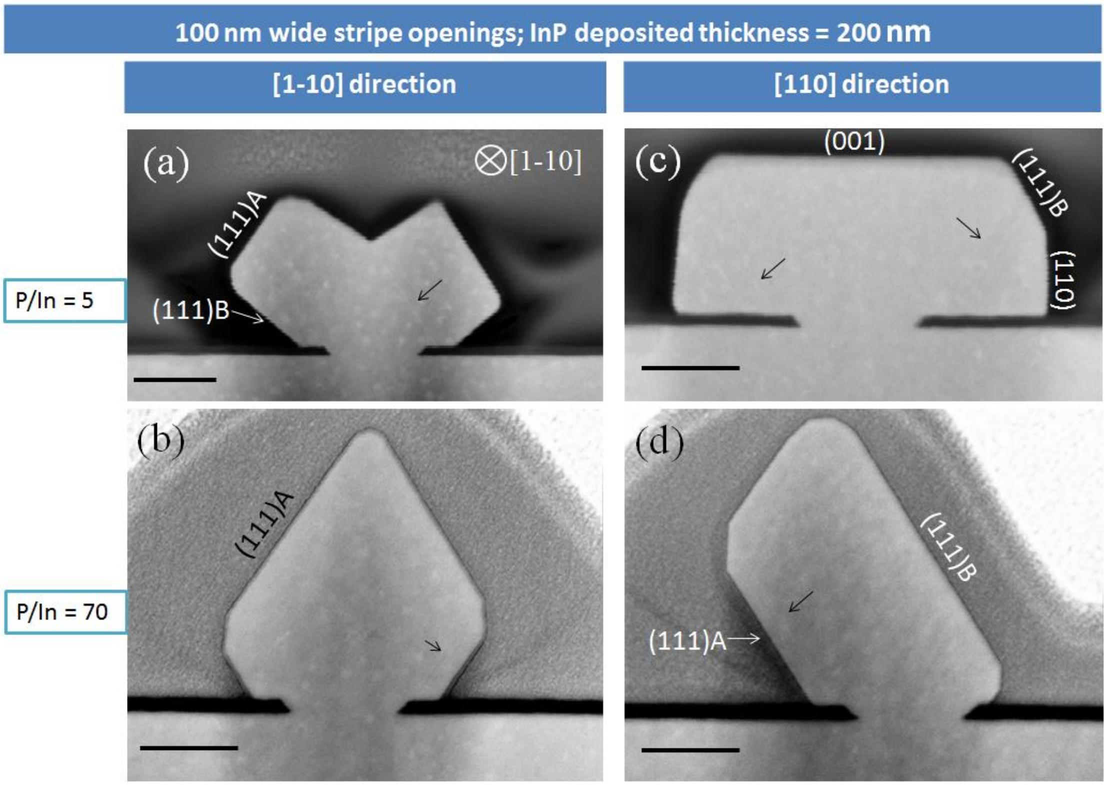

Figure III.17. FIB-STEM images recorded after 200 nm InP growth in apertures directed along [1-10] and [110] for P/In =5 (sample C, a and c), and P/In = 70 (sample F, b and d). The scale bar represents 100 nm.

Figure III.17 presents the FIB-STEM images for these two samples. The observations in figures III.17(a-d) are consistent with the ones shown in figures III.16(a-d). We first notice that the InP nanocrystals present a lot of twin defects (marked by black arrows) which make difficult the interpretation of their shape. Once again, from figures III.17(c and d) which are related to [110]-oriented stripes, the lateral growth over the SiO_2 mask is very limited for the high P/In flux ratio (sample F, figures III.17(d)), whereas for the low P/In flux ratio (sample C, figures III.17(c)) it is more prominent.

3.1.2. Nanostructure shape evolution as a function of deposited thickness

Figures III.18 and 19 reveal the nanostructure evolution as a function of the deposited thickness for both stripe widths (100 and 200 nm) and directions and for P/In = 5. For 200 nm wide and [1-10]-oriented stripes the shape begins forming (113)A and (114)A top facets and (111)A edge facets (figure III.18a) which extend until the cross section involves only (111)A ones (figure III.18c). For the [110]-oriented stripes (figures III.18(d-f)), (111)B and (001) facets first form and, as the growth proceeds, (110) facets appear until the cross section becomes a rectangle with small (111)B facets at the top corners (figure III.18f).

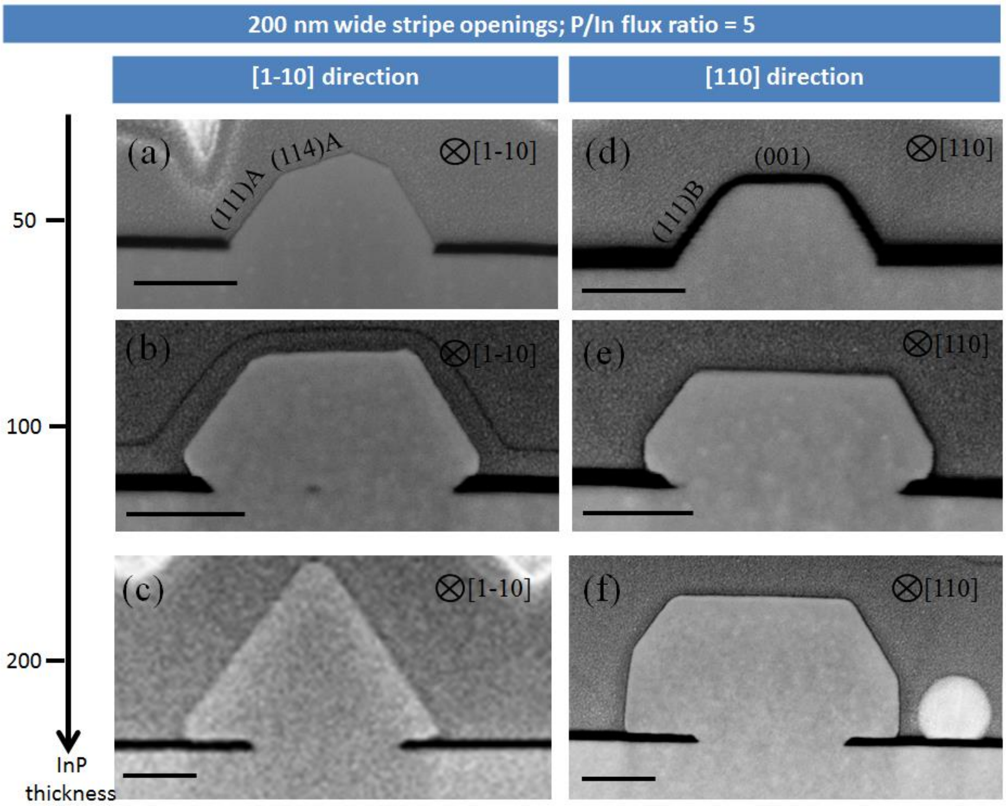

Figure III.18. FIB-STEM images recorded after the growth of 50 nm (sample A, a and d), 100 nm (sample B, b and e), and 200 nm (sample C, c and f) of InP in 200 nm wide stripe openings directed along [1-10] and [110]. The scale bar represents 100 nm.

For 100 nm wide apertures and [1-10]-oriented stripes, the shape starts forming (111)A edge facets (figure III.19a) and as the growth proceeds, InP grows on these facets (figure III.19c). For the [110]-oriented stripes (figures III.19(d-f)), (110), (111)B and (001) facets are firstly formed until the cross section becomes a rectangle with small (111)B facets at the top corners (figure III.19f).

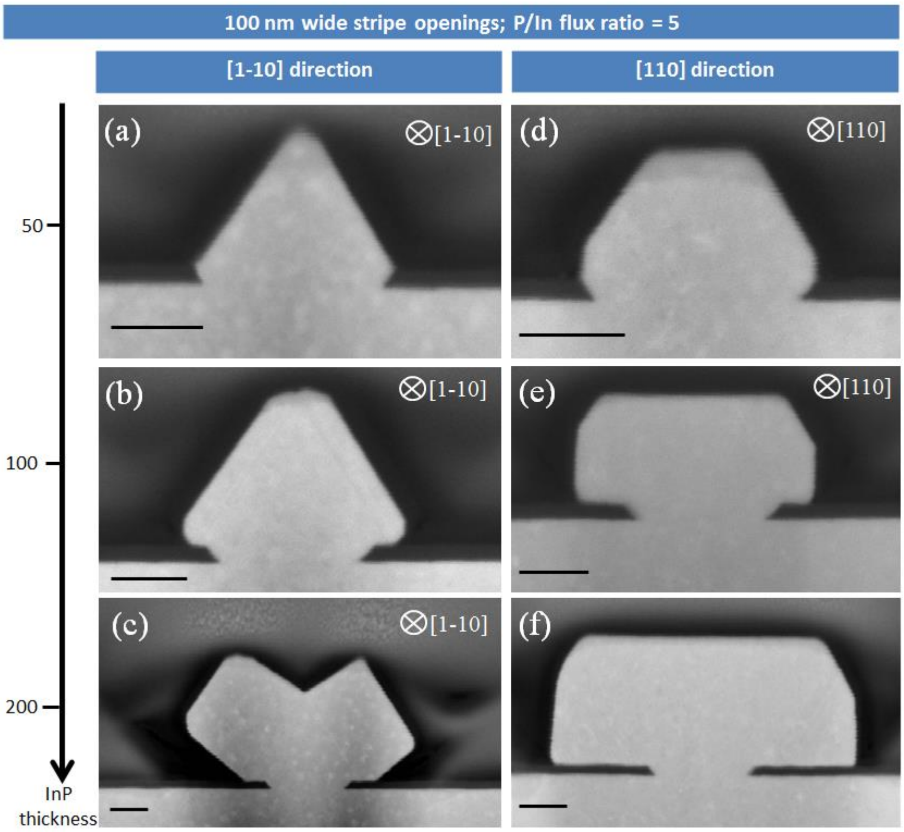

Figure III.19. FIB-STEM images recorded after the growth of 50 nm (sample A, a and d), 100 nm (sample B, b and e), and 200 nm (sample C, c and d) of InP in 100 nm wide stripe openings directed along [1-10] and [110]. The scale bar represents 50 nm.

3.2. Facet growth rates

As for InAs, there is no III-V material lattice matched to InP that can be easily grown by selective MBE as a marker without affecting the InP nanostructures. That’s why we have grown nanostructures for three different InP thicknesses and tried to determine the corresponding GR for each facet. Table III.5 represents the facet GRs for the samples grown at low P/In flux ratio (samples A, B, and C). i.e. varying the deposited thickness for a constant P/In flux ratio of 5. Three important features in table III.5 are discussed in the following. First the values of facet GRs determined from the two stripe widths (100 and 200 nm) are close to each other. This implies that whatever the stripe width the shape evolves in a similar way. Second, we notice that the GR(001) values determined for sample A are higher than those measured in samples B and C, which are rather similar. From figures III.18 and III.19, we can notice that sample B corresponds to the development of clear overgrowth on the mask. This leads us identifying two growth regimes: before and after lateral overgrowth on the mask. Finally, we remark that the values of GR(111)B are higher than the other ones, which explains the shrinking of the (111)B facets when growth proceeds. As we present in chapter 1, in order to use the ECS model, the crystal shape must evolve in a homothetic way. Since the facet GRs keep constant once lateral overgrowth is initiated, we only consider this case in the following to interpret the nanostructure shape in the ECS framework.

Table III.5. Experimentally measured facet GRs of samples A, B, and C for stripe openings of 100 and 200 nm.

GR (nm/s) Sample (thickness)	(001)		(111)B		(111)A		(110)	
	Stripes openings (nm)							
	200	**100**	200	**100**	200	**100**	200	**100**
A (50)	0.1	**0.092**	-	**-**	-	**-**	-	**-**
B (100)	0.023	**0.025**	0.048	**0.054**	0.041	**0.031**	-	**0.035**
C (200)	0.035	**0.03**	0.054	**0.052**	0.027	**-**	0.035	**0.04**

3.3. Equilibrium Crystal Shape (ECS) model

3.3.1. InP facet surface energies

The ECS model relies on the different facet surface energies which have been previously calculated within the DFT [6]. These surface energies will help us discussing the faceting of the obtained nanostructures. The (001), (110) and (111)A and B surface energies for different reconstructions have been calculated as a function of the parameter $\Delta\mu_P=\mu_P-\mu_{P(Bulk)}$, where μ_P is the phosphorus chemical potential at the surface and $\mu_{P(Bulk)}$ is the chemical potential of phosphorus in solid phosphorus. The lowest surface energies for (110), (001), (111)A and (111)B surface orientations for InP are presented in figure III.20. The left and right vertical black lines determine the limits for In- and P-rich environments, respectively. The important feature in figure III.20 is that the (111)B surface energy strongly varies from In-rich to P-rich environment, contrary to the other orientations, for which the surface energy remains almost constant. Qualitatively, from these calculations, we expect rather small (111)B facets for a large negative value of $\Delta\mu_P$.

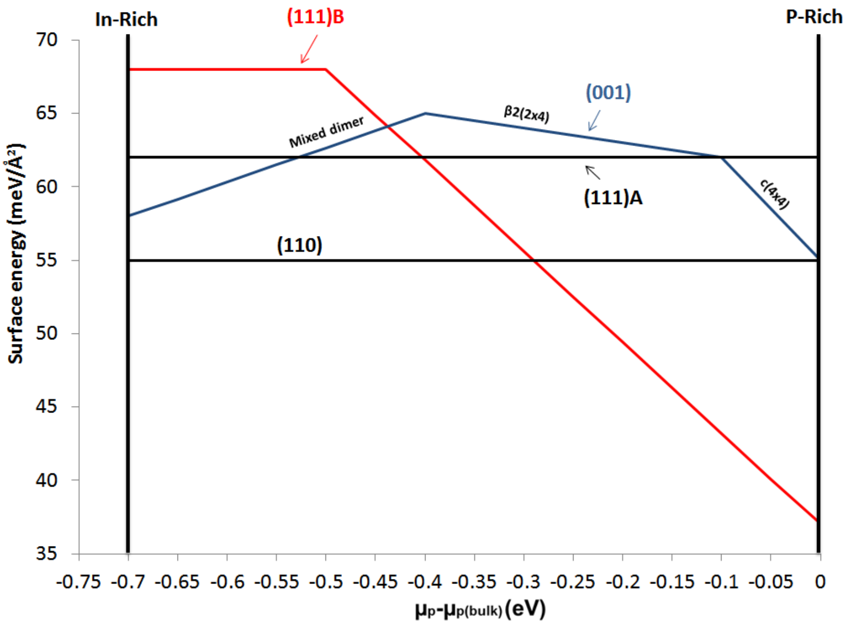

Figure III.20. Variations of the surface energy of the low-index InP facets versus the phosphorus chemical potential. For each orientation, only the minimum value is represented (after [6]).

3.3.2. Evaluation of the chemical potential from the nanostructure crystal shape

In order to discuss the faceting of InP described above in the framework of the ECS model [7-8], the knowledge of the chemical potential ($\Delta\mu_P$) in our growth conditions [3-9] is required. A first estimate of the $\Delta\mu_P$ range can be obtained by the observation of the RHEED pattern during growth. Indeed, on (001) surfaces, whatever the P/In flux ratio, we always observe a (2x4) diagram, which according to figure III.20, can be ascribed either to the β2(2x4) or to the mixed dimer reconstruction of the (001) surface but not to the c(4x4) one, which would result in a (2x2) diagram. This implies that, in our growth conditions, $\Delta\mu_P$ remains below -0.1 eV (and above -0.67 eV).

To get a more precise value of the $\Delta\mu_P$ parameter, we consider first the stripes directed along [110], since the (111)B facet surface energy is very sensitive to the chemical potential unlike the (111)A one (figure III.20). To that end, we collect all InP nanocrystal shapes exhibiting more than two different types of facets (Figure III.21(a and b)).

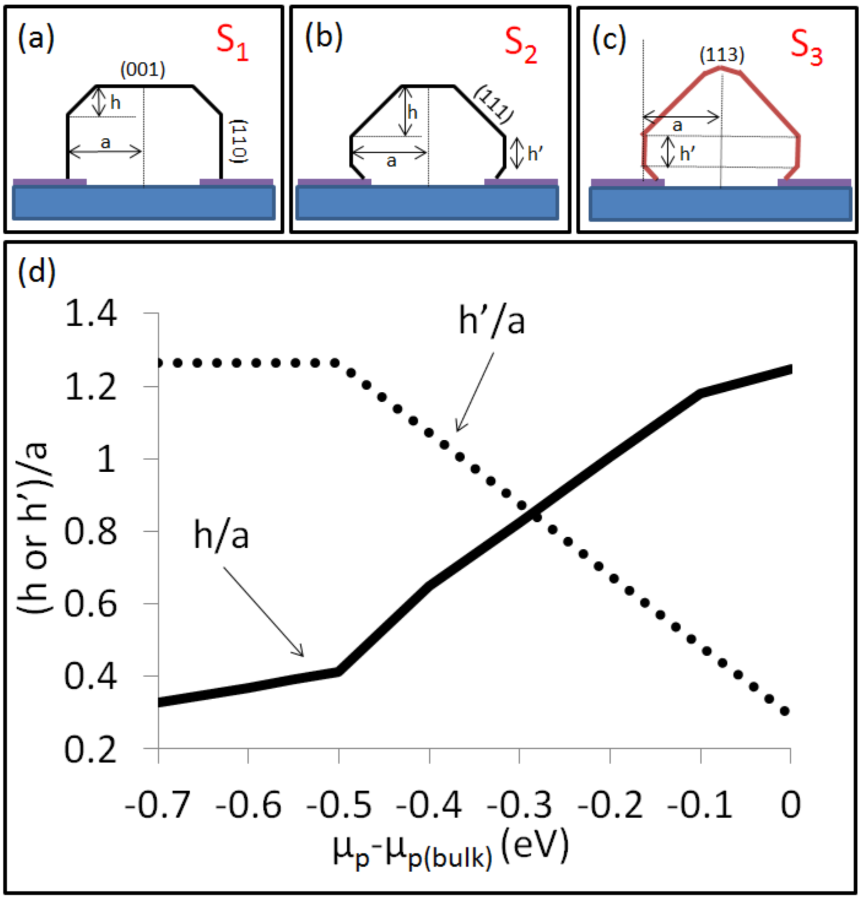

Figure III.21. The schematic of the main InP shapes having more than two different types of facets (a-c). Plot of $\Delta\mu_P = \mu_P - \mu_{P(bulk)}$ *versus h/a (solid line follows the relation given by Eq.III.3.) and h'/a (dashed line follows the relation given by Eq.III.4.).*

S₁ represents the shape containing (110), (111), and (001) facets, schematically shown in figure III.21a. This shape corresponds to figures III.18(e and f) and 19 (d, e, and f) for samples B and C with 100 or 200 nm wide openings oriented along the [110] direction. We apply the Wulff geometric construction to this shape. Doing so, we find the following expression of the parameter h/a (as defined in figure III.21a) as a function of the $\sigma_{(111)}$, $\sigma_{(001)}$, and $\sigma_{(110)}$ surface energies, obtained from simple geometrical arguments:

$$\frac{h}{a} = \frac{\sigma_{(001)}}{\sigma_{(110)}} - \frac{\sigma_{(111)B}}{\sigma_{(110)}\cos(\theta)} + \tan(\theta) \qquad (\text{Eq. III. 1})$$

where θ=54.7°. Using the surface energies in figure III.20, we plot the values of the h/a parameter versus $\Delta\mu_p$, according to Eq.III.1, represented as a solid line in figure III.21d. Let's now compare these plots to the experimental values of the h/a parameter directly measured in the FIB-STEM images, which match the (S_1) shape. For samples B and C (low P/In flux ratio), the resulting h/a values are listed in table III.6, leading to a mean value of 0.45 which corresponds to $\Delta\mu_p$ of -0.5 eV. This latter value is close to the In-rich side, consistent with our experimental conditions. Figure III.18 shows that the surface energy of the (111)B facets is higher than that of the (110) ones by about 13 meV/Å^2. This explains why (110) facets are larger than (111)B ones for sample C and [110]-oriented stripes (figure III.13c).

TABLE III.6. Experimentally measured h/a of samples B, C, and F where the stripes are oriented along [110].

Sample	Openings (nm)	h/a for the stripes oriented along [110]
B	200	0.52
	100	0.4
C	200	0.5
F	200	0.98

We now turn to the shape **S$_2$,** represented in figure III.21b and for which all types of facets are present. This shape is observed for [110]-oriented stripes in sample F (high P/In flux ratio) (figure III.15(d)). Since all the facets existing in **S$_1$** are present in **S$_2$**, Eq.III.1 can still be applied. Once again, the comparison of the plot of Eq.III.2 with the experimental h/a values measured on figure III.15d (sample F, Table III.6) gives the chemical potential for the high value of the P/In flux ratio. The mean h/a is about 0.98, which in turn corresponds to a $\Delta\mu_p \approx -0.2$ eV. For this latter value, figure III.20 clearly shows the reduction of the surface energy of (111)B facets compared to the $\Delta\mu_p$ value calculated before. This explains why (111)B facets are prominent for stripes directed along [110].

The above determination of the chemical potential for each growth condition (low and high P/In flux ratio), should be validated by looking at the [1-10]-oriented stripes. For this reason, we consider the shape (**S$_3$**), schematically drawn in figure III.21c, which is observed in figure III.17b. Once again, applying Wulff geometrical construction allows finding a relation linking the h'/a parameter as defined in figure III.21c and the surface energies as proposed by Lee et al. [5]:

$$\frac{h'}{a} = \frac{\sigma_{(111)A} + \sigma_{(111)B}}{\sigma_{(110)}\cos(\theta)} - 2\tan(\theta) \qquad (\text{Eq. III. 2})$$

The dashed line in figure III.21d represents the variations of h'/a given by Eq.III.2 versus $\Delta\mu_p$ calculated from the surface energies given in figure III.20. The h'/a value for 200 nm wide [1-10]-oriented stripes in sample F is 0.3, and correspond to a $\Delta\mu_p$ of ≈ 0 eV. As discussed previously, this value of $\Delta\mu_p$ cannot be reached in our growth conditions and more is different from the value calculated above ($\Delta\mu_p = -0.2$ eV) which would correspond to an experimental h'/a value of ≈ 0.68. These two reasons appeal to modify the surface energy of (111)A facets, in a way to find a similar value for $\Delta\mu_p$ as that calculated before for the high P/In flux ratio. This leads to a reduction of the (111)A facet surface energy to 47 meV.Å^{-2}. To further justify this assumption, we apply Eq.III.2 to (**S**$_{\mathbf{2}}$) (sample F, apertures along [110]), involving both (111)A and (111)B facets, as (**S**$_{\mathbf{3}}$). The measured h'/a value in this case is 0.31, close to the h'/a value calculated for (**S**$_{\mathbf{3}}$) (sample F, apertures along [1-10]). Therefore, a new value of the (111)A facet energy of 47 meV.Å^{-2} should be considered, i.e. the experimental surface energy ratio between (111)A and (110) facets is 0.86 instead of 1.13, as determined from the calculated surface energies in figure III.20. In the following, we will assume this new value of the (111)A facet surface energy keeping it constant whatever the phosphorus chemical potential.

3.3.3. Nanostructure shape evolution in the first growth stages

As we have shown before, due to the high surface energy cost of (111)B facets at low P/In flux ratio, they are not strongly developed for a deposited thickness of 200 nm and stripes along [110]. However, in the same growth conditions but for a thinner layer (sample A), whatever the stripe width the FIB-STEM image shows that the (111)B facets are prominent.

In the following, from the minimization of the total surface energy and for a stripe opening of 200 nm or 100 nm, the value of the deposited thickness at which the (111)B facets begin to shrink in favor of the (110) ones, is calculated [10]. Two different facet evolutions during growth are considered for [110]-oriented stripes. They are schematically illustrated in the insets of figure III.22. A_1 represents the shape containing a (001) top facet and (111)B side facets, which, by increasing the epilayer thickness, extend until the cross section becomes a triangle. A_2 is a rectangular shape with a (001) top facet of length equal to the opening and (110) vertical facets. The total surface energies per unit length E_1 and E_2 of the corresponding A_1 and A_2 shapes can be written as:

$$E_1 = 2h\left(\frac{\sigma_{(111)B}}{\sin(\theta)} - \frac{\sigma_{(001)}}{\tan(\theta)}\right) \qquad (\text{Eq. III. 3})$$

$$E_2 = 2h'\,\sigma_{(110)} \qquad (\text{Eq. III. 4})$$

The heights h and h' are represented in the insets of figure III.22 and, considering the conservation of the cross section area, h must obey the following relationship which depends on the stripe opening (a):

$$h = \left[\frac{a - \sqrt{a^2 - \frac{4ah'}{\tan(\theta)}}}{2}\right] * \tan(\theta) \qquad (\text{Eq. III. 5})$$

The surface energy of each facet involved in the above equation being known, E_1 and E_2 can be represented as a function of the deposited thickness (figure III.22, dashed and solid lines).

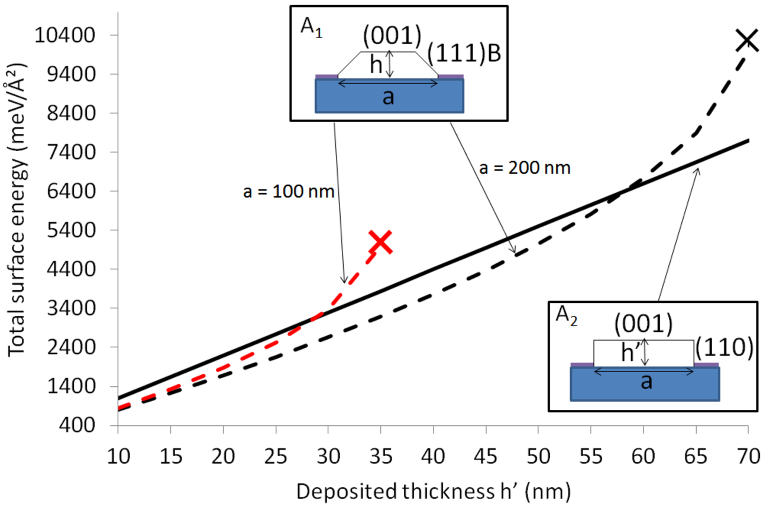

Figure III.22. Plot of the total surface energy versus the deposited thickness as defined in Eqs.III.3 (dashed line) and 4 (solid line). The insets represent the shape evolution with the epilayer thickness considered in each case.

The mark X represents the state where the crystal has a triangular cross section. The red and black dashed lines correspond, to the 100 nm and 200 nm stripe openings, respectively.

A_1 is more energetically favorable than A_2 when the deposited thickness is smaller than 30 nm and 58 nm for the stripe openings of 100 nm and 200 nm, respectively. This can be confirmed from the FIB-STEM of sample A where the stripes opening are 200 nm (figure III.18d). For larger thickness, $E_1 > E_2$ and we infer that the crystal starts developing (110) facets, in good agreement with the FIB-STEM images in figures III.18(e) and 19(d). Finally, these calculations show that along [110], the nanocrystal cannot reach a triangular cross section in our growth conditions since the total surface energy is clearly higher in this case.

3.4. Range of values for the interface energy between InP and the mask

Figures III.15 and 17 evidence a large lateral overgrowth on the mask under low P/In flux ratio whereas it is strongly reduced for the high P/In flux ratio. Lee et al. suggest that the formation of (110) facets (figure 15b) could favor the overgrowth with respect to facets making an obtuse angle with the mask [10]. Nevertheless, this argument can scarcely explain the observed difference in the overgrowth between the two samples since it cannot account for the large overgrowth observed along the [1-10] direction for the low P/In flux ratio, with the formation of extended (111)A facets making an obtuse angle with the mask. This in turn implies that the energy difference between the interface energy between the SiO_2 mask and InP and the SiO_2 surface energy is dependent on the P/In flux ratio. This energy difference between the interface energy between the SiO_2 mask and InP and the SiO_2 surface energy ($\Delta\sigma$) can be defined as:

$$\Delta\sigma = \sigma_{InP/SiO_2} - \sigma_{SiO_2} \qquad \text{(Eq. III. 6)}$$

The value of $\Delta\sigma$ is small with respect to the facet surface energies for the low P/In ratio whereas it is increased for high values of this ratio. To go further, we consider a crystal shape without overgrowth on the mask, called **SS**. Accordingly, by applying the minimization of total surface energy approach between experimental shapes of samples B and C vs the shape **SS**, we get a range of values for the interface energy between InP and SiO_2. As presented in the beginning of this section, for a defined chemical potential, the ratios h/a or h'/a (as defined in figure III.21(a, b, and c)) should be constant. We therefore assume the conservation of both the cross section area and the h/a or h'/a ratio for the shape **SS**.

Figure III.23a represents the FIB-STEM image for the apertures oriented along [110] of sample B associated with the shape **SS** having the same surface as the experimental one (yellow lines).

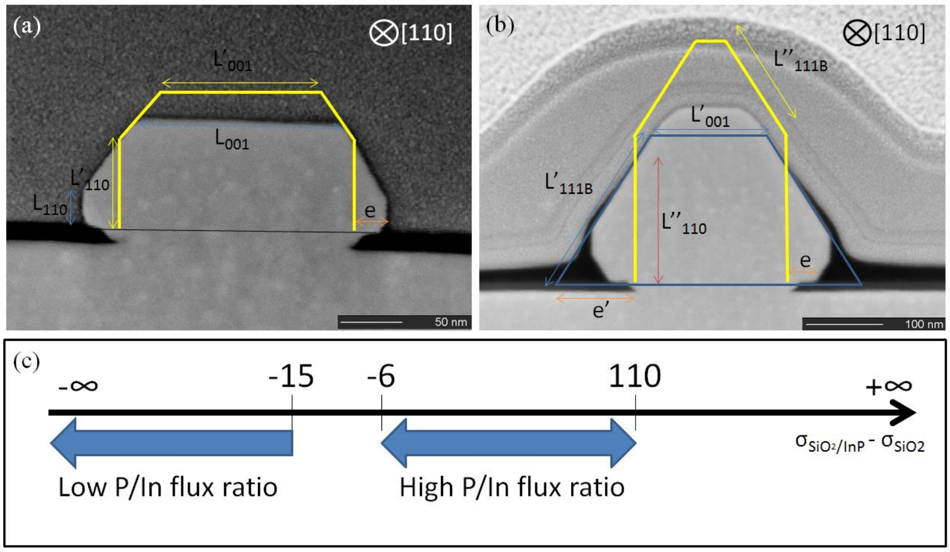

Figure III.23. FIB-STEM images recorded after InP growth in apertures of 200 nm wide directed along [110] for sample B (a) and F (b). Plot of the ranges of surface energy between InP and SiO_2 for low and high value of P/In flux ratio (c).

The total surface energy for the experimental and **SS** shapes are σ_{exp} and σ_{SS}, respectively. By applying the fact that $\sigma_{exp} < \sigma_{ss}$ in figure III.25a we get the following equation:

$$\Delta\sigma \ < \ \frac{2(L'_{110}-L_{110}).\sigma_{110}+\,(L'_{001}-\,L_{001}).\sigma_{001}+2(L'_{111B}-\,L_{111B})\sigma_{111B}}{2\,e} \qquad \text{(Eq.III.7)}$$

where L_{110}, L_{001}, L_{111B}, L'_{110}, L'_{001} and L'_{111B} are the (110), (001), and (111)B facet lengths of the experimental and SS shapes, respectively. e is the lateral overgrowth on the mask of the experimental InP-nanostructures. Eq.III.7 applied to sample B (low P/In ratio) leads to $\Delta\sigma < -20$ meV/Å^2.

The same methodology was applied for sample C with the apertures oriented along [110]. Since there is an asymmetry in InP-nanostructure in this case ($\neq$ values of e), we consider a mean value for the lateral overgrowth on the mask. Using Eq.III.7 and sample C results in similar values: $\sigma_{SiO_2/InP} - \sigma_{SiO_2} < -10$ meV/Å^2. As a conclusion for a low value of P/In flux ratio, the value of $\Delta\sigma$ is less than -15 meV/Å^2. This result is schematically presented in figure III.23c.

If we turn now to the discussion on the high P/In flux ratio, we notice that the lateral overgrowth on the mask in this case is lesser than for low P/In flux ratio. Once again, we consider the shape **SS** without overgrowth on the mask, with the same cross section area, keeping a shape with the same h/a or h'/a ratio (figure III.23b(yellow lines)). Using Eq.III.8, we get the following inequality: $\Delta\sigma < 110$ meV/Å^2. Since the surface energy of (111)B facets in the case of high P/In flux ratio is lower than that of other facet, a shape with (111)B facets and a (001) top one can be assumed (figure III.23b(blue lines)). Applying the minimization of total surface energy between experimental shapes of sample F and this shape, we get the following equation:

$$\Delta\sigma \ > \ \frac{2(L'_{111B}-L_{111B}).\sigma_{111B}+\,(L'_{001}-\,L_{001}).\sigma_{001}-2L_{110}\sigma_{110}\,-2L_{111A}\sigma_{111A}}{2\,(e-e')} \qquad \text{(Eq.III.8)}$$

This equation threads to the following inequality: $\Delta\sigma > -6$ meV/Å^2. Therefore, the range values of $\Delta\sigma$ lies between -6 and 110 meV/Å^2. Figure III.23c combines the results of high and low P/In flux ratio, evidencing the difference between the calculated ranges of $\Delta\sigma$.

Referring to Eq. I.5 (see chapter I):

$$\begin{cases} \Delta\sigma_{Low\,P/In} = \sigma_{InP} - \beta \\ \Delta\sigma_{High\,P/In} = \sigma'_{InP} - \beta' \end{cases} \qquad \text{(Eq.III.9)}$$

where β (β') and σ_{InP} (σ'_{InP}) is the adhesion energy of InP on SiO$_2$ and the InP surface energy at low (high) P/In flux ratio respectively. Actually, from figure III.20, we notice that $\sigma_{InP} \geq$

σ'_{InP} whatever the facet considered. Therefore, from Eq.III.9, since $\Delta\sigma_{High\,P/In} > \Delta\sigma_{Low\,P/In}$ (see Figure III.23c), we can infer that the adhesion energy is higher at low P/In flux ratio (β > β').

3.5. Conclusion

We have shown that the faceting of InP nanostructures selectively grown inside 200 nm and 100 nm wide stripes by MBE on an InP(001) substrate can be tailored playing with the P/In flux ratio and the deposited thickness. Indeed, for the [110]-oriented stripes, we demonstrate that the extension of the (111)B facets can be controlled by the P/In flux ratio since the surface energy of these facets is strongly dependent on the phosphorus chemical potential. On the other hand, the [1-10]-oriented stripes are not strongly affected by the P/In flux ratio. We have discussed our whole set of observations in the framework of the facet kinetics and the ECS model using previously reported surface energies for the different facets, taking properly into account their variations with the changes in chemical potential induced by different experimental conditions. A general agreement could be achieved if the surface energy of the (111)A facets with respect to the other ones is reduced. In this way, an experimental $\sigma_{(111)A}/\sigma_{(110)} = 0.86$ compared to 1.13 using calculated values has been determined. We also discuss the evolution of the nanostructure shape with the InP-deposited thickness. We then explain that although the surface energy of (111)B facet is large for low P/In flux ratios, the minimization of the total surface energy leads to the formation of prominent of (111)B facets for the [110]-directed stripes in the early growth stages. By mean of the minimization of total surface energy approach we determine a range value for the energy difference between the interface energy between the SiO_2 mask and InP and the SiO_2 surface energy for low and high value of P/In flux ratio.

As for InAs, we determine the shape evolution when the growth proceeds. Accordingly, we calculate the ratio of the experimental thickness (T_{exp}) over the opening width (W), where T_{exp} is obtained by calculating the ratio of the InP nanostructure cross-section surface over W (W is 100 or 200 nm). Figures III.24 and 25 schematically present the shape evolution when the growth proceeds for the stripes oriented along [110] and [1-10] direction respectively.

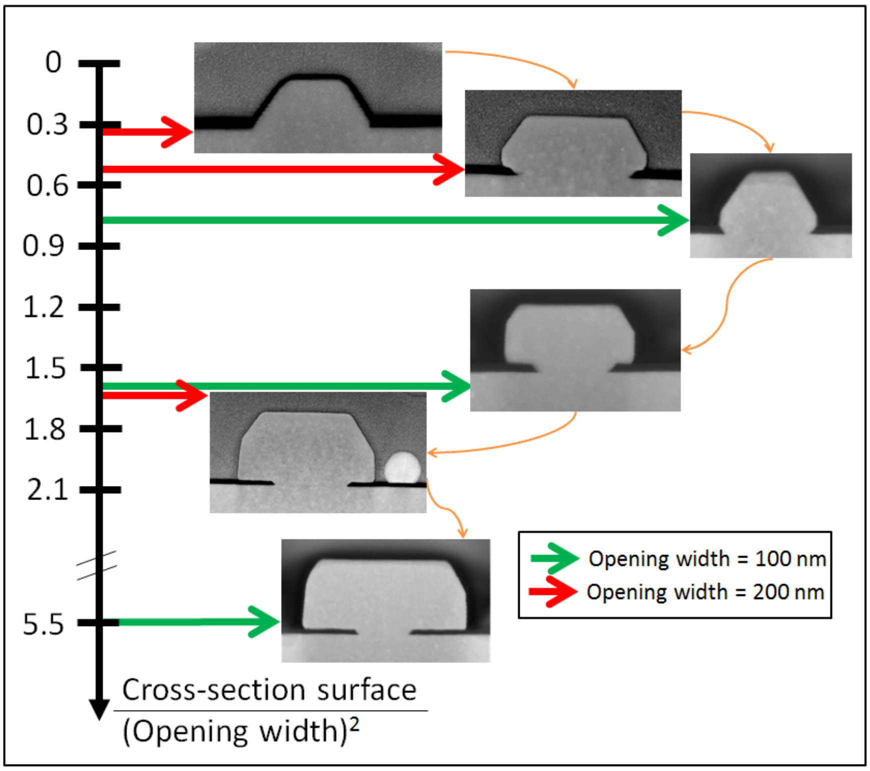

Figure III.24. Schematic of the shape evolution inside the stripe oriented along [110] when the growth proceeds.

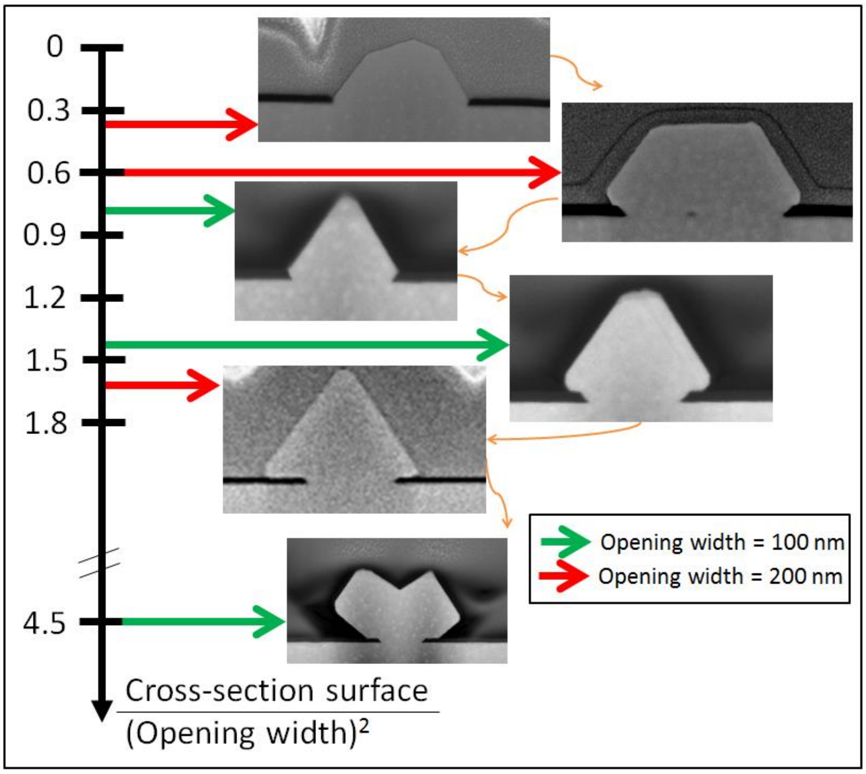

Figure III.25. Schematic of the shape evolution inside the stripe oriented along [110] when the growth proceeds.

4. General conclusion

In this chapter, we have made a detailed study for the selective homoepitaxy of InAs and InP. We notice a different crystal evolution between the two materials. For the SAG of InAs, the high interface energy between InAs and the mask impedes the crystal to freely evolve and therefore prohibits the use of the ECS model to interpret the results, although the SAG is not kinetically limited. Indeed, the migration flux from the lateral facets continuously changes the chemical potential which in turn prohibits reaching a definite equilibrium shape.

In the case of the InP SAG, the surface energy between InP and the mask appears to be low, in such a way that it does not influence the lateral overgrowth of the crystal. Therefore, once lateral overgrowth has occurred, the nanocrystal evolves as a free one and results can be consistently interpreted within the ECS model.

References

1. C. Thelander, P. Caroff, S. Plissard, A.W. Dey and K.A. Dick, Nano Lett. 11, 2424, 2011.

2. A. G. Taboada, M. Meduňa, M. Salvalaglio, F. Isa, T. Kreiliger, C. V. Falub, E. Barthazy Meier, E. Müller, L. Miglio, G. Isella, and H. von Känel, J. Appl. Phys. **119**, 5, 055301, 2016.

3. N. Moll, M. Scheffler, and E. Pehlke, ArXiv Prepr. Cond-Mat 9807200, 1998.

4. M. Fahed, L. Desplanque, C. Coinon, D. Troadec, and X. Wallart, Nanotechnology **26**, 29, 295301, 2015.

5. S. C. Lee, D. L. Huffaker, and S. R. J. Brueck, Appl. Phys. Lett. **92**, 2, 023103, 2008.

6. Q. K. K. Liu, N. Moll, M. Scheffler, and E. Pehlke, Phys. Rev. B **60**, 24, 17008, 1999.

7. C. Rottman and M. Wortis, Phys. Rep. **103**, 1–4, 59–79, 1984.

8. E. D. Williams and N. C. Bartelt, Ultramicroscopy **31**, 1, 36–48, 1989.

9. P.-S. Wong, B. Liang, R. Molecke, J. Tatebayashi, and D. L. Huffaker, Cryst. Growth Des. **10**, 6, pp. 2509–2514, 2010.

10. S. C. Lee, L. R. Dawson and S. R. J. Brueck, Appl. Phys. Lett. **87**, 071110, 2005.

Chapter IV: Heteroepitaxial selective area growth of InAs/GaSb nano-heterostructures on GaAs(001)

This chapter deals with the optimization of the conditions to achieve selective growth of GaSb on GaAs using MBE. The growth temperature (GT), the presence of an atomic hydrogen flux during the growth and the Sb/Ga flux ratio are investigated to promote selectivity and filling of the mask apertures with GaSb. We then use the obtained GaSb nano-ribbons as nanotemplates for subsequent epitaxial growth of high structural quality in-plane InAs nanowires. After the epitaxial growth, scanning electron microscopy (SEM), atomic force microscopy (AFM), scanning transmission electron microscopy coupled with focused ion beam preparation (STEM-FIB), as well as X-ray diffraction (XRD) and extended STEM analysis were carried out to analyze the morphological and structural properties of the layers. Energy dispersive X-Ray (EDX) analysis was also performed to determine the chemical composition of the deposited layers.

1. Optimization of the GaSb/GaAs selective growth

In this section, we first investigate the role of GT on the selectivity as well as on the stripe filling. We then show that the use of an atomic hydrogen flux during the growth promotes selective epitaxy at low GT where a few micron long high quality GaSb nano-ribbons can be obtained in both [110] and [1-10] orientations. Finally, we highlight the influence of the Sb/Ga flux ratio on the growth on GaSb nanostructures inside opening windows and on the strain relaxation of GaSb nanowires oriented along the [110] and [1-10] directions.

1.1. Growth temperature

For the samples presented in this section, the pattern consists of 100 nm wide and 4 µm long stripe openings and the GaAs native oxide layer is removed by thermal annealing at 620°C under an As flux in the MBE chamber. This deoxidization procedure induces some surface roughness as evidenced by RHEED and AFM observations on a bare GaAs sample with no mask (see chapter II). Indeed, a ‘spotty’ (2x4) RHEED pattern was observed after deoxidization whereas AFM measurements lead to a RMS roughness value of 3 nm (see chapter II). Therefore, in order to smooth the GaAs starting surface, prior to GaSb growth, we deposited 25 nm GaAs at 590°C and 0.1 ML.s^{-1}. During GaSb subsequent growth, the Sb/Ga flux ratio was 10 and the GaSb GT was varied between 470°C to 540°C. Figures IV.1(a-f) show the SEM images of the nanostructures oriented along [110] and [1-10] for GaSb GT of

470°C, 510°C, and 540°C. The first noticeable evolution is related to the growth selectivity, which is achieved at 540°C but not at all for lower temperatures where polycrystalline GaSb forms on the mask.

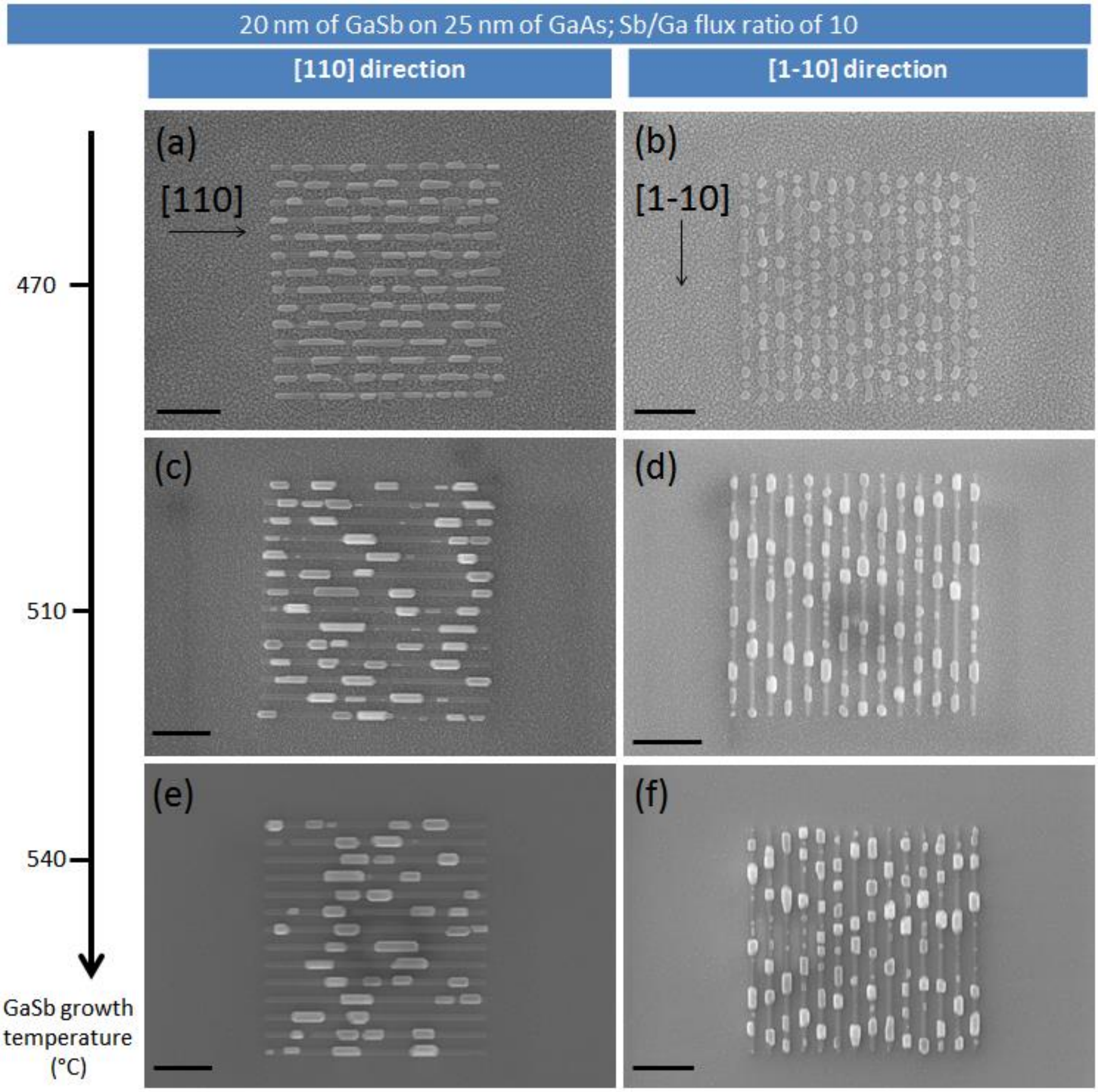

Figure IV.1. SEM images recorded after the growth of 20 nm GaSb on 25 nm GaAs for apertures directed along [110] and [1-10] when varying the GaSb growth temperature: 470°C (a and b), 510°C (c and d), and 540°C (e and f). The scale bar represents 1 µm.

Figure IV.1 also reveals strong changes in the nanostructure continuity and shapes. As expected, the stripe filling increases with decreasing GT, the island density in the [1-10] direction being higher than that in the [110] one at each temperature. Anyway, whatever the

GT, the stripe filling remains incomplete, resulting in disrupted lines. Regarding the nanostructure shapes, figure IV.1 clearly evidences the preferential GaSb nanostructure elongation along the [110] direction. In order to determine the mean length and height of the GaSb nanostructures, AFM measurements have been performed. Figure IV.2(a) shows an example of an AFM image recorded for the stripes along [110] and a GT of 540°C. From this later, the nanostructure profiles (length and height) are extracted for each stripe. Figure IV.2(b) represents such a profile, taken along the black line shown in the AFM image. Similar line profiles were done on all the stripes to get the average length and height of the nanostructures.

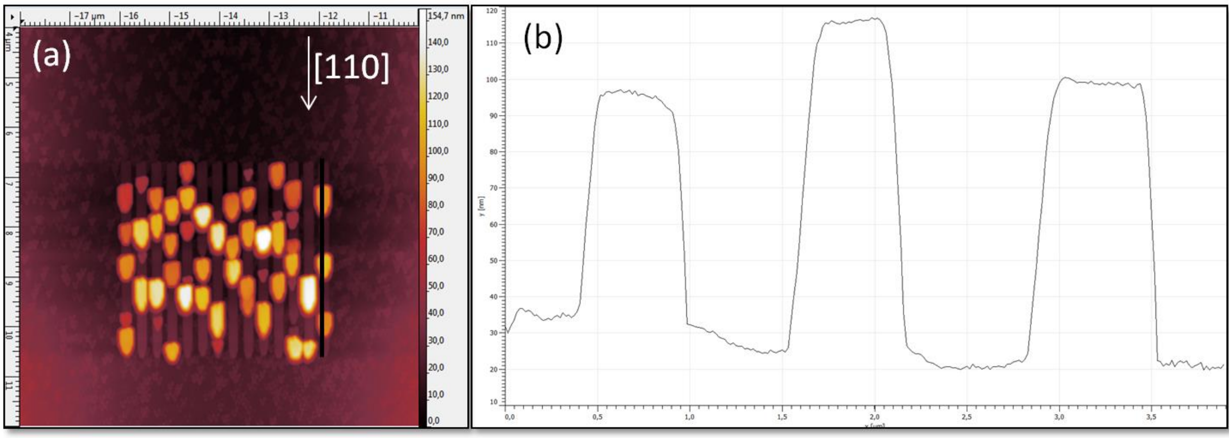

Figure IV.2. (5x5) µm^2 AFM image recorded for the apertures directed along [110] after the growth of 20 nm GaSb at 540°C on 25 nm GaAs (a). Length and height nanostructure profiles along the black line presented in the AFM image (b).

The results for the different samples are gathered in Table IV.1. For [110]-oriented apertures, the average length does not evolve significantly whereas the mean height increases with GT. In the case of [1-10] stripes, higher GT leads to larger height and length. However, this larger length does not improve the stripe filling since it goes together with a reduced nanostructure density along the stripes. Figure IV.1 clearly evidences that a complete filling of the stripes requires a rather low GT and an increased deposited thickness.

Table IV.1. The average length (l) and height (h) of GaSb-nanostructures inside the patterns oriented along [110] and [1-10] directions when varying the GaSb growth temperature: 470°C, 510°C, and 540°C.

Stripe direction / GaSb growth temperature (°C)	[110]		[1-10]	
	l (nm)	h (nm)	l (nm)	h (nm)
470	453	35	158	40
510	455	86	187	76
540	463	104	214	88

A too high GT favors Ga adatom diffusion on GaAs and, together with the large lattice mismatch between GaSb and GaAs, leads to the formation of 3D nanostructures. An interesting point is that this nanostructure formation depends on the opening orientation with a strong preferential elongation along the [110] direction. This evidences anisotropic Ga adatom diffusion as already noticed during GaSb growth on bare GaAs substrates [1] with the formation of [110] elongated islands under Sb-rich conditions. Larger Ga diffusion length results from increasing GT and leads to higher nanostructures in both directions, but only affects the island length for openings along [1-10] since the nanostructure length along [110] is already large at low GT. Regarding the samples presented in figure IV.1 for which a 25 nm-thick GaAs deposition has been performed prior to GaSb growth, we cannot exclude some influence of GaAs faceting on the formation of the GaSb nanostructures. Indeed, after GaAs deposition (113) and (100) facets are formed in the [110] stripes whereas mainly (111) facets appear in the [1-10] ones. However, it has been reported that the (001) facet exhibits the smallest Ga adatom diffusion length among low-index ones [2]. Therefore the formation of the (001) GaAs facet cannot account for the preferential elongation along the [110] direction for [110] stripes.

In order to avoid the effect of the faceted GaAs surface, in the following, the GaAs native oxide layer will be removed by a moderate thermal annealing at 450°C under combined atomic hydrogen and Sb fluxes in the MBE chamber. This results in a smooth surface without any further GaAs deposition, as attested by a streaky (2x4) RHEED pattern on the bare GaAs surface, confirmed by AFM measurements, leading to a RMS roughness value of 0.3 nm for hydrogen assisted GaAs substrate deoxidization (see chapter II). More, they agree with previous ones demonstrating smooth surface morphology upon atomic hydrogen cleaning of GaAs (001) surfaces [3].

Since the challenge is to achieve the selectivity at low GT, the use of atomic hydrogen during the growth to improve the selectivity will be discussed in the following section.

1.2. Atomic hydrogen flux during the growth

Figures IV.3(a and b) show the SEM images after deposition of 65 nm of GaSb at 470°C without atomic hydrogen. Polycrystalline GaSb covers almost all the mask, but an upsurge of GaSb nanostructure length inside the stripes can be noticed. GaSb deposition in the [110]-oriented stripes leads now to complete lines whereas for [1-10] stripes, the GaSb nanostructure average length increases to 1.5 µm.

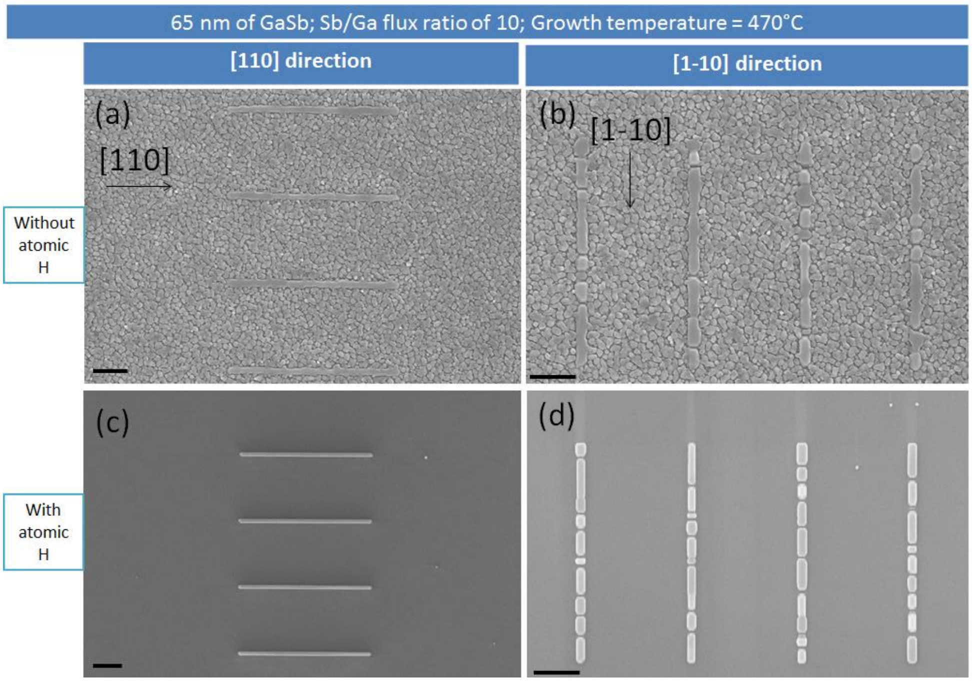

Figure IV.3. SEM images recorded after 65 nm of GaSb growth at 470°C in apertures directed along [110] and [1-10]: without atomic H (a and b) and with atomic H (c and d). The scale bar represents 1 µm.

As it has been shown in the case of the SAG of GaAs [4], we tried to enhance the selectivity at 470°C using an atomic hydrogen flux during GaSb growth. The SEM images (figures IV.3(c and d)) clearly confirm this improvement. Furthermore, atomic hydrogen does not seem to alter the GaSb nanostructure morphology since, along the [110] direction, the formation of continuous GaSb lines is maintained whereas along the [1-10] one, the GaSb nanostructure average length remains around 1.3 µm.

Regarding the role of atomic hydrogen on the selectivity, in the case of GaAs, Sugaya et al. have proposed a mechanism based on the enhanced Ga and As desorption from the SiO_2

surface due to the formation of Ga and As hydrides [5]. In the same way, Kuroda et al. have shown that the dominant factor of the selective growth mechanism is not Ga atom migration from the masked regions to the growing regions, but Ga atom desorption from the mask surface. In our case, the atomic hydrogen assisted desorption may also occur in the form of Ga hydrides since the bond strength of Ga-H (66 kcal/mol) is larger than that of Ga-Sb (46.23 kcal/mol) [6]. Therefore, on the mask surface, the Ga atoms tend to bind with atomic hydrogen rather than with Sb atoms, impeding the formation of polycrystalline GaSb on the mask surface [7]. This in turn may imply that for atomic hydrogen assisted growth of GaSb on a bare GaAs surface, hydride formation could occur and result in a lower thickness than the nominal one. But, Kobayashi et al. have reported that atomic hydrogen reacts with Ga atoms and removes them from the GaAs surface only if it is annealed above 850°C [8].

In order to check this effect, we have measured the GaSb thickness after the growth of 65 nm of GaSb under atomic hydrogen flux on a bare GaAs surface using the full width at half maximum (FWHM) of the GaSb peak on the (004) ω-2θ XRD spectrum. The relation between the GaSb thickness (T) and the GaSb pic FWHM (w) is given by [9]:

$$T = \frac{5.56624}{w} \qquad \text{(Eq.IV.1)}$$

Figure IV.4(a) represents the (004) ω-2θ T-XRD spectra of the GaSb peak (blue line), together with a fit using a Gaussian shape (red line). The FWHM is about 0.09025 nm^{-1}, which corresponds to a thickness of ≈ 63 nm. Therefore, we do not find any noticeable difference between the deposited and the measured GaSb thickness, which means that there is no significant effect of the atomic hydrogen on the GaSb nanocrystals growth on GaAs.

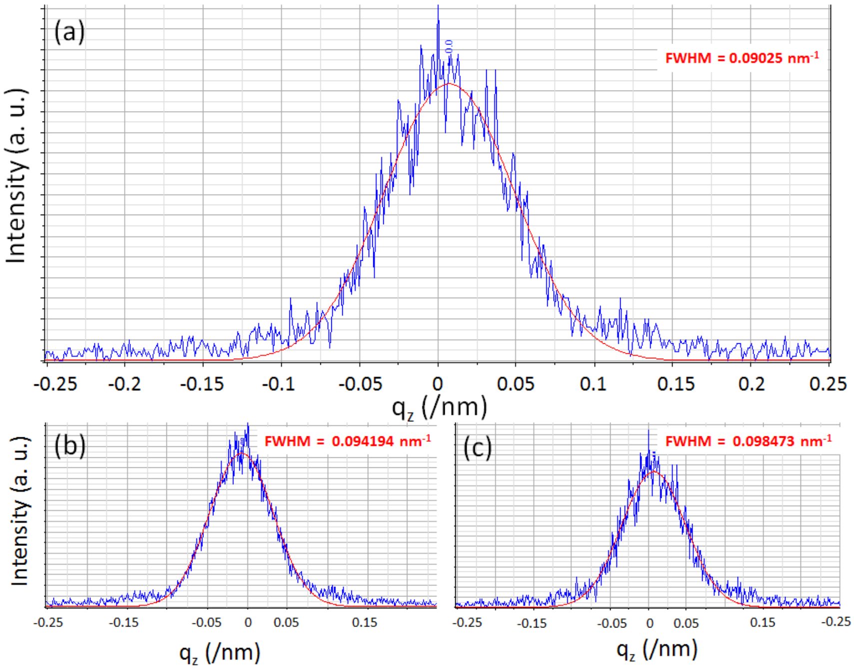

Figure IV.4. (004) ω-2θ T-XRD GaSb peak recorded after the growth of 65 nm of GaSb at 470°C with atomic H on a bare GaAs substrate (a), and on a sample with patterns at Sb/Ga = 20 (b) and Sb/Ga = 2 (c) .

To compare the deposited thickness to the nominal one on the patterned substrates, special dense patterns were fabricated to improve the sensitivity for XRD measurements. These special dense patterns consist in 10 µm long, 100 nm wide and 200 nm spaced stripe openings oriented either along [110] or [1-10] inside a (3x3) mm^2 square (Figure IV.6(a)). These latter were In soldered on the sample holder together with the patterned GaAs (001) and the 2D samples. Figures IV.6(b and c) show SEM images of top and tilted views, respectively, recorded after the growth of 65 nm GaSb at 470°C with atomic H in apertures directed along [110].

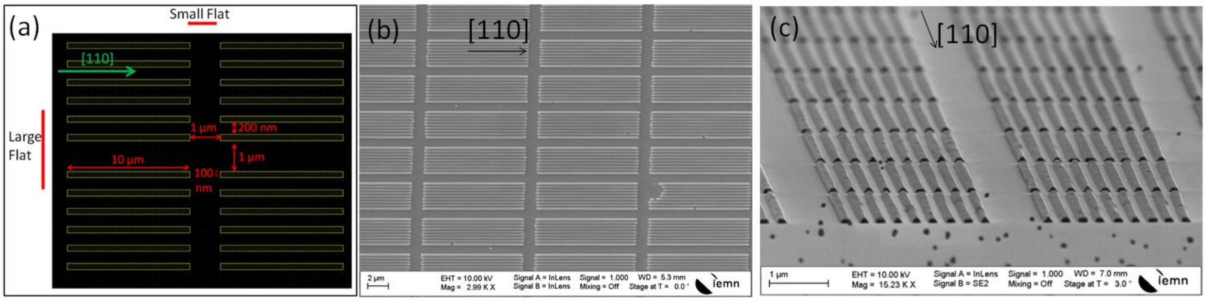

Figure IV.5. Schematic of the pattern used for XRD measurements (a), SEM images top and tilted views (b and c) recorded after 65 nm GaSb growth at 470°C with atomic H in apertures directed along [110].

Once again we have measured the GaSb thickness after deposition of 65 nm GaSb under atomic hydrogen using the FWHM of the GaSb peak on the (004) ω-2θ XRD spectrum. Figures IV.4(b and c) represent the (004) ω-2θ T-XRD GaSb peak (blue line) with the fitted lines using a Gaussian shape (red line). These spectra where obtained for the samples grown with a Sb/Ga flux ratio of 20 and 2. The FWHM is about 0.096 nm^{-1}, which corresponds to a thickness of ≈ 60 nm. No significant difference between the deposited and the measured GaSb thickness for the patterned substrates can then be noticed. This implies also that there is no strong effect of the diffusion from the mask surface to the opening windows.

As reported by Bachrach et al., investigating the interaction between atomic hydrogen and (001) GaAs surfaces, the formation of Ga hydrides is restricted to the top surface layer and cannot be ascribed to an etching mechanism [10]. The improved selectivity noticed with atomic hydrogen is therefore not due to an increase of the Ga adatom diffusion length on the mask surface towards the stripes but to a shortening of the species residence time on the SiO_2 surface due to the easy hydride formation. This in turn implies that the observed growth morphology is almost independent on the stripe density since a very small amount of material diffuse from the mask inside the stripes. This is confirmed by the SEM images in figures IV.1 and 3 where no diffusion related area could be distinguished around the stripes.

1.3. Sb/Ga flux ratio

In this section, we highlight the Sb/Ga flux ratio effect on the GaSb nanostructure formation. We present the results concerning the growth of 65 nm GaSb at a fixed GT of 470°C and using atomic hydrogen during growth, when varying this ratio between 2 and 20. Firstly, we study the GaSb nanostructure morphology inside opening windows oriented along either [110] or [1-10] direction. Then, we focus on the strain relaxation of GaSb nanowires on GaAs.

1.3.1. GaSb nanostructure morphology

We start with the two extreme values of the Sb/Ga flux ratio, 2 and 20. SEM images in figures IV.6(a and c) reveal that along the [110] direction, no major difference can be detected and both ratios lead to continuous lines. However, along [1-10], figures IV.6(b and d) indicate that a low Sb/Ga flux ratio (2) leads to larger segments. This is confirmed by the values of the nanostructure average length, which are 300 nm and 2 µm for the high and low Sb/Ga flux ratio, respectively.

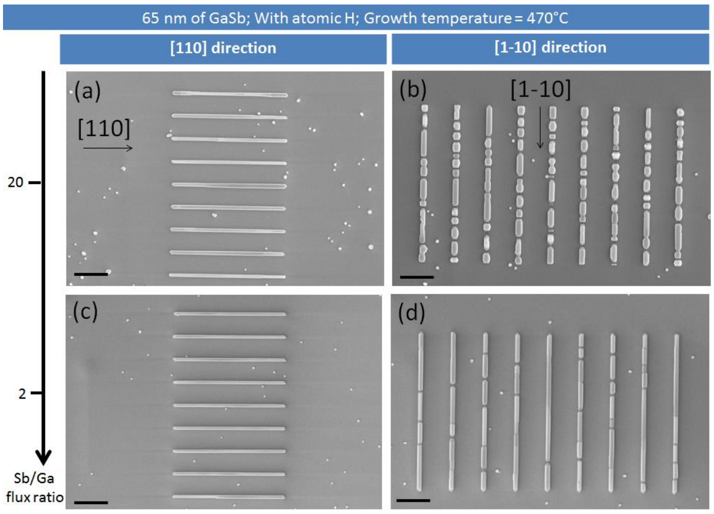

Figure IV.6. SEM images recorded after 65 nm of GaSb growth at 470°C in apertures directed along [110] and [1-10] varying the Sb/Ga flux ratio. Sb/Ga = 20 (a and c) and Sb/Ga = 2 (c and d). The scale bar represents 1 µm.

This trend has been observed for the other values of the Sb/Ga flux ratio (5 and 10). Figure IV.7 depicts the variation of the clipping density and nanostructure mean length inside the apertures directed along the [1-10] direction when varying the Sb/Ga flux ratio. A large increase (decrease) of the clipping density (mean length) is observed when the Sb/Ga flux ratio is varied from 2 to 10, preceding a smoother evolution when the Sb/Ga flux ratio is further raised to 20.

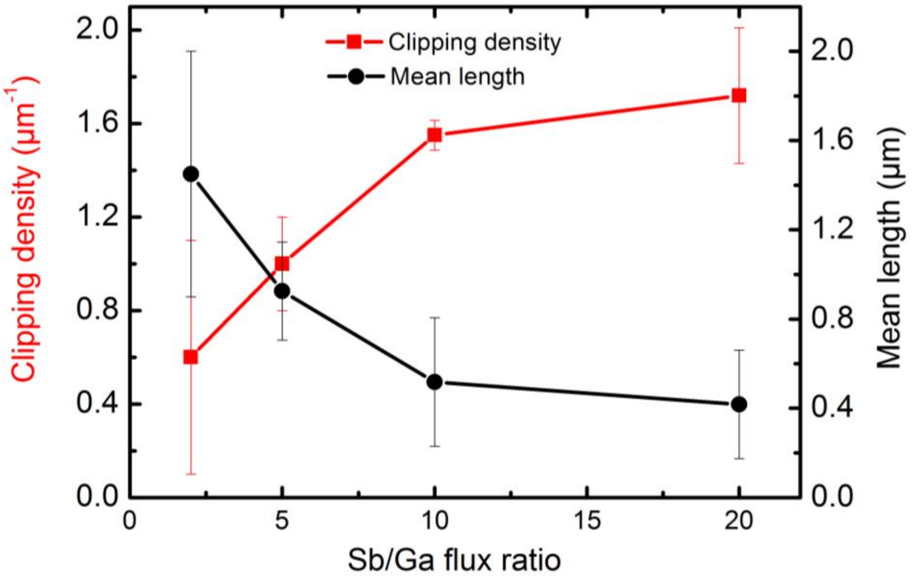

Figure IV.7. Variations of the clipping density and nanostructure mean length versus Sb/Ga flux ratio after the growth of 65 nm GaSb at 470°C with atomic H inside stripes oriented along [1-10].

Therefore, the stripe morphology is influenced by the Sb/Ga flux ratio and a low Sb/Ga ratio promotes GaSb nanostructure coalescence inside [1-10]-oriented stripes, the [110] ones being far less sensitive. This behavior can be first interpreted by the enhancement of the Ga adatom diffusion length along [1-10] when decreasing the Sb/Ga flux ratio, leading to larger nanostructures. However, a close examination of figure IV.6(b) shows that the nanostructures inside the [1-10] lines are very close to each other, which is different from the situation depicted in figures IV.1(b, d, f). This makes the interpretation in terms on diffusion length only not completely convincing.

On the other hand, the clipping inside the stripes along [1-10] is not due to an anisotropic deoxidized opening between the two directions and this is shown in the Annex part.

In order to complete the information about this difference, FIB-STEM observations were carried out for the two extreme cases (figures IV.8(a-c)). For [110]-oriented stripes (figures IV.8(a and b)), no major shape difference can be detected varying the Sb/Ga flux ratio. The cross section mainly exhibits lateral (111)B facets and a (001) facet at the top. Figure IV.8(c) presents the FIB-STEM image for stripes along [1-10] and the low Sb/Ga flux ratio value. The cross section exhibits a rectangular shape with lateral (110) facets, small (111)A ones at the top corners and a (001) on top. The high number of clippings of the stripes grown with a high Sb/Ga flux ratio prevents FIB-STEM observation in this case.

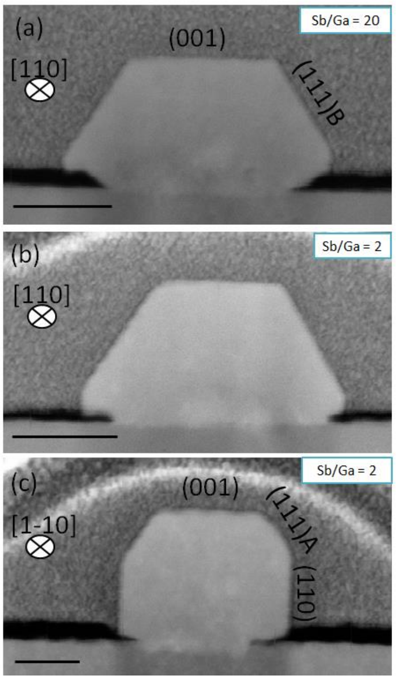

Figure IV.8. FIB-STEM (a, b and c) images recorded after 65 nm GaSb growth at 470°C with atomic H in apertures directed along [110] and [1-10] varying the Sb/Ga flux ratio. Sb/Ga = 20 (a), Sb/Ga = 2 (b and c). The scale bar on the FIB-STEM images represents 50 nm.

A piece of explanation for the observed behavior along the [1-10] direction can be brought by the FIB-STEM cross section images in figures IV.8(a and b), which clearly indicate a strong tendency to the formation of (111)B facets, probably related to their lower surface energy with respect to the other ones. Indeed, for GaAs [11], InAs [12] and InP [13], previous calculations have demonstrated the strong decrease of the (111)B surface energy with increasing group-V element flux. We are not aware of such calculations for GaSb but we assume the same trend holds. Then for [1-10]-oriented stripes and a high Sb/Ga ratio, (111)B facets have a low surface energy and are easily formed normal to the line, promoting the formation of rather small nanostructures which may also contribute to the elastic relaxation via increased surface area. The high clipping density observed along [1-10] stripes could then be attributed to the easy formation of (111)B facets, which are Sb-terminated and may exhibit Sb-Sb bond [14] formation impeding Ga adatom incorporation and leading to a low growth rate [15] (figure IV.9). On the contrary, for low Sb/Ga flux ratio values, the formation of Sb-Sb bonds is almost suppressed, the (111)B surface energy is higher and accordingly its growth rate increases, resulting in a larger spreading of the nanostructure. Therefore, we demonstrate that reducing the Sb/Ga flux ratio during growth leads to improved line continuity along [1-10].

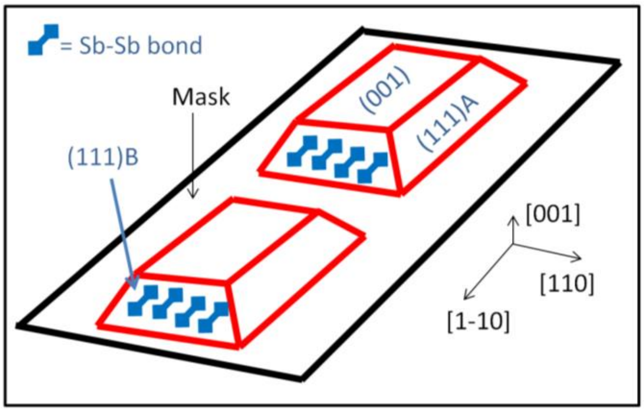

Figure IV.9. Schematic illustration of GaSb nanostructures where showing the facets in different crystallographic directions.

1.3.2. GaSb-lattice relaxation

XRD measurements have been carried out to characterize more precisely the GaSb relaxation within the stripes for samples grown at Sb/Ga flux ratio of 20 and 2. For each sample, two types of XRD measurements were carried out, in the (004) reflection using an analyzer in front of the detector and in the (220) grazing incidence geometry (GIXD), without analyzer. The (004) ω-2θ spectrum allowed the determination of the lattice parameter in the [001] growth direction, whereas the (220) spectra gave a direct measurement of the in plane [110] and [1-10] ones (see chapter II). Assuming then pure GaSb growth leads to the calculation of GaSb relaxation along the different directions.

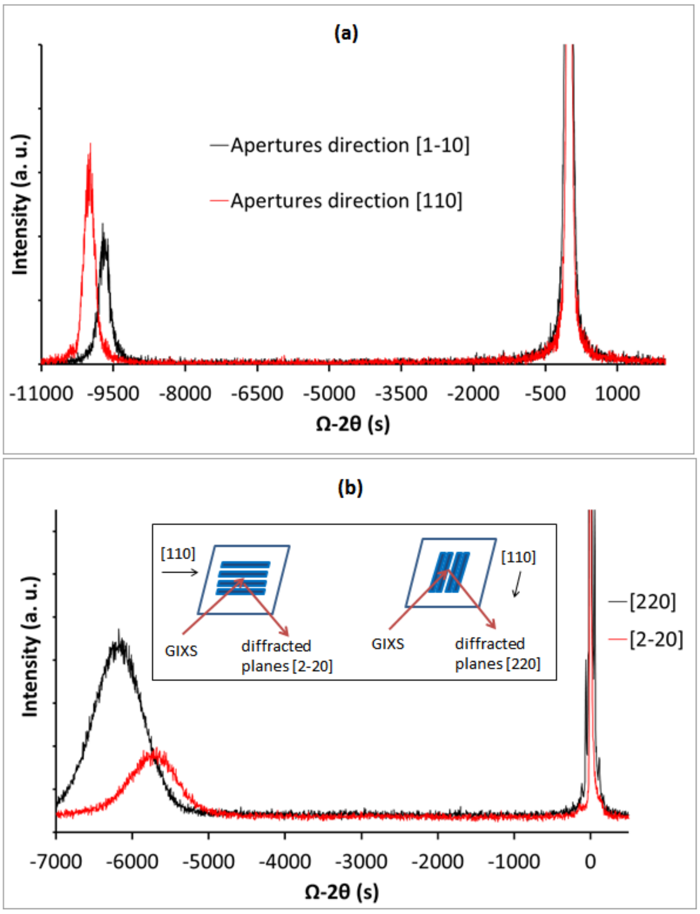

Figure IV.10. Typical XRD ω-2θ scan for 65 nm of GaSb deposited at 470°C with atomic H and a Sb/Ga flux ratio of 20. (004) ω-2θ spectra for apertures directed along [110] and [1-10] (a); GIXD (220) spectra for apertures directed along [110] (b). The inset in figure (b) represents the stripe positions with respect to the X-Ray beam.

For a high value of the Sb/Ga flux ratio, (004) ω-2θ and (220) GIXD spectra are presented in figures IV.10(a and b), respectively. Table 2 summarizes the calculated GaSb lattice relaxation from these measurements and compares them with those obtained on a bare GaAs substrate (2D growth). The calculated relaxation values in the [001] direction, deduced from the measurements along the [110] and [1-10] ones using GaSb elastic coefficients are listed in the last line in Table 2. The agreement between these calculated values and the measured ones in the (004) ω-2θ geometry confirms the overall consistency of our analysis. When varying the Sb/Ga flux ratio, no major change in GaSb lattice relaxation is observed for the 2D growth

(97%) and for the apertures directed along [1-10] (99%). However, for the apertures directed along [110], the GaSb lattice relaxation decreased with increasing Sb/Ga flux ratio. From the GIXD measurements, it appears that this relaxation reduction could be mainly attributed to a relaxation decrease along the [110] direction from 94.2% (Sb/Ga=2) to 90.7% (Sb/Ga =20).

Table IV.2. GaSb lattice relaxation (R) on GaAs(001) substrate.

Sb/Ga flux ratio	20		2	
R along (004) for 2D growth ± 0.1%	97%		97%	
Stripes directions Relaxation	[110]	[1-10]	[110]	[1-10]
R along (004) ± 0.1%	95%	99%	97%	98.5%
R along (1-10) ± 0.5%	99.3%	98.9%	99.5%	98.2%
R along (110) ± 0.5%	90.7%	99.4%	94.2%	98.6%
Calculated R along (004) from the (220) and (2-20) measurements ± 0.5%	95.0%	99.2%	96.9%	98.8%

The main result from the XRD measurements in Table IV.2 is that the strain relaxation is larger along the stripe direction for [1-10] oriented stripes than for [110] oriented ones. This difference originates in the weak relaxation along the [110] direction. For the high Sb/Ga value, considering the small size of GaSb nanostructures within the [1-10] stripes, the effect of elastic strain relaxation at the nanostructure surface in addition to the plastic one arising from MDs at the interface with the substrate might be considered. However, at low Sb/Ga value, the [1-10] lines become more continuous without any significant degradation of the relaxation. More, along the [110] direction, the relaxation is improved when decreasing the Sb/Ga ratio although the lines remain continuous. Therefore, elastic effects occurring on the nanostructure facets cannot account for the observed behavior. It then turns out that GaSb plastic relaxation is anisotropic, being easier along the [1-10] direction than along the [110] one. Our X-ray results are in agreement with previous reports on 2D growth based on X-ray diffraction analysis using synchrotron radiation and showing that the dislocation spacing is larger for the dislocation array in the [110] direction. This is due to the energy difference between [1-10] and [110] dislocations related to different dislocation cores [16]. More, this different core nature can account for the behavior upon reducing the Sb/Ga flux ratio. Indeed, the core of [110] Lomer dislocations (which relax the strain of [1-10] stripes) has a missing Ga atom whereas the core of the [1-10] Lomer dislocations (which relax the [110] stripes) has a missing Sb atom [17]. Therefore, we can infer that reducing the Sb flux promotes the formation of [1-10] dislocations and improves the relaxation along the [110] direction.

1.4. Conclusion

We have shown that the use of a low GT leads to stripe filling by the GaSb nanostructures but results in a high polycrystalline GaSb deposition on the mask. We achieved the selectivity at low GT thanks to the use of an atomic hydrogen flux during the growth. Moreover, we show that a reduced Sb/Ga flux ratio enhances the GaSb relaxation within the stripes, leading to nearly perfectly relaxed material. Using these optimized growth conditions, we obtain a good template for mismatch accommodation between GaAs and 6.1 Å material. In the following, we use this template for the deposition of an InAs layer.

2. InAs/GaSb/GaAs

In this section, we present three samples, the first consists of the SAG of 10 nm InAs on the top of 65 nm GaSb nanotemplates on GaAs and the two other consist of the 2D and SAG of 10 nm InAs on the top 150 nm of GaSb nanotemplates on GaAs. The studied samples were grown at a Sb/Ga flux ratio of 2 and a GaSb GT of 470°C since it has been shown in the previous section that these conditions lead to the formation of almost continuous GaSb lines in both [110] and [1-10] directions. After the epitaxial growth, extended STEM analysis and XRD were carried out to analyze the structural properties of the layers. Then EDX analysis was performed to determine the chemical composition of the deposited layers. Concerning the STEM and EDX analysis on the selective growths, for each stripe direction, transversal and longitudinal cross-sections were performed. For the XRD analysis, we get information about the GaSb crystalline quality using “Williamson-Hall model” (WHM) or the “Extended version of Williamson-Hall model” (see chapter II). The WHM approach is proposed to evaluate the threading dislocation density (TDD) in the epitaxial films from the width of the diffracted peak ignoring the contribution of misfit dislocations (MDs). Since in this work we study the case of highly relaxed mismatched films it is not obvious to disregard the MDs. That is why we then perform the extended version of WHM. This latter approach consists in assuming that the effect of the TDs can be neglected with respect to that of the MDs.

2.1. Structural analysis

2.1.1. 2D growth

In this section, we discuss the structural characteristics of a 10 nm thick InAs layer on top of a 150 nm thick of GaSb one deposited on a bare GaAs(001) substrate. Preparation of STEM lamellas as well as XRD measurements have been performed along both crystallographic directions ([110] and [1-10]).

a) STEM-analysis

Figures IV.11 presents the STEM cross-section images along [110] and [1-10]-directions. The high-angle annular dark-field (HAADF) and the bright field images reveal the structural quality of the GaSb layer which is relaxed mainly through a regular array of Lomer dislocations at the interface. The distance between these dislocations, in both crystallographic directions, is around 5.7 nm and we notice some TDs inside the GaSb layer (marked by red arrows on figures IV.11).

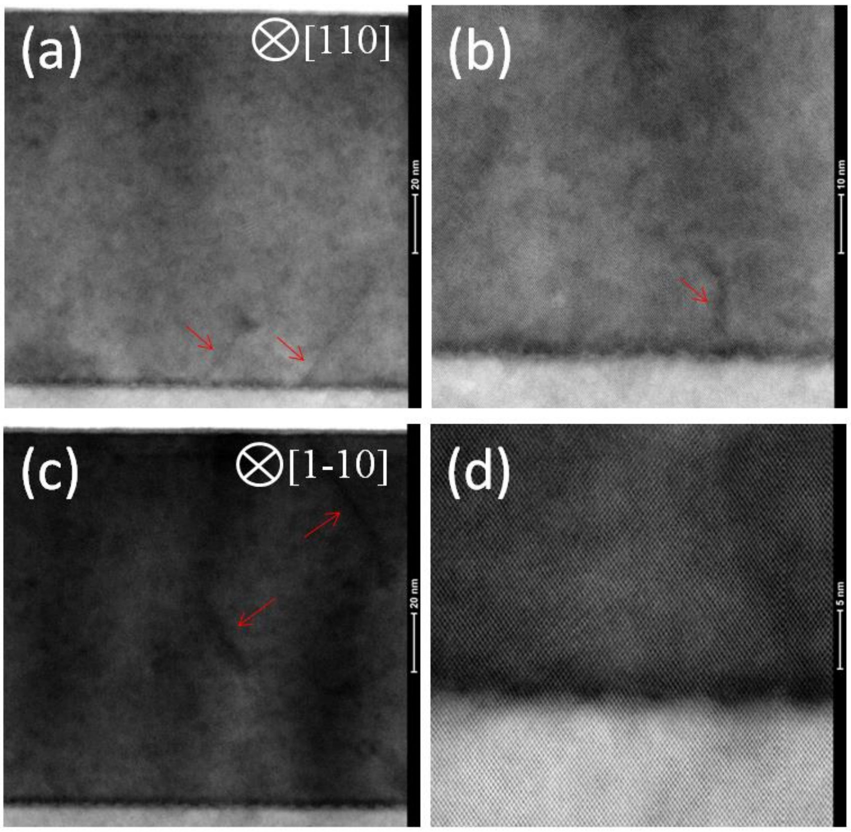

Figure IV.11. Bright field STEM images recorded in [110] (a-b) and [1-10] (c-d) directions and after atomic hydrogen assisted MBE growth of 150 nm GaSb with Sb/Ga = 2 followed by 10 nm InAs on a bare GaAs at 470°C. The threading dislocations are marked by red arrows.

Due to the limitation of displaying defects inside epilayer using a single STEM image, several dark field STEM (DF-STEM) observations has been performed for the cross-section along [110] and [1-10]-directions (figures IV.12). We notice a very strong contrast which allows determining the position of the defects in the GaSb layer. By examining the DF-STEM images for the cross-section along [110]-direction (figures IV.12(a)), we calculate a TDD of 11 x 10^4 cm^{-1} (1.2 x 10^{10} cm^{-2}). This latter is slightly more important along the [1-10] direction where it is about 15 x 10^4 cm^{-1} (2.2 x 10^{10} cm^{-2}) (figures IV.12(b)).

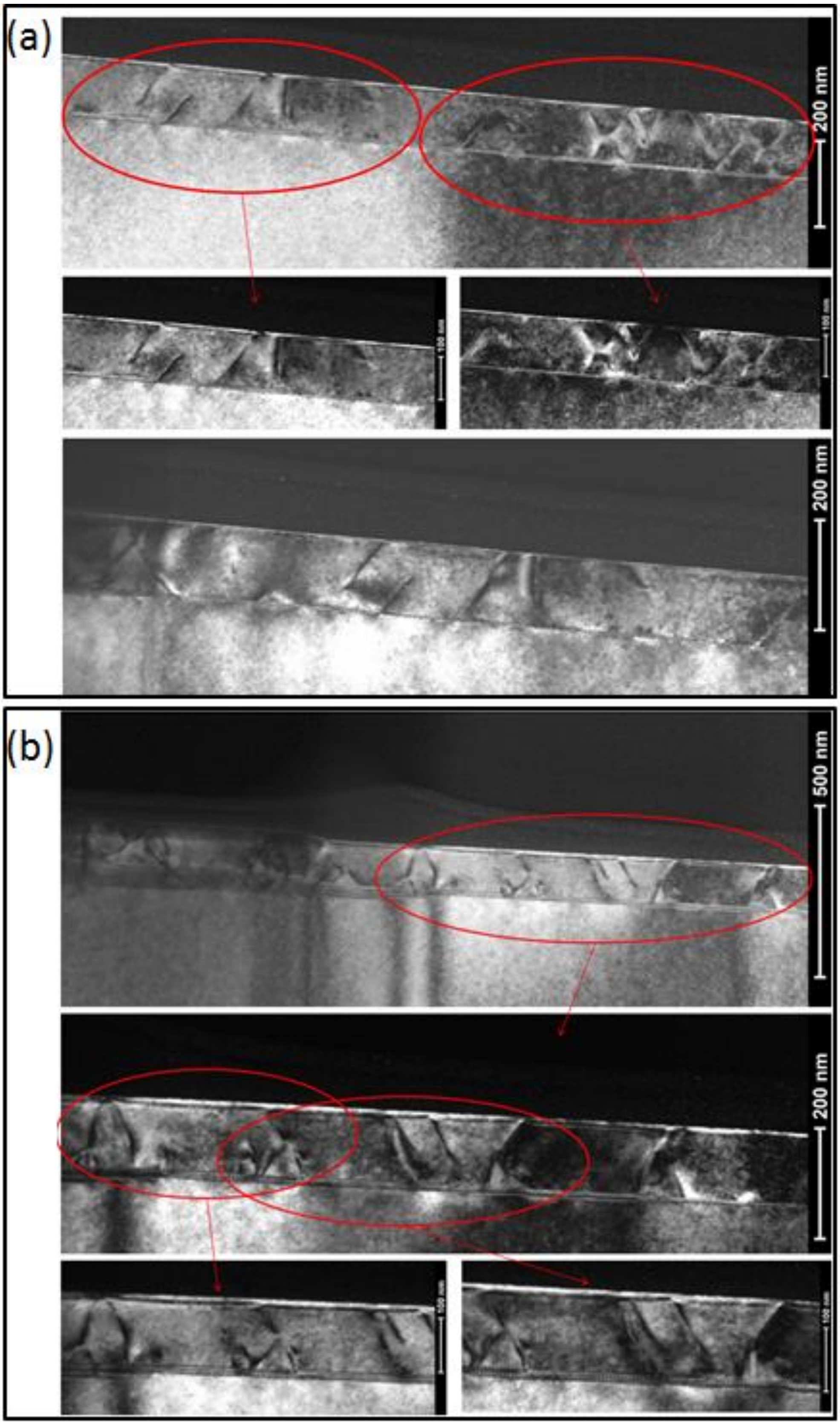

Figure IV.12. Dark field STEM images recorded in [110] (a) and [1-10] (b) directions and after atomic hydrogen assisted MBE growth of 150 nm GaSb with Sb/Ga = 2 followed by 10 nm InAs on a bare GaAs at 470°C.

b) XRD-analysis

Williamson-Hall model

As discussed in chapter II, assuming that the measured D-XRD spectra for a (hkl) reflection has a Gaussian shape, the square of the measured D-XRD FWHM, $\mathrm{B_m^2(hkl)}$, is given by [18]:

$$\mathrm{B_m^2(hkl) = B_i^2(hkl) + B_c^2(hkl) + B_r^2(hkl) + B_t^2(hkl) + B_d^2(hkl)} \qquad \text{(Eq.IV.2)}$$

where all the equation terms are defined in chapter II. Keeping the main terms in Eq.IV.2:

$$\mathrm{B_m^2(hkl) = B_r^2(hkl) + B_t^2(hkl) + B_d^2(hkl)} \qquad \text{(Eq.IV.3)}$$

The broadening due to the epilayer thickness ($\mathrm{B_t^2(hkl)}$) are determined with t = 150 nm and for different (hkl) reflections in table IV.3, together with the measured FWHM $\mathrm{B_m(hkl)}$ of the D-XRD spectra. Eq. IV.3 can then be transformed to:

$$\mathrm{B_m^2(hkl) - B_{150}^2(hkl) = B_r^2(hkl) + a.\tan^2(\theta)} \qquad \text{(Eq.IV.4)}$$

The dislocation density (D) may be determined from the rotational broadening as following [19]:

$$D = \frac{B_r^2(hkl)}{4.36\times b^2} \qquad \text{(Eq.IV.5)}$$

and from the strain broadening as following:

$$D = \frac{a}{0.09\times b^2 \times \left|\ln(2\times 10^{-7}\, cm\, \sqrt{D}\right|} \qquad \text{(Eq.IV.6)}$$

Table IV.3. The Ayers and Williamson-Hall model data for the 2D growth of 150 nm of GaSb on GaAs.

(hkl) Reflections	θ_B (°)	$\tan^2(\theta_B)$ (rad^2)	$\mathrm{B_{150}^2(hkl)}$ x 10^{-6} (rad^2)	$\mathrm{B_m^2(hkl)}$ x 10^{-6} (rad^2)		$[\mathrm{B_{150}^2(hkl) - B_m^2(hkl)}]$ x 10^{-6} (rad^2)	
				azimuth			
				[110]	[1-10]	[110]	[1-10]
(002)	14.6	0.07	0.99	5.96	8.77	4.96	7.77
(004)	30.4	0.34	1.25	7.31	0.11	6.06	9.48
(444)	62.2	3.28	3.98	0.11	0.15	7.23	9.63
(117)	65.5	4.38	5.01	0.18	0.21	13.1	16.5

Figure IV.13 presents the Ayers and Williamson-Hall plot in both [110] and [1-10] directions for the 2D growth of GaSb/GaAs. The linear fit along [110] has the following equation:

$$\mathrm{B}_{\mathrm{m}}^{2}(\mathrm{hkl}) - \mathrm{B}_{150}^{2}(\mathrm{hkl}) = \left(4.87 + 1.47 \times \tan^{2}(\theta)\right) \times 10^{-6} \qquad \text{(Eq.IV.7)}$$

Thus $\mathrm{B}_{\mathrm{r}}^{2}(\mathrm{hkl}) = 4.87 \times 10^{-6}$, which results in a TDD of 6.98 x 10^{8} cm^{-2}. Using the value of a = 1.47 x 10^{-6}, we obtain a TDD of 7.06 x 10^{8} cm^{-2}, which is in good agreement with the previous calculation.

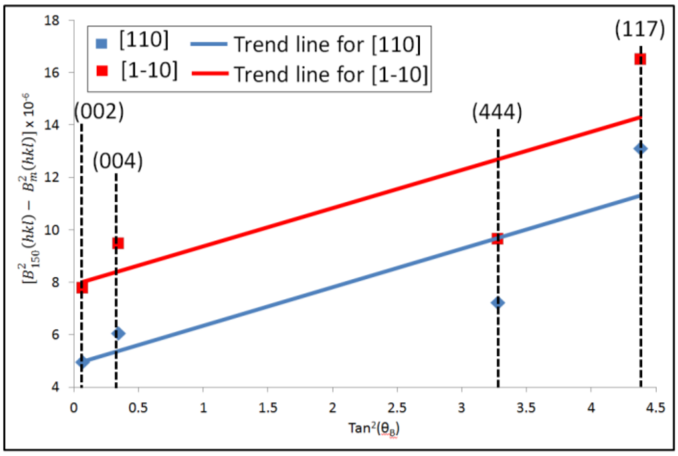

Figure IV.13. Ayers and Williamson-Hall plot in both diffracted planes [110] and [1-10] for the 2D growth of GaSb/GaAs.

The linear fit along [1-10] (figure IV.13) gives the following equation:

$$\mathrm{B}_{\mathrm{m}}^{2}(\mathrm{hkl}) - \mathrm{B}_{150}^{2}(\mathrm{hkl}) = \left(7.9 + 1.46 \times \tan^{2}(\theta)\right) \times 10^{-6} \qquad \text{(Eq.IV.8)}$$

Thus $\mathrm{B}_{\mathrm{r}}^{2}(\mathrm{hkl}) = 7.9 \times 10^{-6}$, and the TDD amounts to 11.32 x 10^{8} cm^{-2}. Using the value of a = 1.46 x 10^{-6}, we obtain a TDD of 7.01 x 10^{8} cm^{-2}, which is slightly lower than the previous calculation. This difference of a factor two or less between the $\mathrm{B}_{\mathrm{r}}^{2}(\mathrm{hkl})$ and the a calculations should be considered as an excellent agreement due to the approximated treatments in Eq.IV.1. By taking the mean value of the calculated TDD values we get 9.16 x 10^{8} cm^{-2} [19], which is rather close to the result for the [110] one. However, both values are largely smaller than those determined from the TEM images. This will be discussed in section 2.1.3 below.

Extended version of Williamson-Hall model

By means of the "Extended version of WHM", we qualify the structural quality of the GaSb epitaxial film, considering the following spectra [20]:

- (002), (004), (006), (117), and (444) D-XRD ω-scan
- (002) and (004) T-XRD ω-scan

- (002), (004), (006), and (444) T-XRD ω-2θ scan

Since the XRD-peaks have a Gaussian shape, the FWHM of GaSb peak can be easily determined. Actually, we apply the extended version of Williamson-Hall K-plot for the 60° and 90° dislocation types. Figure IV.14 displays the 60° and 90° K-plot for the 2D growth of GaSb/GaAs and for both [110] and [1-10] directions. For each K-plot we find the slope from the linear fit to calculate the linear density of 60° dislocations (ρ) or the correlation factor corresponding to the mean variation of the spacing between 90° dislocations (γ) (see chapter II). From the 60° dislocation K-plot and in both directions, we find a value of $\rho = 6.9 \times 10^4$ cm^{-1}. Assuming a regular network of 90° dislocations and using the 90° dislocation K-plot, we find a value of $\gamma = 5.7$ %.

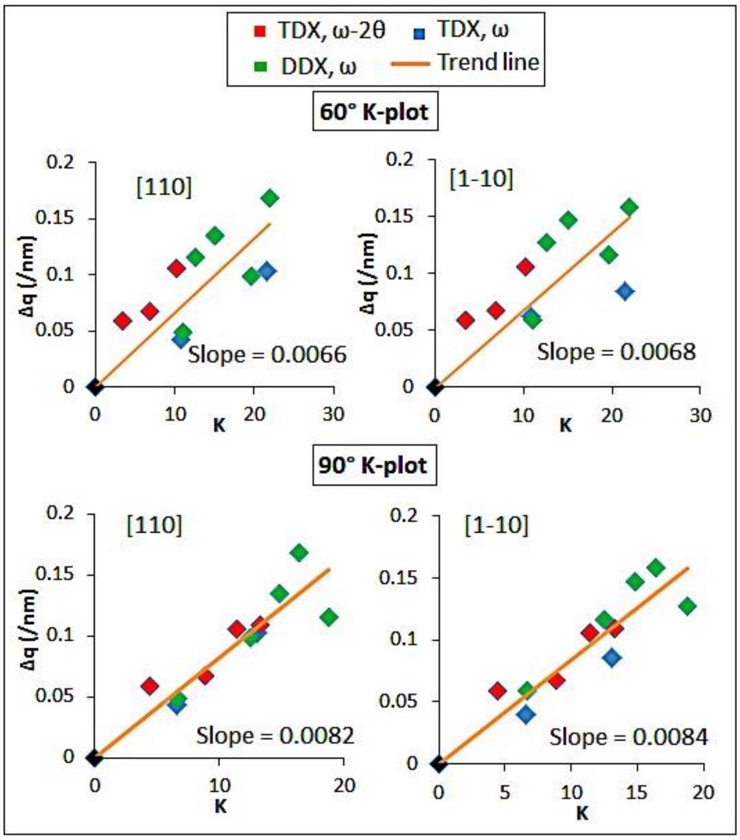

Figure IV.14. Extended version of Williamson-Hall plot using K values for 60° and 90° dislocations in both [110] and [1-10] directions for the 2D growth of GaSb/GaAs.

At this point, it is not obvious to choose between the Williamson-Hall and the extended version of Williamson-Hall models to interpret our XRD data. This will be further detailed in section 2.1.3 after the presentation of the results relative to the SAG in the following paragraph.

2.1.2. Selective area growth

a) STEM-analysis

Figure IV.15 presents the transverse STEM cross-section images of 10 nm InAs on the top of 65 or 150 nm GaSb for [110] and [1-10]-oriented stripes. As a first step, we will compare the GaSb crystal shape evolution with the deposited thickness for both stripe directions. For the [110]-oriented stripes, we notice that at 65 nm the shape exhibits lateral (111)B facets and a (001) facet at the top (figure IV.15(a)), whereas at 150 nm, (111)A facets appear at the GaSb/SiO_2 interface (figure IV.15(d)). For the [1-10]-oriented stripes at 65 nm, the GaSb nanocrystals have (110) and (111)A lateral facets and a top (001) one (figure IV.15(g)). By increasing the thickness, small (111)B facets appear at the GaSb/SiO_2 interface (figure IV.15(j)). Regarding the InAs deposition on GaSb nanotemplates in both directions, we notice that it is deposited mainly on the (001) GaSb facets. For the GaSb nanotemplates oriented along [110], InAs forms (111)B and (001) facets (figure IV.15(c and f)). However, for the GaSb nanotemplates oriented along [1-10], InAs forms a triangular shape having (113)A facets (figure IV.15(i and l)). Moreover by examining the interface between InAs and GaSb, TEM images clearly demonstrate the high crystal quality of InAs without any misfit dislocation at the GaSb/InAs interface (figure IV.15(c, f, i, and l)). This can be compared with recent reports on the growth of dislocation-free GaSb/InAs core-shell nanowires [17, 21]. High crystalline interface quality was achieved in these cases too but the heterostructures still suffer from polytypism with the presence of both zinc blende and wurtzite segments in the nanowires, which is not at all the case in our work.

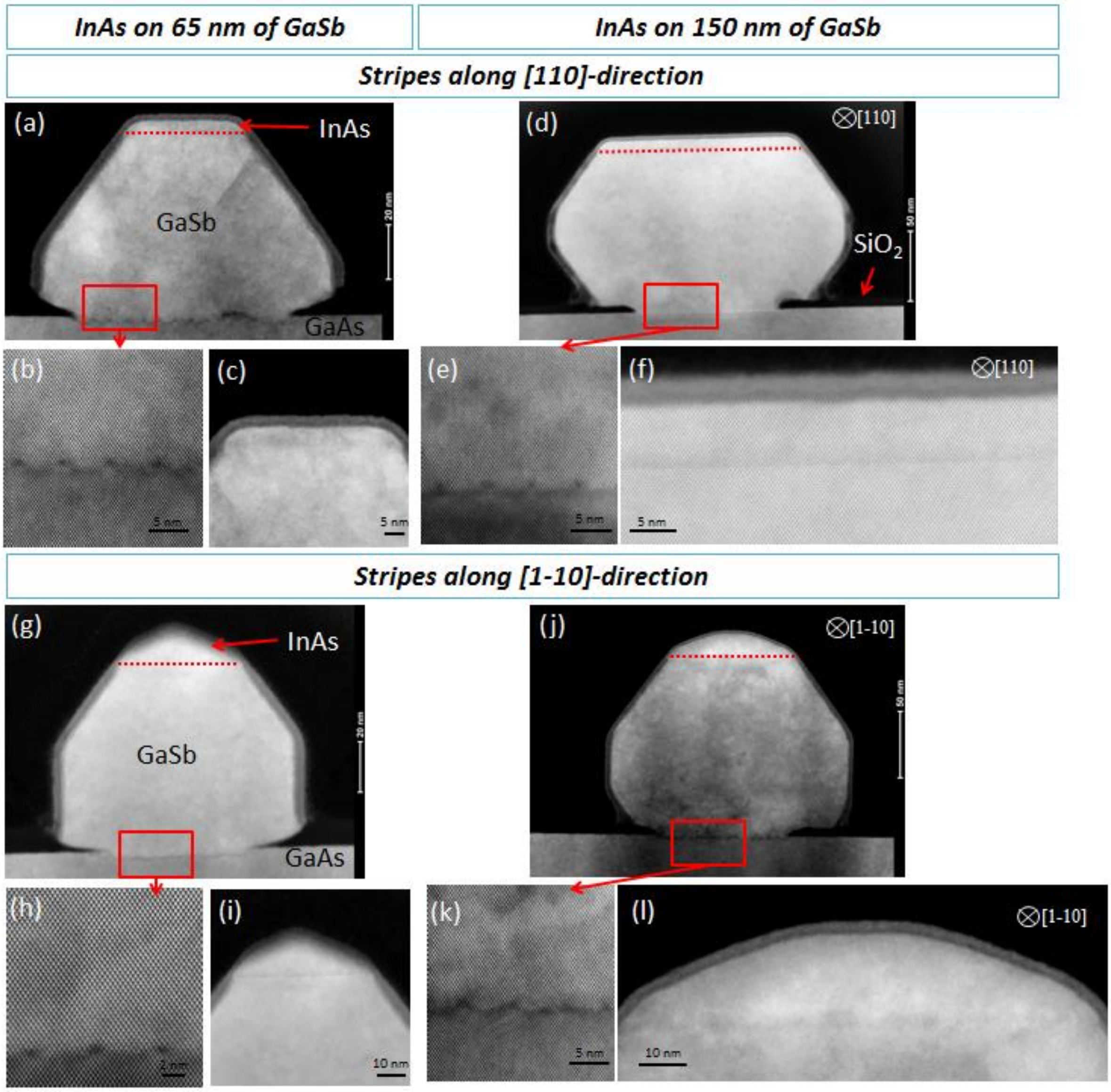

Figure IV.15. STEM images recorded after atomic hydrogen assisted MBE growth of 65 or 150 nm GaSb with Sb/Ga = 2 followed by 10 nm InAs at 470°C in apertures directed along [110] (a-f) and along [1-10] (g-l).

Let's now turn to the discussion of the interface between GaSb/GaAs for both stripe directions. The HAADF STEM images of the GaSb/GaAs interface for the transverse STEM cross-section of the [110] and [1-10]-oriented stripes (figure IV.15(b, e, h, and k) show that relaxation occurs mainly through a regular array of Lomer dislocations at the interface. To support the results shown by these images, ε_{xx} (along [100]) and ε_{yy} (along [1-10]) images are deduced from geometrical phase analysis (GPA) for the 65 nm GaSb sample (figure IV.16). It reveals that the lattice relaxation, for both stripes directions, is uniform both along the growth direction and in the growth plane. More they highlight the dislocation cores and allow measuring the distance between the dislocations, which is around 5.7 nm, a bit higher than the theoretical value of 5.5 nm for full relaxation of GaSb on GaAs. However, the above-mentioned value (5.7 nm) cannot be considered as a significant average since it has been obtained with only a few dislocations and therefore suffers from uncertainty, at least +/- 0.1 nm. The STEM observations of the Lomer dislocation spacing do not reveal any significant difference between both directions and between both GaSb deposited thickness.

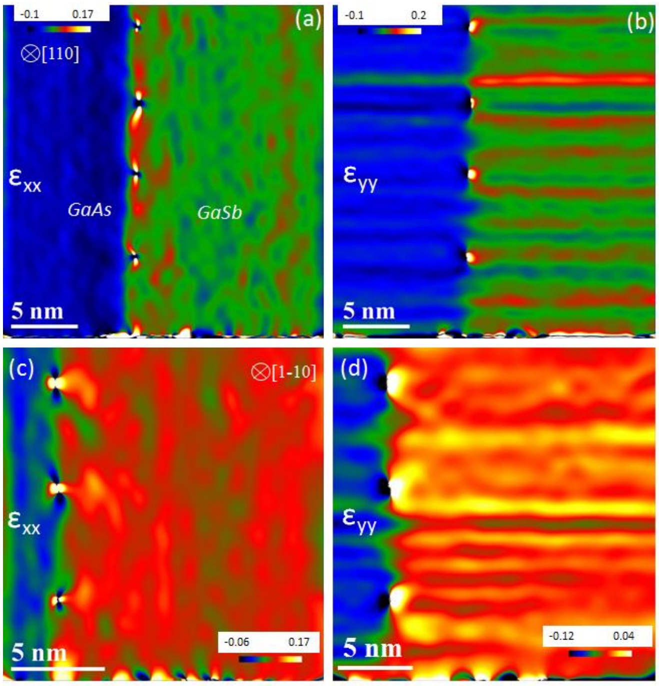

Figure IV.16. GPA analysis recorded after atomic hydrogen assisted MBE growth of 65 nm GaSb with Sb/Ga = 2 followed by 10 nm InAs at 470°C in apertures directed along [110] (a and b) and [1-10] (c and d). The determination of ε_{xx} (a and c) and ε_{yy} (b and d) through GPA analysis of figure IV.16b and h, respectively.

Examining the DF-STEM images for the longitudinal cross-section of the stripes directed along [110] (figures IV.17(a)) and [1-10] (figures IV.17(b)), we notice that the GaSb layer is relaxed through a Lomer dislocation network. Once again, the dislocation spacing is around 5.7 +/- 0.1 nm. Moreover, the GaSb nanotemplates are free from TDs and only contain stacking faults crossing the entire GaSb layer. The stacking fault density is about 3 x 10^4 cm^{-1} for the apertures along the [110]-direction and slightly lower (2 x 10^4 cm^{-1}) for apertures along the [1-10] direction.

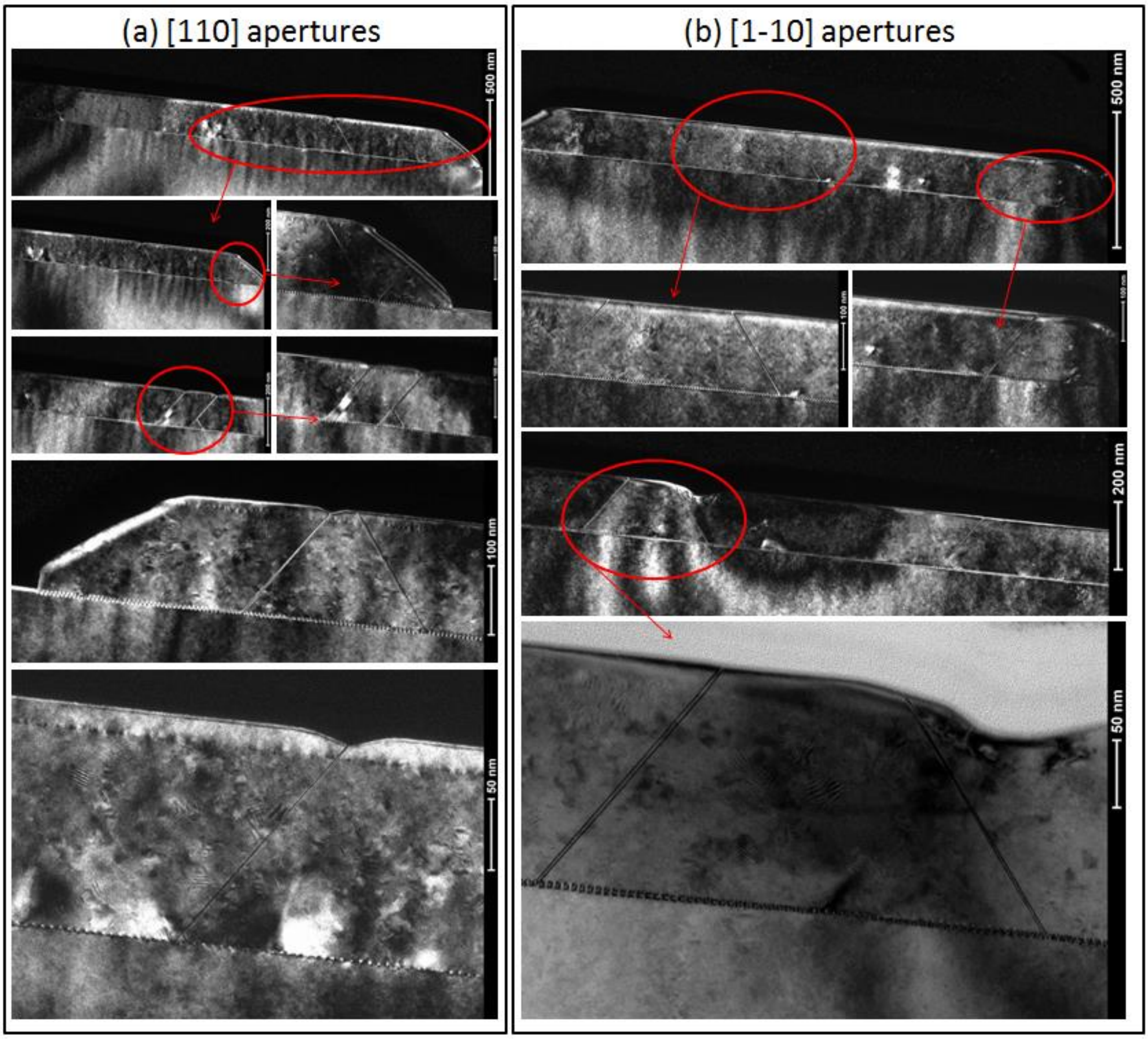

Figure IV.17. Dark field STEM images recorded along an InAs/GaSb nano-heterostructure grown by atomic hydrogen assisted MBE at 470°C in apertures directed along [110](a) and [1-10] (b) (150 nm GaSb with Sb/Ga=2 followed by 10 nm InAs).

b) XRD-analysis

InAs on 65 nm GaSb

The GaAs peak in (004) T-XRD ω-scan recorded for 65 nm GaSb inside [110] oriented stripes is presented in figure IV.18. We notice satellite peaks around the central peak, which are detected when the stripes are normal to the diffraction plane as presented in the inset of figure IV.18. The distance between two consecutive peaks (Δq) is related to a characteristic length L given by the following equation:

$$L = \frac{2.\pi}{\Delta q} \qquad \text{(Eq.IV.9)}$$

The measured value of Δq is about 0.02 nm which leads to L = 300 nm. This latter value corresponds to the pattern period (100+200) as depicted in the inset of figure IV.18.

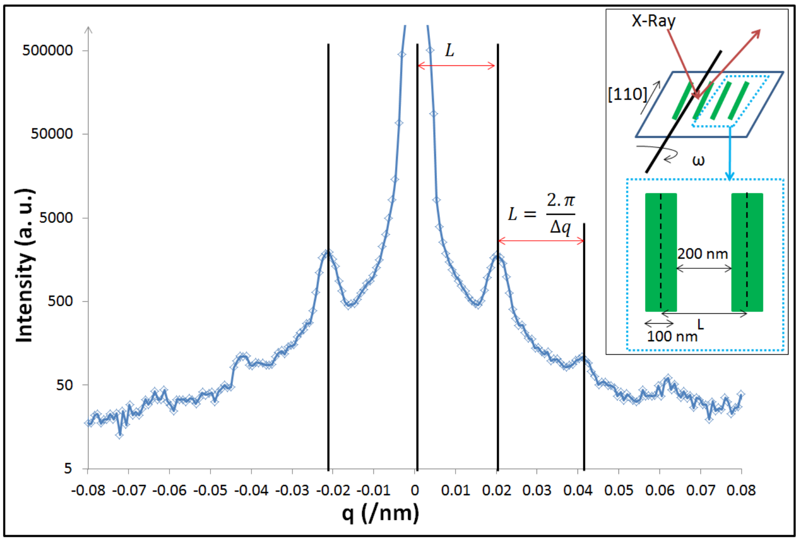

Figure IV.18. GaAs peak in (004) ω-scan T-XRD for 65 nm of GaSb stripes directed along [110] and deposited at 470°C with atomic H and a Sb/Ga flux ratio of 2. The inset represents the stripes position with respect to the X-Ray.

To get information about the GaSb crystal quality using the WHM or the "Extended version of WHM", XRD spectra in different geometries were recorded but most of them contain several peaks. For instance, Figure IV.19 presents the GaSb peak for (004) and (002) T-XRD ω-scans. Since the peaks are not purely Gaussian but exhibit several components, the FWHM cannot be extracted easily.

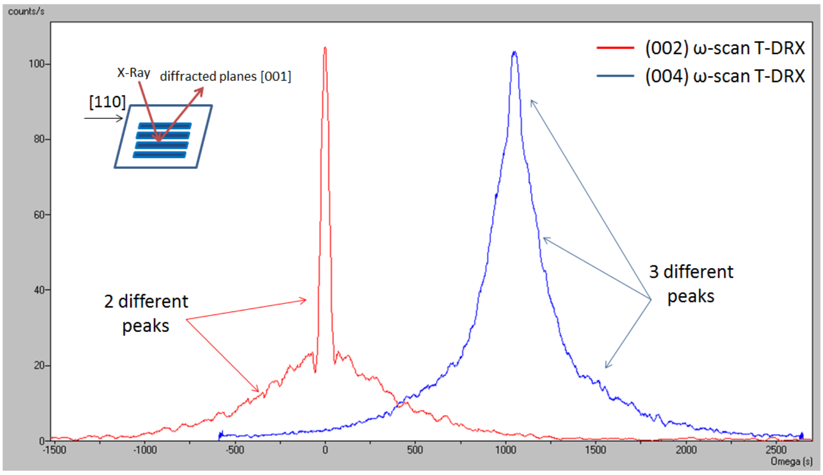

Figure IV.19. Typical (002) and (004) T-XRD ω-scan for 65 nm of GaSb stripes directed along [110] and deposited at 470°C with atomic H and a Sb/Ga flux ratio of 2. The inset represents the stripes position with respect to the X-Ray.

The same kind of peak shape was reported by Babkevich et al. [16]. They claimed that the FWHM of the sharp central peak is limited by the resolution of the XRD instrument. For this reason, XRD measurement has been performed on a perfect GaAs substrate. Figure IV.20 displays the associated (002) T-XRD ω-scan for the GaAs peak (red spectrum) together with the GaSb peak recorded for 65 nm GaSb stripes directed along [110] (blue spectrum). As evidenced by the inset of figure IV.20, the FWHM of the main peaks for the two samples are similar. Therefore, it may be concluded that the FWHM of the sharp central peaks seen on the XRD spectra in figure IV.19 are limited by the resolution of the XRD setup used in this work. Following Babkevich et al., this narrow peak could be related to constructive interferences between different stripes and reflects some long range coherency between the GaSb nanocrystals. After decomposition of the XRD peaks in different components, we have then tried to apply the WHM and extended WHM using the FWHM of the broad ones. However, the resulting plots cannot be interpreted properly, suggesting that the description of the peak broadening requires more sophisticated models in this case.

Babkevich et al. have also reported that due to an increase of the broad peak intensity with the layer thickness, the central sharp peak becomes progressively indistinguishable, leading to XRD peaks exhibiting an overall Gaussian shape. For this reason, in the next section we study the samples with a GaSb thickness of 150 nm to perform XRD analysis.

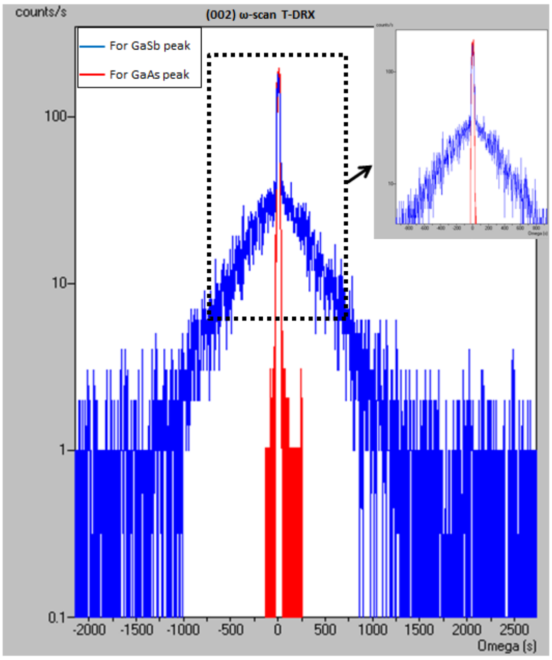

Figure IV.20. Typical (002) T-XRD ω-scan for 65 nm of GaSb stripes directed along [110] (blue spectrum) and for a perfect GaAs substrate (red spectrum). The inset represents a zoom for the central peaks.

InAs on 150 nm GaSb

The STEM images show that there is no TDs inside the GaSb nanowires. Accordingly, the WHM cannot be applied on these stripes. However, the "Extended version of WHM" can be performed in order to qualify the structural quality of the GaSb epitaxial film. To do that, the following spectra were selected:

- (002), (004) and (444) D-XRD ω-scan
- (004) T-XRD ω-scan
- (002), (004) and (444) T-XRD ω-2θ scan

Figures IV.21(a and b) represent typical XRD spectra for GaSb peak in D-XRD and for T-XRD ω-2θ respectively. We notice that the XRD peaks exhibit a Gaussian shape. Consequently, the FWHM can be easily determined. Since the InAs peak is weak in the T-XRD ω-2θ scan (figure IV.21(b)), we will focus on the GaSb peak to study GaSb structural quality in the opening. The XRD measurement configuration is presented in the inset of figure IV.21(a)

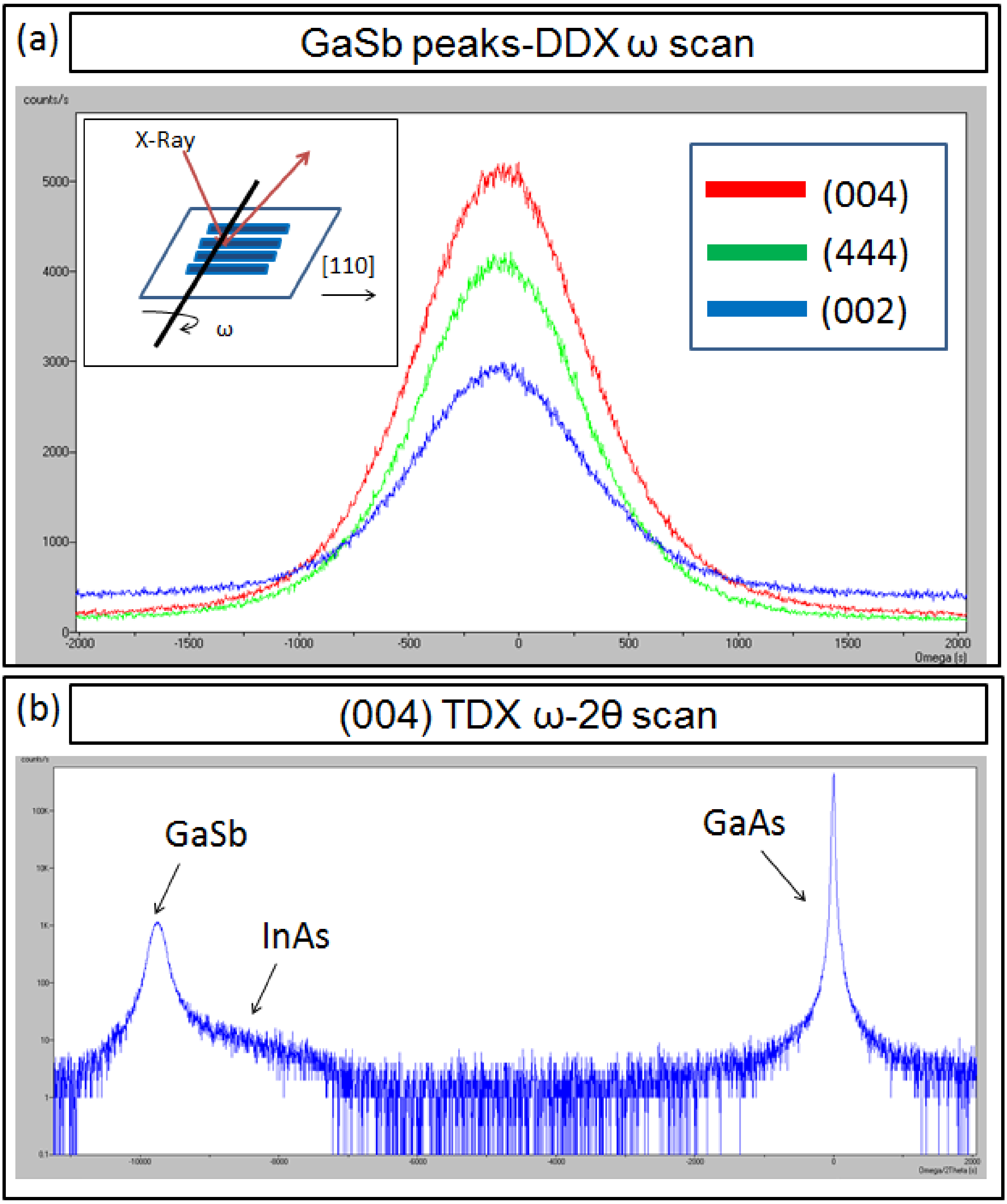

Figure IV.21. Typical XRD spectra for 150 nm of GaSb deposited inside the apertures directed along [110]. (002), (444) and (004) D-XRD ω-scan (a) and (004) T-XRD ω-2θ scan (b). The inset in figure (a) represents the stripes positions with respect to the X-Ray.

Actually, we apply the extended version of Williamson-Hall K-plot for the 60° and 90° dislocation types. Figures IV.22(a and b) display the 60° and 90° K-plot for the apertures directed along [110] and [1-10] respectively. For each K-plot we find the slope from the linear fit in order to calculate the linear density of 60° dislocations (ρ) and the correlation factor corresponding to the mean variation of the spacing between 90° dislocations (γ) (see chapter II).

For the stripes oriented along [110]-direction and from the 60° dislocation K-plot, we find a value of $\rho = 9.8 \times 10^4$ cm^{-1}. Assuming a regular network of 90° dislocations and using the 90° dislocation K-plot, we find a value of $\gamma = 7.5$ %. For the stripes oriented along [1-10]-direction, we find a lower value of $\rho = 6.7 \times 10^4$ cm^{-1} and $\gamma = 5.6$ %.

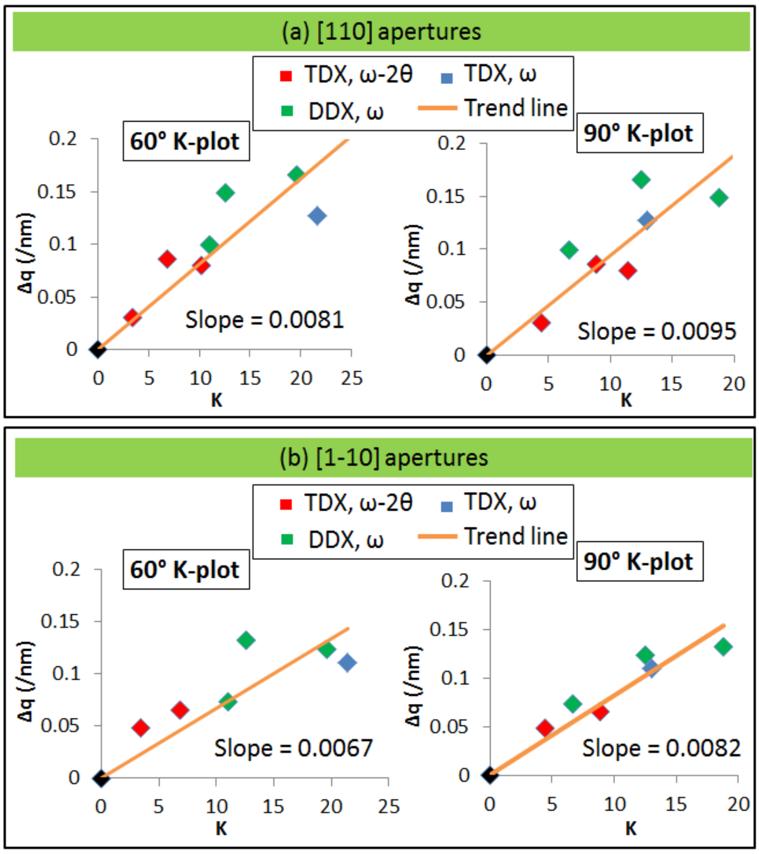

Figure IV.22. Extended version of Williamson-Hall plot using K values for 60° and 90° dislocations for the apertures directed along [110] (a) and [1-10] (b), using the configuration presented in the inset of figure IV.21(a).

2.1.3. Discussion

Comparing the GaSb quality for the 2D and the selective growth, we notice that using the SAG approach we get TD free GaSb nanowires. This is the benefit of growing in small openings for which, upon gliding, TDs easily reach the nanocrystal edges. However, some twins are detected inside the selectively grown GaSb. May be it is due to the coalescence of the islands which are formed inside the openings or it can be due to a growth on the faceting of these islands before it coalesce.

We first compare the STEM and WHM results. Since the 2D growth presents TDs in the GaSb layer, we apply the WHM on this sample in order to quantify the TDD. The TDD values obtained using the WHM are much lower than those deduced from the STEM images. To explain this difference we present in table IV.4 the FWHM of the GaSb peak for different reflections obtained for 2D and selective growths. We notice that the values of the FWHM for the 2D growth are slightly lower than that of selective growths. This means that the broadening of the GaSb peak cannot be ascribed to the TDs since the GaSb nanostructures inside openings are free from TDs (see STEM images). Therefore, the broadening appears mainly related to the MDs at the interface as proposed by the extended version of WHM. Nevertheless, in the case selective growth, we cannot exclude some broadening contribution from the stacking faults.

Table IV.4. Data of the FWHM of GaSb peak from XRD scans for the 2D and selective growths of 150 nm of GaSb on GaAs.

ω-scan in		D-XRD			T-XRD
Reflections		(002)	(004)	(444)	(004)
Samples		Δq (/nm)			
2D	110	0.04869	0.09878	0.11559	0.08445
	1-10	0.05907	0.11653	0.12734	0.10134
[110] apertures		0.09939	0.16599	0.14897	0.12729
[1-10] apertures		0.07351	0.12387	0.13251	0.11071

Let us now try to correlate the STEM results with the extended version of WHM. It is not easy because the mean variation of the spacing between 90° dislocations determined from the STEM images involves only few dislocations. To do so we use the GPA analysis recorded for the longitudinal cross-section of the stripes along [110]-direction (Figure IV.23) and measure the spacing between the 90° dislocations. The mean variation of the spacing between 90° dislocations calculated from the GPA analysis is about 10 %. This later is close to the one found by the extended version of WHM which is 7.5%.

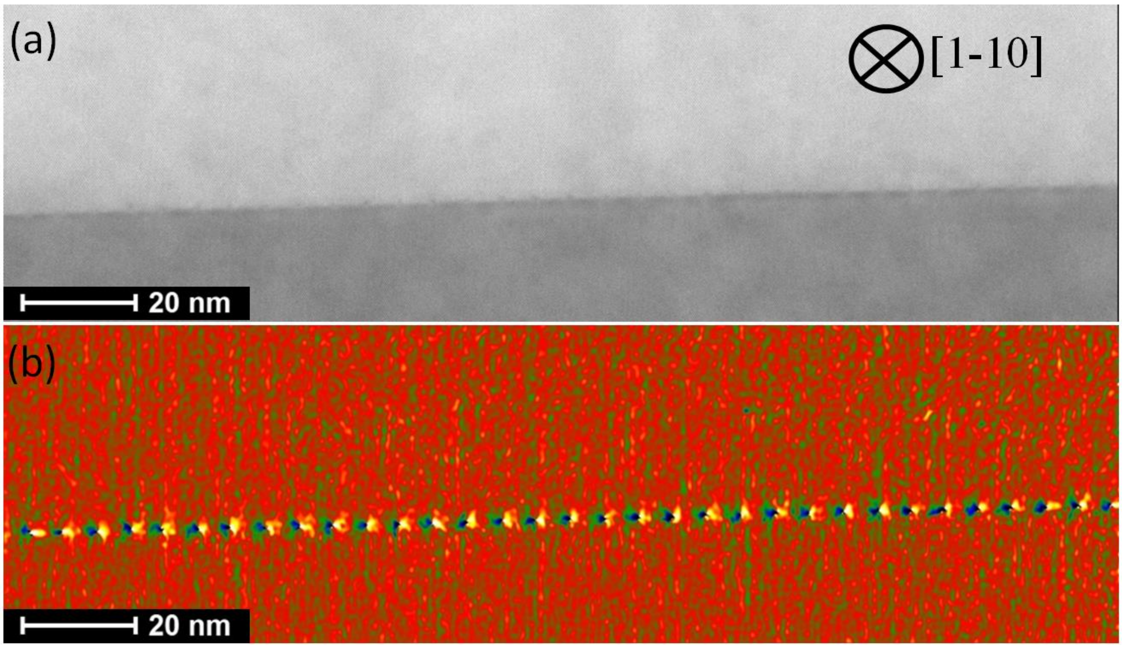

Figure IV.23. Determination of R_{xy} *(b) through GPA analysis of HAADF STEM image (a) recorded after atomic hydrogen assisted MBE growth of 150 nm GaSb with Sb/Ga = 2 followed by 10 nm InAs at 470°C in apertures directed along [110].*

Finally, within the extended version of WHM, comparing the 2D growth and the selective one, it comes out that the results for the [1-10] direction are very similar whereas for the [110] one, they are better for the 2D growth (Table IV.5). It might be related to the slight difference in the stacking fault density between the two directions mentioned above (Figure IV.17).

Table IV.5. The density of 60° dislocations (ρ) and the mean variation of the spacing between 90° dislocations (γ) calculated for the 2D and selective growths of 150 nm of GaSb on GaAs.

Samples	ρ (x 10^4 cm^{-1})	γ (%)
2D	6.9	5.7
[110] apertures	9.8	7.5
[1-10] apertures	6.7	5.6

2.2. Chemical analysis

Firstly, we present the EDX analysis obtained for the 2D growths. Figures IV.24(a-d) and 24(e-h) display the ones of the STEM images presented in figures IV.11(a) and (b) respectively. These EDX analyses show the composition of the deposited layers in both directions with no major difference between the two directions.

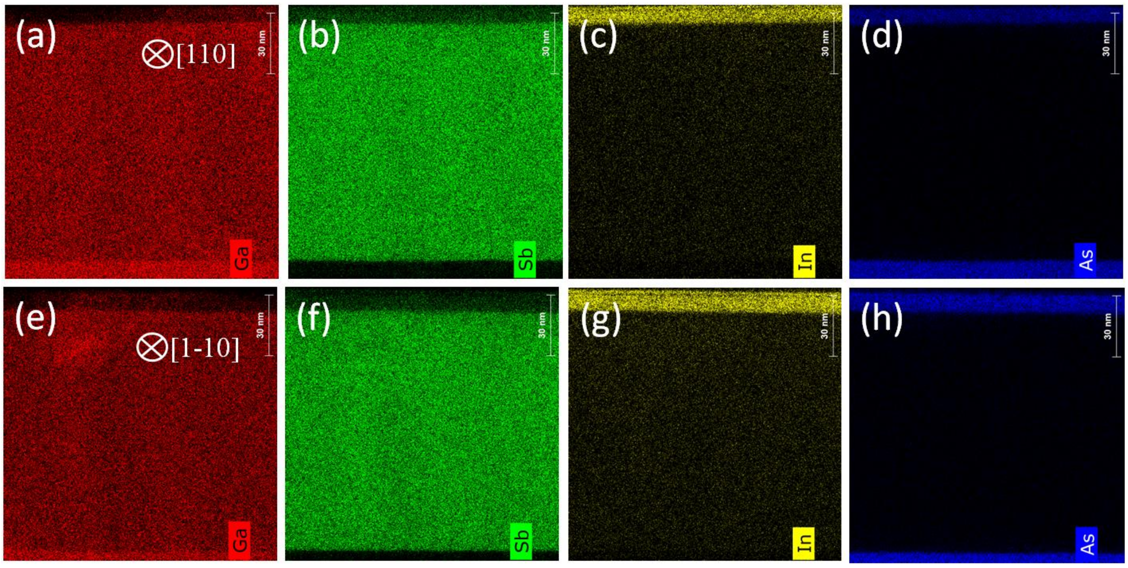

Figure IV.24. EDX images recorded in [110](a-d) and [1-10] (e-f) directions and after atomic hydrogen assisted MBE growth of 150 nm GaSb with Sb/Ga = 2 followed by 10 nm InAs on a bare GaAs at 470°C.

HAADF images and EDX analysis of transverse cross-section for [110] and [1-10]-oriented stripes for both GaSb thicknesses are displayed in figures IV.25, respectively. For the stripes oriented along [110], InAs growth occurs mainly on top of GaSb with only minor In deposition on the (111)B facets (figure IV.25A(d and i)). Similarly for the stripes along [1-10], InAs growth occurs on top of GaSb by forming a (113)A facets. However, Sb and Ga are also detected in the upper InAs part with decreasing concentrations from the GaSb/InAs interface to the top. Quantitatively, this amounts to roughly 15% Sb and 20% Ga in InAs, as quantified by the concentration profile recorded along the growth direction through the nanostructure for [1-10]-oriented stripes (figure IV.25B(a)). Figure IV.25(k) reveals the oxidization of the nanostructure facets, which is more pronounced on the GaSb lower part than on the InAs upper part.

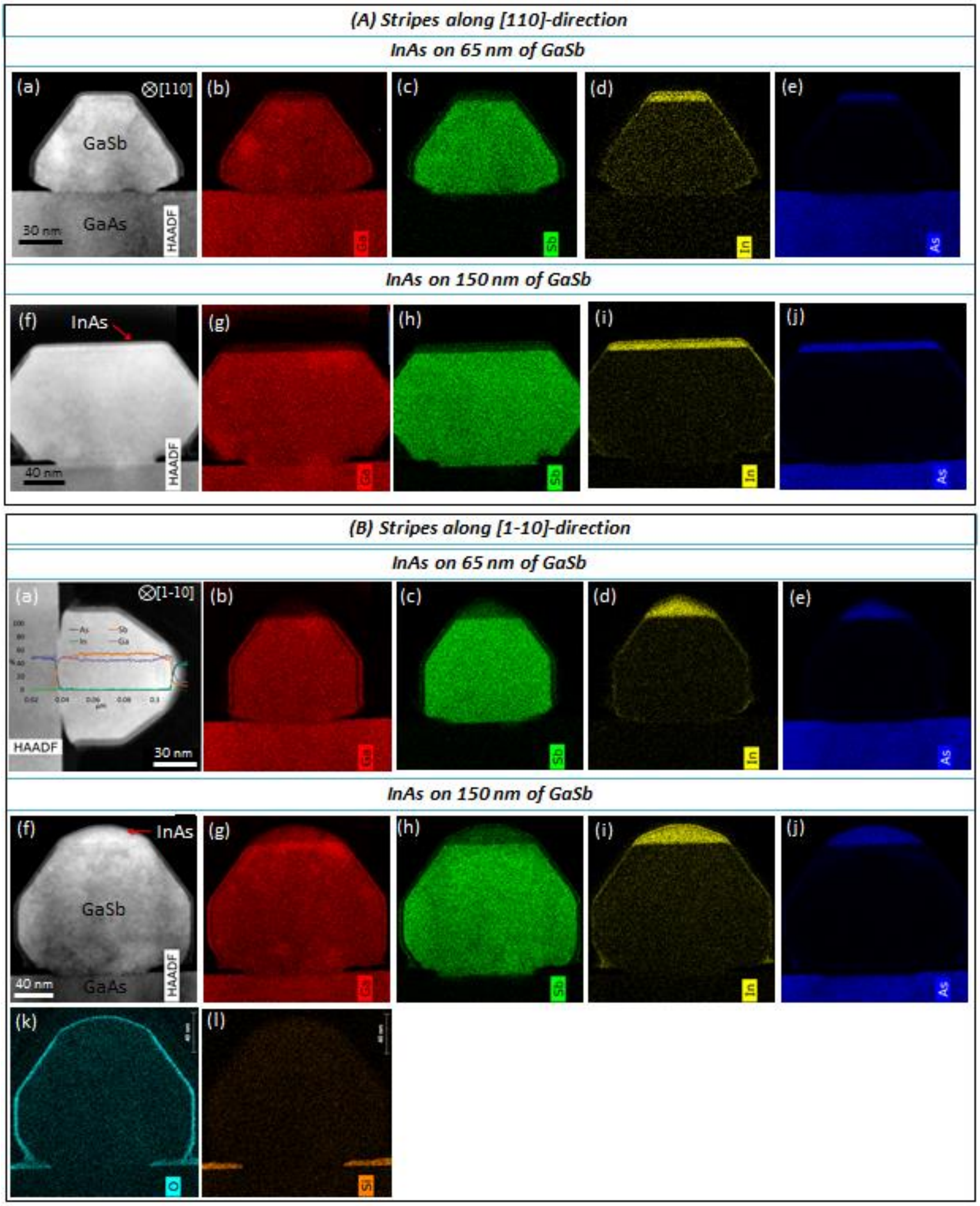

Figure IV.25. HAADF images (a and f) and EDX analysis (b-f and g-j) obtained after atomic hydrogen assisted MBE growth of 65or 150 nm GaSb with Sb/Ga=2 followed by 10 nm InAs at 470°C in apertures directed along [110](A) and [1-10] (B). The scale for the EDX images are represented on the corresponding HAADF images.

Figure IV.26 presents the HAADF images and EDX analysis of the longitudinal cross-section for the stripes directed along [110]-direction. The HAADF images show the high structural quality of the InAs/GaSb nanostructures (no noticeable defect). The same result is obtained for the longitudinal cross-section for the stripes directed along [1-10]-direction.

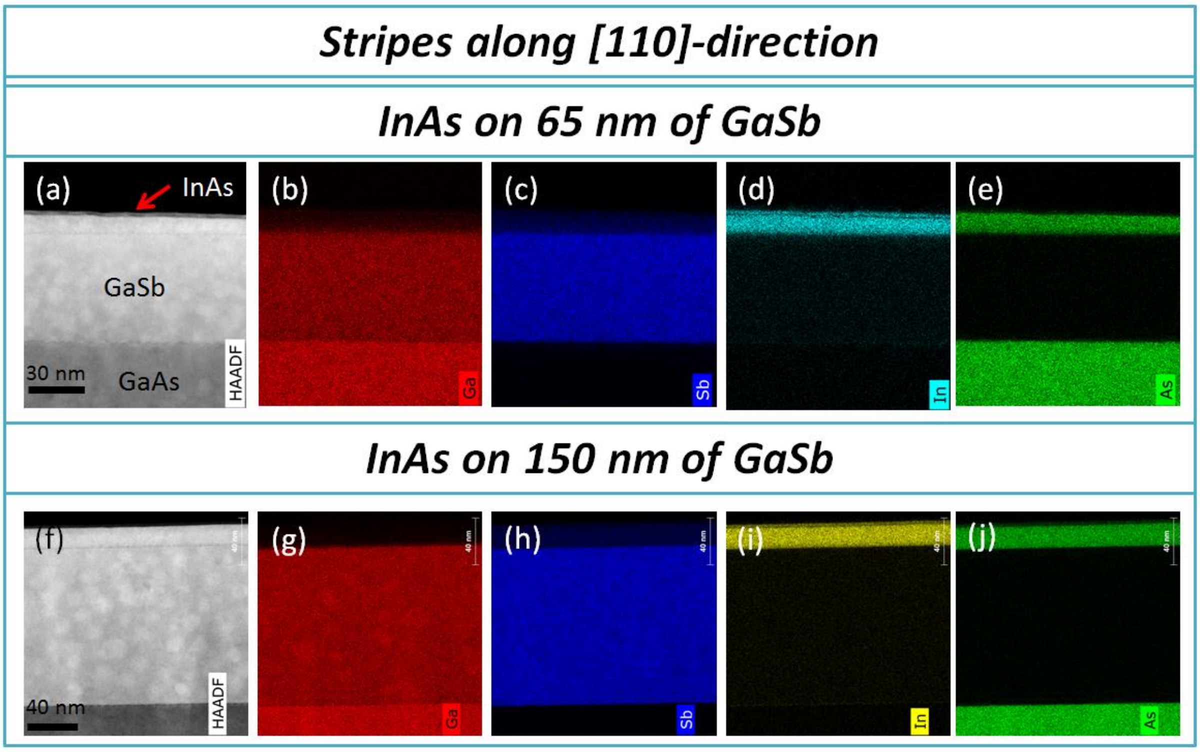

Figure IV.26. HAADF images (a and f) and EDX analysis (b-f and g-j) obtained after atomic hydrogen assisted MBE growth of 65 or 150 nm GaSb with Sb/Ga=2 followed by 10 nm InAs at 470°C in longitudinal cross-section of the apertures directed along [110]. The scale for the EDX images are represented on the corresponding HAADF images.

As evidenced by EDX data some intermixing occurs in the InAs top layer. Sb segregation is a well-known phenomenon [22], probably enhanced in our growth conditions using a relatively low growth rate. Ga segregation/interdiffusion in InAs is less expected and further work is needed to clarify this point. This may be related to the desorption of some residual Ga and Sb atoms from the mask. In this case, a growth interruption after GaSb selective epitaxy should allow this desorption to occur before InAs growth. Nevertheless, only a very small amount of InAs is deposited on the (111) and (110) GaSb facets. One first basic reason for this is purely geometric since the mean molecular flux is different for each facet of the nanostructure due to the angle between the crucibles and the rotating sample (about 40°). An other piece of explanation could be the passivation of (111)B facets by As trimmers at high As/In ratio impeding the growth on these facets for [110] oriented lines [23]. However, these arguments are probably not sufficient to explain the observed thickness difference between the facets, which may also, involves some surface energy minimization. Anyway, this clearly demonstrates that the present approach can be used to grow InAs nanowires with typical dimensions far smaller than the lithographically defined ones.

More, thanks to the selective etching of GaSb versus InAs using dilute ammonia-based solution (10%), InAs nanowires can be released as illustrated in figure IV.27 showing a GaSb/InAs nanostructure after ammonia etching and just before complete lift-off of InAs.

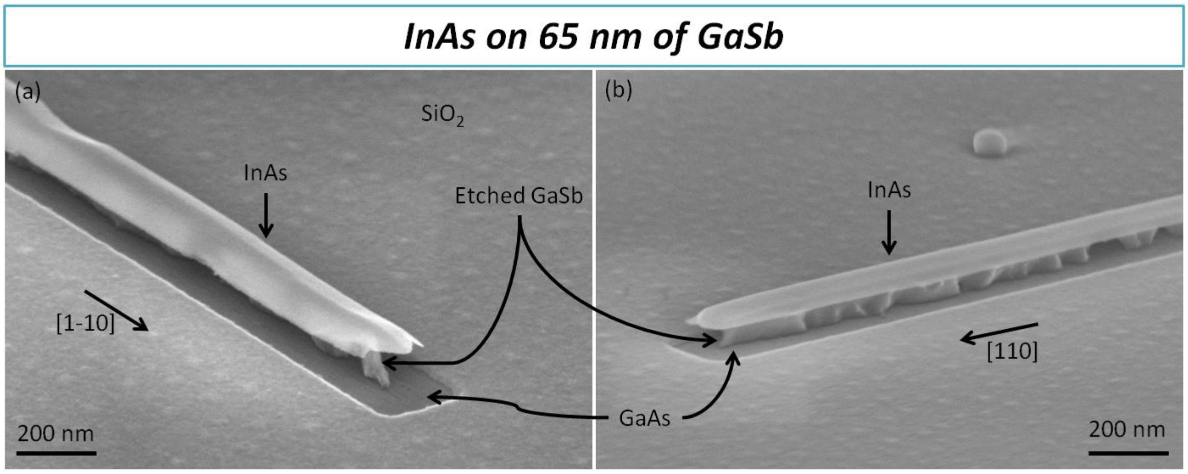

Figure IV.27. Freestanding InAs nanowire obtained after GaSb wet selective etching of an InAs/GaSb nano-heterostructure grown along [1-10] (a) and [110] (b).

In order to impede the complete lift-off of InAs nanowires, a specific pattern was carry out, i.e. to preserve the InAs nanowires maintained on the substrate. Figure IV.28(A) shows a schematic representation of the plan and sectional view of this pattern. This latter consists in two squares (10*10 μm^2) connected by several lines of 500 nm long and 100 nm wide. Here, we present the SEM plan and cross-section view images for 10 nm of InAs grown on 150 nm of GaSb where the stripes are oriented along [110]-direction (figure IV.28(B)). We achieve the realization of freestanding InAs nanowires but we notice that we still have a slight deposition of InAs on the (111) facets of GaSb. To improve the InAs nanowire release, a supercritical drying can be established.

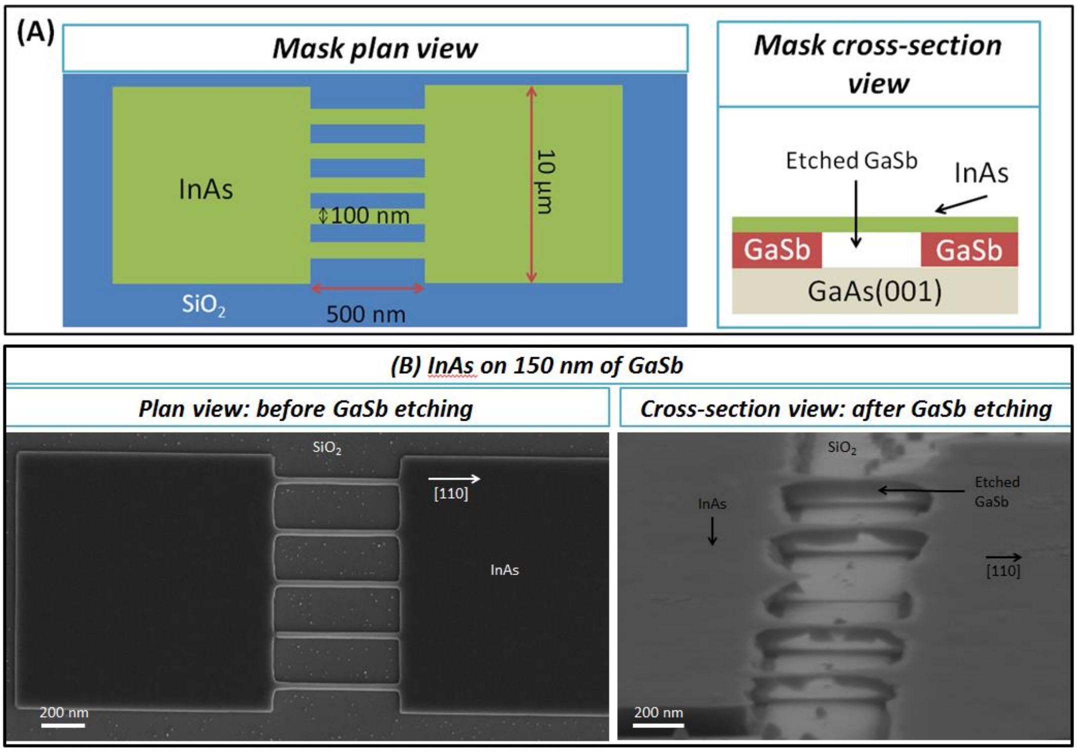

Figure IV.28. Schematic representation for the pattern used to get freestanding InAs nanowires (A). SEM plan view of InAs/GaSb nano-heterostructure grown along [110] before GaSb wet selective etching (a) and their cross-section view after GaSb etching where freestanding InAs nanowire are obtained (b).

3. General conclusion

We have shown that the morphology and strain relaxation of GaSb nanostructures selectively grown inside 100 nm wide stripes by MBE on a GaAs substrate can be influenced by the growth temperature, the presence of atomic hydrogen during the growth, and the Sb/Ga flux ratio. A rather low growth temperature (470°C) improves the GaSb nanocrystal morphology at the expense of growth selectivity. At the same growth temperature, this latter can be improved by the use of an atomic hydrogen flux which preserves the nanostructure morphology. We also show that a reduced Sb/Ga flux ratio enhances the GaSb relaxation within the stripes, leading to nearly perfectly relaxed material.

In these optimized conditions, STEM observations and XRD measurements confirm the high structural quality of the grown GaSb nanostructures. We achieve TD free GaSb nanostructures, whereas this is not the case for a 2D GaSb layer. We then use the obtained GaSb nanostructures as a template for the growth of a 10 nm thick InAs layer. High resolution EDX analysis demonstrates that InAs mainly grows on top of GaSb, which upon subsequent selective wet chemical etching, releases freestanding InAs nanowires.

References

1. C. Jiang, H. Sakaki, Physica E **32**, 17, 2006.

2. M. Ohtsuka, J. Cryst. Growth **205**, 112, 1999.

3. A. Khatiri, J. Ripalda, T. Krzyzewski, G. Bell, C. McConville, and T. Jones, Surf. Sci. **548**, 1–3, L1–L6, 2004.

4. N. Yamamoto, N. Kondo, and Y. Nanishi et al, J. Cryst. Growth **96**, 705, 1989.

5. T. Sugaya, Y. Okada, and M. Kawabe, Jpn. J. Appl. Phys. **31**, 2, 6A, L713–L716, 1992.

6. N. Kuroda, S. Sugou, T. Sasaki, and M. Kitamura, Jpn. J. Appl. Phys. **32**, 2, 11A, L1627–L1630, 1993.

7. D. R. Lide, CRC handbook of chemistry and physics. CRC press, 2004.

8. R. Kobayashi, K. Fujii, and F. Hasegawa, Jpn. J. Appl. Phys. **30**, 2, 8B, L1447–L1449, 1991.

9. A. Y. Babkevich, R. A. Cowley, N. J. Mason, S. Weller, and A. Stunault, J. Phys. Condens. Matter **14**, 49, 13505, 2002.

10. R. Z. Bachrach and R. D. Bringans, J. Vac. Sci. Technol. B **1**, 2, 142–145, 1983.

11. N. Moll, A. Kley, E. Pehlke, and M. Scheffler, Phys. Rev. B **54**, 12, 8844, 1996.

12. N. Moll, M. Scheffler, and E. Pehlke, ArXiv Prepr. Cond-Mat 9807200, 1998.

13. Q. K. K. Liu, N. Moll, M. Scheffler, and E. Pehlke, Phys. Rev. B **60**, 24, 17008, 1999.

14. B. Paulus, P. Fulde, and H. Stoll, Phys. Rev. B **54**, 4, 2556–2560, 1996.

15. S. E. Kazzi, L. Desplanque, X. Wallart, Y. Wang, and P. Ruterana, J. Appl. Phys. **111**, 12, 123506, 2012.

16. A. Y. Babkevich, R. A. Cowley, N. J. Mason, S. Weller, A. Stunault, J. Phys. Condens. Matter **14**, 13505, 2002.

17. M.S. Abrahams, C.J. Buiocchi, J. Appl. Phys. **37**, 1973, 1966.

18. M. J. Hordon and B. L. Averbach, Acta. Meta. **9**, 1961.

19. J.E. Ayers, J. Crys. Growth **135**, 71-77, 1994.

20. V. M. Kaganer, R. Kohler, M. Schmidbauer, and R. Opitz, Phys. Rev. B **55**, 3, 1997.

21. X. Ji, X. Yang, W. Du, H. Pan, S. Luo, H. Ji, H. Q. Xu, T. Yang, Nanotechnology **27**, 275601, 2016.

22. X. Wallart, S. Godey, Y. Douvry, L. Desplanque, Appl. Phys. Lett. **93**, 123119, 2008.

23. K. Tomioka, P. Mohan, J. Noborisaka, S. Hara, J. Motohisa, T. Fukui, J. Cryst. Growth **298**, 644, 2007.

Conclusions and perspectives

This thesis reports very promising results for the selective area growth (SAG) of III-V semiconductor nanostructures on III-V (001) substrates by molecular beam epitaxy (MBE). After presenting the interests of III-V nanostructures for microelectronics in chapter I, we study the SAG approach in order to control nanostructure shape and crystalline quality. The main conclusions, obtained in the framework of this thesis, are summarized below.

Through a detailed study of the selective homoepitaxy of InAs and InP, we analyze the nanostructure evolution for these two materials when varying the V/III flux ratio, the opening width and the stripe orientation. For the SAG of InP, it comes out that the interface surface energy between InP and the mask is low, in such a way that it does not strongly influence the lateral overgrowth of the nanostructures. Once lateral overgrowth has occurred, the nanocrystal evolves as a free one. This InP-nanocrystal behavior allows applying the equilibrium crystal shape (ECS) model for interpreting the obtained shapes [1-2]. The chemical potential as well as the facet surface energies can be then determined for defined growth conditions. By playing on these latter (i.e. varying the chemical potential), we demonstrate that the crystal shape can be tailored. However, for the SAG of InAs and due to the high interface energy between InAs and the mask, no lateral overgrowth of the nanostructures is detected. In this case the ECS model cannot be applied. Actually, since the InAs nanostructures are blocked by the mask, a migration of InAs from the (110) facets to the (001) ones occurs and results in a variation of the chemical potential as well as the facet surface energies during the growth. Therefore, in the case of SAG of InAs it is more complicated to predict the crystal shape evolution when varying the growth conditions. Moreover, two important features have been showed for InAs and InP growth systems. The first one is that the shape evolution when the growth proceeds can be determined by calculating the ratio of the experimental thickness over the opening width. The second feature is that, when the nanostructure thickness becomes important, either a lateral overgrowth or growth on the (111) facets occurs, leading to some crystalline defects.

This manuscript also details the selective heteroepitaxy of highly mismatched GaSb on GaAs(001). We demonstrate that a low growth temperature improves the GaSb nanocrystal morphology but causes a lot of polycrystalline GaSb deposition on the mask. We have shown that an atomic hydrogen flux during the growth can be used to get rid of the polycrystalline GaSb deposited on the mask at low temperature without affecting the nanostructure morphology. Moreover, the effect of Sb/Ga flux ratio has been investigated, demonstrating that a reduced value of Sb/Ga flux ratio enhances the nanostructure length within the stripes in [1-10]-direction and the GaSb relaxation for the ones oriented along [110]-direction. It may be due to anisotropic diffusion length of Ga adatoms and GaSb relaxation between the stripe directions. By means of transmission electron microscopy, we show that SAG greatly improves GaSb crystalline quality. Indeed, selectively grown GaSb, although containing some stacking faults is free from TD, while the TD density in GaSb 2D layer is very important. These high-quality GaSb nanotemplates have then been used to grow in-plane InAs nanowires with high structural quality. This demonstration is very promising for the integration of in-plane InAs nanowires on Si substrate for the next generation of gate all-around transistors working at low supply voltage.

Besides this applied goal, this work also provides perspectives for future studies. First of all, the role of lattice mismatch on the nanostructure faceting remains to be investigated experimentally. Indeed, the effect of strain has been described theoretically for pseudomorphic nanostructures [3, 4] but not for plastically relaxed ones.

For these material systems, further work could also focus on what happens at the island coalescence during 2D or selective growth. For instance, is the formation of stacking faults and twin defects observed in the nanostructures related to this coalescence step? A detailed investigation of this process inside openings for different layer thicknesses and aperture widths has to be considered. This kind of study might help understanding some rather unexpected behavior we have observed during the SAG of GaSb on GaAs inside stripes oriented along [1-10]-direction: an increasing number of clippings when the stripe width decreases. The SEM images recorded for 25 nm GaSb on GaAs inside the stripes along [1-10]-direction and for several opening widths are displayed in the figure below. This phenomenon has also been observed for the SAG of SiGe [5] and Si [6], and attributed to the minimization of the nanostructure free energy. This latter is mostly expressed through the reduction of the surface area by Plateau-Rayleigh instability.

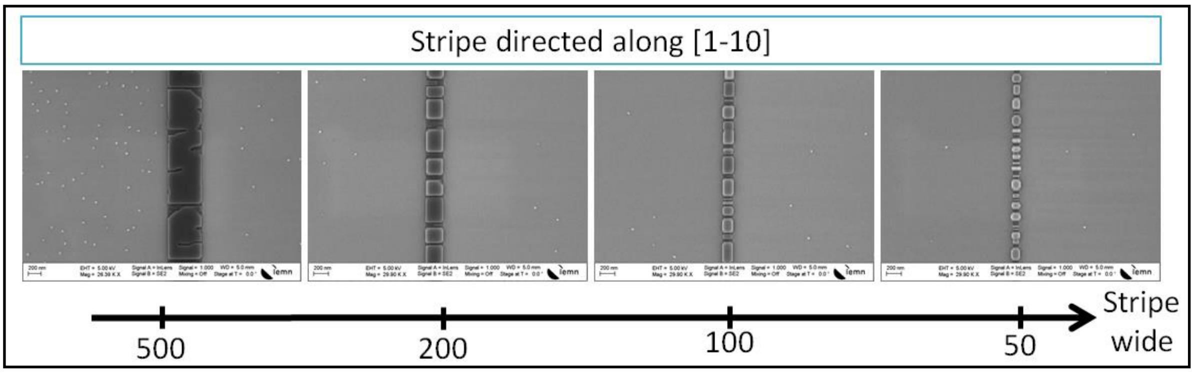

SEM images recorded after the growth of 25 nm of GaSb on GaAs for apertures directed along [1-10] when varying the stripes wide.

References

1. N. Moll, et al., ArXiv Prepr. Cond-Mat **9807200**, 1998.

2. G. Wulf, Z. Kristallogr. **34**, 449, 1901.

3. P. Müller and R. Kern, Surf. Sci. **457**, 1, 229-253, 2000.

4. E. Placidi, et al., *Self-Assembly of Nanostructures: The INFN Lectures III*, Nanoscale Science and Technology **12**, 2012.

5. B. Seiss and D. Dutartre, Solid-State Electron. **83**, 18–24, 2013.

6. T. Barwicz, et al., App. Phys. Lett. **100**, 093109, 2012.

Annex: Selective area growth of GaAs/GaAs(001)

The studied samples are made of 50 nm GaAs deposited on a patterned GaAs(001) sample at 550°C, a growth rate of 0.1 ML.s^{-1} and with a Sb/Ga flux ratio of 2. Before the growth, the GaAs native oxide layer for sample A and B was removed, respectively, by a thermal annealing under arsenic flux at 620-640°C and a thermal annealing under combined atomic hydrogen and arsenic fluxes at 450°C. Moreover, an atomic hydrogen flux was supplied during GaAs growth for sample B. The SEM images recorded for samples A and B are displayed in the figure below.

We notice that GaAs covers all the mask openings whatever their directions. Consequently, both GaAs deoxidization procedures lead to well deoxidized openings.

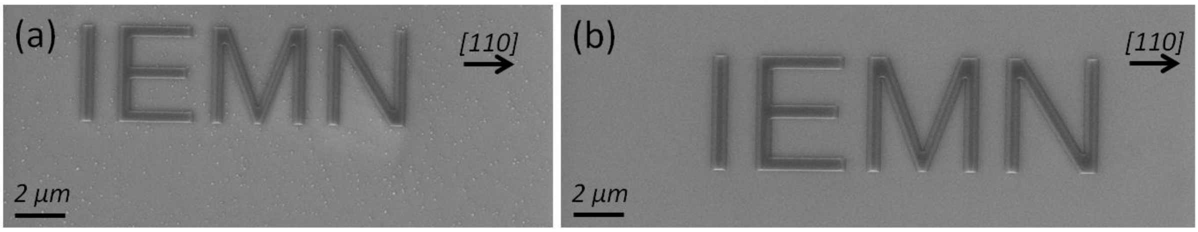

SEM images recorded after the SAG of 50 nm GaAs on patterned GaAs samples either thermally deoxidized under arsenic flux at 620-640°C (sample A(a)) or deoxidized under combined atomic hydrogen and arsenic fluxes at 450°C (sample B(b)).

LIST OF COMMUNICATIONS

Publications:

1) Selective area growth of in-plane InAs nanowires on GaAs (001) using Atomic Hydrogen-Assisted Molecular Beam Epitaxy
   M. Fahed, L. Desplanque, D. Troadec, G. Patriarche, X. Wallart
   Journal of Crystal Growth (Submitted,October 2016)
2) In-plane InAs nanowires on GaAs (001) using selective area heteroepitaxy of GaSb nanotemplates
   M. Fahed, L. Desplanque, D. Troadec, G. Patriarche, X. Wallart
   Nanotechnology ***27****, 50 (2016)*
3) Impact of P/In flux ratio and epilayer thickness on faceting for nanoscale selective area growth of InP by molecular beam epitaxy
   M. Fahed, L. Desplanque, C. Coinon, D. Troadec, X. Wallart
   Nanotechnology ***26****, 29, 295301 (2015)*
4) Influence of nanoscale faceting on the tunneling properties of near broken gap InAs/AlGaSb heterojunctions grown by selective area epitaxy
   L. Desplanque, M. Fahed, X. Han, V. K. Chinni, D. Troadec, M-P. Chauvat, P. Ruterana, X. Wallart
   Nanotechnology ***25****, 46, 465302 (2014)*

Communications:

1) Selective area growth of in-plane InAs nanowires on GaAs (001) using Atomic Hydrogen-Assisted Molecular Beam Epitaxy (Oral presentation)
   M. Fahed, L. Desplanque, D. Troadec, Y. Wang, P. Ruterana, G. Patriarche, and X. Wallart
   International Conference on Molecular Beam Epitaxy (MBE), Montpellier France, 4-9 Sep 2016

2) Selective area growth of GaSb in-plane nanowires on GaAs (001) by Atomic Hydrogen-Assisted Molecular Beam Epitaxy (Oral presentation)
   M. Fahed, L. Desplanque, D. Troadec, G. Patriarche, and X. Wallart
   Conférence Nationale sur les Processus Ultimes d'Epitaxie des Semiconducteurs (GDR Pulse), Marseille France, 18-22 juillet 2016
3) Selective area growth of GaSb nano-templates on GaAs (001) using atomic hydrogen assisted molecular beam epitaxy (Poster)
   L. Desplanque, M. Fahed, D. Troadec, P. Ruterana, and X. Wallart
   International Conference on Indium Phosphide and Related Materials (IPRM), Toyama Japan, 26-30 June 2016
4) Analyse par diffraction de rayons X de couches de GaSb épitaxiées par jets moléculaires sur substrats de GaAs nanostructurés (Poster)
   M. Fahed, L. Desplanque, D. Troadec, X. Wallart
   Journées Nano, Micro et Optoélectronique (JNMO), Les Issambres France, 30 mai-1 juin 2016
5) V/III flux ratio effect on faceting for nanoscale selective area growth of InAs and InP by molecular beam epitaxy (Poster)
   M. Fahed, L. Desplanque, C. Coinon, J. L. Codron, D. Troadec, X. Wallart
   Conférence Nationale sur les Processus Ultimes d'Epitaxie des Semiconducteurs (GDR Pulse), Porquerolles France, Sep 2015
6) Nanoscale selective area growth of InP by Molecular Beam Epitaxy : influence of the P/In flux ratio on the faceting (Oral presentation)
   M. Fahed, L. Desplanque, C. Coinon, J. L. Codron, D. Troadec, X. Wallart
   European Materials Research Society Spring Meeting (E-MRS), Lille France, 11-15 may 2015
7) InAs/AlGaSb Esaki tunnel diodes grown by selective area epitaxy on GaSb (001) substrate (Oral presentation)

L. Desplanque, X. Han, M. Fahed, V. K. Chinni, D. Troadec, M-P. Chauvat, P. Ruterana, X. Wallart

International Conference on Indium Phosphide and Related Materials (IPRM), Montpellier France, 11-15 may 2014

8) Croissance localisée d'InAs par épitaxie par jets moléculaires (Oral presentation)

M. Fahed, L. Desplanque, D. Troadec, X. Wallart

Journées Nationales du Réseau Doctoral en Micro-Nanoélectronique (JNRDM), Villeneuve d'Ascq France, 26-28 mai 2014